

Institut für Geodäsie und Geoinformation der Universität Bonn

**Wet Path Delay Corrections from Line-of-Sight Observations of  
Effelsberg's Water Vapour Radiometer for Geodetic VLBI Sessions**

Inaugural Dissertation zur  
Erlangung des Grades  
Doktor-Ingenieur (Dr.-Ing.)  
der  
Landwirtschaftlichen Fakultät  
der  
Rheinischen Friedrich-Wilhelms-Universität Bonn

vorgelegt am 31. Januar 2012 von

M.Sc. Jungho Cho  
aus Seoul

Referent: Priv.-Doz. Dr.-Ing. Axel Nothnagel  
Koreferenten: Prof. Dr.-Ing. Heiner Kuhlmann  
Assoc. Prof. Dipl.-Ing. Dr. techn. Johannes Böhm

Tag der mündlichen Prüfung: 28. Juni 2012

Publikation: Diese Dissertation ist auf dem  
Hochschulschriftenserver der ULB Bonn  
[http://hss.ulb.uni-bonn.de/diss\\_online](http://hss.ulb.uni-bonn.de/diss_online) elektronisch  
publiziert.

Erscheinungsjahr: 2012

## Zusammenfassung

Wasserdampfinduzierte Refraktionseffekte der elektromagnetischen Wellen stellen die zurzeit größte Fehlerquelle bei Messverfahren der Satellitengeodäsie, wie z.B. GPS und VLBI, dar. Die Problematik rührt hauptsächlich her von der stark variierenden Verteilung von atmosphärischem Wasserdampf sowohl in der Zeit als auch im Raum. Im Allgemeinen können diese Laufzeitverzögerungen durch den feuchten Anteil der Atmosphäre nicht exakt genug durch atmosphärische Modelle berechnet werden, die herkömmlich in Satellitengeodäsieanwendungen genutzt werden. In den vergangenen Jahrzehnten hat die Wasserdampfradiometrie ein großes Potential entwickelt, um den atmosphärischen Wasserdampfbestandteil zu messen. Allerdings ist der Prozess der Umrechnung von gemessenen Helligkeitstemperaturen in Laufzeitverzögerungen stark von gleichzeitig durchgeführten Radiosondenmessungen abhängig. Dabei werden die Messergebnisse von an aufsteigenden Ballons befestigten Wettersensoren für verschiedene Druckstufen per Radiosignal ausgesendet. Leider werden periodische Radiosondenbeobachtungen aber nur selten in der Nähe des Wasserdampfradiometers (WVR) durchgeführt. Dem gegenüber besteht seit einigen Jahren die Möglichkeit, ein numerisches Wettermodell anstelle der Radiosondenergebnisse zu nutzen. Ein numerisches Wettermodell kann meteorologische Profile für solche Orte liefern, wo eine Radiosonde nicht verfügbar ist.

Der Schwerpunkt dieser Dissertation liegt hauptsächlich auf der verbesserten Bestimmung der Laufzeitverzögerungen durch den feuchten Anteil der Atmosphäre in der geodätischen VLBI, wobei die Wasserdampfradiometerbeobachtungen am Radioteleskop in Effelsberg genutzt werden. Verglichen mit anderen Wasserdampfradiometern hat dieses Instrument große Vorteile hinsichtlich der Messwertgewinnung. Es zeigt immer in dieselbe Richtung wie die VLBI-Antenne, weil es im Primärfokus des Teleskopes installiert ist. In oder in der Nähe von Effelsberg werden jedoch keine Radiosondenbeobachtungen durchgeführt. Um diese Schwäche zu beheben, wurde ein numerisches Wettermodell des European Centre for Medium Range Weather Forecasts (ECMWF) für die Bestimmung von Kalibrierwerten herangezogen. Es liefert für das Radioteleskop in Effelsberg meteorologische Daten wie z.B. Druck, Temperatur und Wasserdampfdruck. Solche Profile wurden in einem Strahlungsübertragungsmodell verarbeitet, welches theoretische Messungen der Helligkeitstemperatur ermittelt und diese in Laufzeitverzögerungen durch den feuchten Anteil der Atmosphäre umwandelt.

Um die Laufzeitverzögerungen durch den feuchten Anteil der Atmosphäre aus Wasserdampfradiometermessungen und die Modelle besser vergleichen zu können, wurden alle Laufzeitverzögerungen durch den feuchten Anteil der Atmosphäre auf die Zenitrichtung (Zenith Wet Delays, ZWD) bezogen. Der Vergleich hatte zum Ergebnis, dass die ZWDs der Modelle einen um ca. 30 mm höheren Wert zeigten als jene, die mit einem Wasserdampfradiometer gemessen wurden. Im Vergleich zu GPS-abgeleiteten ZWDs betragen die durchschnittlichen Offsets der Modelle und des Wasserdampfradiometers  $-4.3 \pm 11.0$  mm beziehungsweise  $-44.8 \pm 24.0$  mm. Diese ZWD-Vergleiche haben gezeigt, dass eine Korrektur der WVR ZWDs erforderlich ist. Außerdem hatte es den Anschein, dass die rohen WVR-ZWD-Messungen geglättet werden sollten, um das Rauschen des Instruments zu reduzieren. Für die Fehlerkorrektur wurden außerdem in jeder einzelnen Session durchschnittliche Offsets

zwischen den Modellen und den Wasserdampfradiometern berechnet und angesetzt. Allerdings zeigte sich schon hier, dass die interne Kalibrierung des Instruments einige Defizite aufwies und die Ergebnisse dadurch in ihrer Genauigkeit eingeschränkt waren.

Die Korrekturen an den Laufzeitverzögerungen in Zenitrichtung aus verschiedenen Ansätzen wurden in fünf geodätischen VLBI-Sessionen verwendet und die Auswirkungen auf die Basislinienwiederholbarkeit und Höhengenaugigkeit untersucht. Es stellte sich heraus, dass die Basislinienwiederholbarkeit bei manchen Basislinien verbessert werden konnte, wenn Offsets an den gemessenen WVR-Ergebnissen angebracht wurden. Die Verbesserung war jedoch kleiner als 1 Prozent. Obwohl die Höhengenaugigkeit, ausgedrückt als Root Mean Squared Error (RMS) und Weighted RMS (WRMS), um den Faktor 2 verbessert werden konnte, zeigte die Höhenkomponente selbst eine größere Ablage von den Ursprungswerten als erwartet. Als Ursache dafür wurde die Vielzahl der zu schätzenden Parameter und ihre zum Teil hohen Korrelationen identifiziert.

Die Schlussfolgerung dieser Untersuchung ist somit, dass die Wasserdampfradiometerbeobachtungen in Effelsberg noch nicht gänzlich für die Fehlerbehebung der Laufzeitverzögerungen durch den feuchten Anteil der Atmosphäre geeignet sind, was hauptsächlich auf die Unvollkommenheit einer instrumentellen Kalibrierung zurückzuführen ist. Es werden weitere Studien mit einer größeren Zahl von WVR-Messwerten mit einer verbesserten Kalibrierung des WVR notwendig sein, um die Zweckmäßigkeit des Wasserdampfradiometers für die Fehlerbehebung der Laufzeitverzögerungen durch den feuchten Anteil der Atmosphäre in der geodätischen VLBI abschließend nachweisen zu können.

## Summary

Water vapour induced excess path lengths in electromagnetic waves have been one of the most unmanageable errors in space geodesy, such as GPS and VLBI. The difficulty mainly comes from the highly variable distribution of atmospheric water vapour both in time and space. In general, these wet path delays cannot be estimated accurately by atmospheric models that are conventionally used in space geodetic applications. In the last few decades, water vapour radiometry has shown great potential for measuring atmospheric water vapour content. However, the wet path delay retrieval processes are strongly dependent on radiosonde data, although periodic radiosonde observations are rarely available in the vicinity of water vapour radiometers (WVRs). Radiosonde observations are weather profiles from balloon starts which are transmitted by radio signals. On the other hand, the possibility of using a numerical weather model (NWM) instead of a radiosonde has been on the increase in recent years. NWM can provide meteorological profiles for those places where radiosonde data is not available.

The focus of this thesis is mainly on the improvement of the wet path delay corrections in geodetic VLBI sessions using the WVR observations at the 100m Effelsberg radio telescope. Compared to other WVRs, the Effelsberg one has a great advantage in terms of observation. It always points at the same direction as the VLBI antenna because it has been installed on the prime focus cabin of the telescope. However the Effelsberg station does not make periodic radiosonde observations. To overcome this weakness, the numerical weather model of the European Centre of

Medium Range Weather Forecasts (ECMWF) was introduced. It provides meteorological profiles over Effelsberg such as atmospheric pressures, temperatures, and water vapour pressures. Those profiles were processed by a radiative transfer model, which calculates theoretical measurements of brightness temperature and converts them into wet path delays. These two models were combined to be compared with WVR-observed wet path delays.

For a better comparison between wet path delays from the WVR and the models, zenith wet delays (ZWDs) were used. As the results of the comparison illustrate, ZWDs from the models showed higher values than the WVR-measured ones by roughly 30 mm. For comparison with GPS-derived values, average offsets and standard deviations of the models and the WVR were  $-4.3 \pm 11.0$  mm and  $-44.8 \pm 24.0$  mm, respectively. From these ZWD comparisons it was found that further corrections to the WVR ZWDs are necessary. In addition, the noisy behaviour of the raw WVR ZWD measurements should be smoothed by a running mean method before application. In addition, averaged offsets between the models and the WVR measurements should be determined for the correction of individual sessions. However, already at this step it became obvious that the instrumental calibrations of the radiometer are far from being mature resulting in erroneous absorption profiles.

ZWDs from the WVR measurements with different levels of corrections were applied as corrections to the wet components of the atmospheric refraction in the five geodetic VLBI sessions. Impacts on baseline repeatability and height precision by these were investigated. As the results show, the baseline repeatability was improved in terms of Root Mean Squared Error (RMS) when the offset correction was applied. However, the improvement was less than one percent. Although the repeatability of the height component was improved in terms of Weighted RMS (WRMS) with respect to the short term mean height by a factor of 2, the height component itself showed a larger deviation from the original value than that expected from the ZWD corrections. A possible reason is that the estimation of the many parameters in the least squares adjustment can easily affected the height parameter.

The conclusion of this study is that the Effelsberg WVR observations are not perfectly suited for wet path delay corrections yet. This is mainly due to the imperfectness of instrumental calibration. Further studies based on an increased number of WVR data with better internal calibrations seems to be necessary to make a final judgment regarding the usefulness of the WVR for wet path delay corrections in geodetic VLBI.

# Contents

<b>1. Introduction</b>	<b>7</b>
1.1 Motivation and objectives	7
1.1.1 Motivation	7
1.1.2 Objectives	8
1.2 Water vapour in Space Geodesy	9
1.2.1 Path delays induced by atmosphere	9
1.2.2 Path delay induced by water vapour	10
1.2.3 Path delay correction in geodetic VLBI	13
1.3 Water vapour sensors	15
<b>2. Water Vapour Radiometry</b>	<b>17</b>
2.1 Brightness temperature	19
2.2 Absorption Model	21
2.3 Retrieval coefficients	24
2.4 Various WVRs and their application for Geodesy	26
2.5 Effelsberg WVR instrument co-located with VLBI	29
<b>3. Numerical Weather Model and Radiative Transfer Model</b>	<b>34</b>
3.1 ECMWF	34
3.2 MonoRTM	36
3.2.1 Profile mode	40
3.2.2 Calculations	41
3.2.3 Error propagation	47
<b>4. Wet Path Delay Comparisons and Readjustments</b>	<b>49</b>
4.1 Wet path delays from the WVR at Effelsberg	50
4.2 Wet path delays from MonoRTM(ECMWF)	52
4.3 Comparison with GPS-ZWDs	54
4.4 readjustment of ZWDs	56
<b>5. ZWDs Applications to Geodetic VLBI and its Results</b>	<b>61</b>
5.1 Impacts on wet path delay corrections in geodetic VLBI	61
5.2 Impacts on baseline repeatability	69
5.3 Impacts on height precision	73
<b>6. Summary and Discussion</b>	<b>77</b>
<b>7. Conclusions</b>	<b>79</b>
Appendix	80
List of figures	96
List of tables	98
References	99

# 1. Introduction

## 1.1 Motivation and objectives

### 1.1.1 Motivation

Atmospheric water vapour degrades the accuracy of the results of space geodetic observations due to permanent electric dipole moments. It creates excess path lengths by retarding (slowing and bending) the propagation of the electromagnetic waves that are used in global positioning system (GPS) and very long baseline interferometry (VLBI) observations. It is known that the excess path lengths are less than 30~40 cm at the most, and are the primary obstacles of space geodesy because of the highly variable distribution of water vapour in the atmosphere.

According to Askne and Nordius (1987), this wet path delay cannot be determined by only using surface meteorological data with an accuracy of 1 cm or better in the zenith direction. To cope with this deficit, geodetic VLBI analysts normally estimate the wet path delay contributions via various approaches. However, the number of unknown parameters increases considerably and the results still leave room for improvement for many space geodetic applications. It is known that improved accuracy can be achieved by using remote sensing techniques. Several authors (Resch *et al.*, 1979, 1984; Ware *et al.*, 1986, 1993; Kuehn *et al.*, 1991, 1993; Johansson *et al.*, 1993; Teitelbaum *et al.*, 1996; Tahmoush and Rogers, 2000; Oswald *et al.*, 2005; Nothnagel *et al.*, 2007) suggested the use of water vapour radiometers (WVRs). A WVR measures the brightness temperature from the thermal emission of water molecules. In order to use a WVR for geodetic purposes, a conversion process from the brightness temperature to the wet path delay is necessary.

Since Elgered *et al.* (1991) presented the usefulness of WVRs to geodetic VLBI, the quality of WVRs has constantly improved. However, wet path delay retrieval from the water vapour content has always been dependent on radiosonde data. Radiosonde weather profiles originate from weather balloons which transmit their data via radio signals. Only a few WVR stations have access to radiosonde data acquired in the immediate vicinity. With the advent of numerical weather models (NWM), a new method for the conversion of the brightness temperature or the readjustment of the wet path delay corrections may be possible, even for stations where radiosonde data is not available.

Another modern development is that the observatory at Effelsberg has been operating a WVR with a new concept. Most WVRs measure brightness temperatures at only two distinct frequency channels. The Effelsberg WVR, however, possesses a receiver with 25 channels of 0.9 MHz bandwidth each, spanning from 18.3 to 26.0 GHz. Another promising feature of the WVR at Effelsberg is that it always points in the same direction as the VLBI antenna, continuously changing directions during geodetic VLBI sessions. In the absence of regular radiosonde observations in close vicinity to Effelsberg, it appears to be a suitable approach to use a NWM for improving the retrieval of the wet path delay corrections.

### 1.1.2 Objectives

The primary hypothesis of this thesis is that the new concept of the Effelsberg WVR together with data from NWM yields improved results for the geodetic parameters estimated from VLBI observations. In contrast to conventional two-channel WVR, the Effelsberg WVR scans the water vapour emission spectrum on multi-channels. This sampling allows the separation of the emission from instrument effects and from the emission of cloud water (Tahmoush and Rogers, 2000). In addition, the WVR can always keep the line-of-sight direction of the VLBI antenna. In order to use the WVR for geodetic purposes, the conversion process between parameters in different units is indispensable. WVR-measured brightness temperatures in Kelvin can be converted into wet path delays in millimetres via the so-called the retrieval process. Every retrieval algorithm includes conversion coefficients. The coefficients are derived from the relationship between WVR-measured brightness temperatures and radiosonde-derived wet path delays. Unfortunately, Effelsberg has no regular radiosonde observations. To cope with this deficit, a NWM will be introduced to provide meteorological profiles over Effelsberg. In order to calculate brightness temperature measurements based on the profiles, a radiative transfer (RT) model will be introduced. At the microwave frequencies used in this study, the radiation from water vapour molecules is an integrated quantity of the two opposite processes that are the emission and the absorption, as depicted in figure 1-1. A series of interactions of the two processes along a line-of-sight are called the cascade process. Chandrasekhar (1960) presented the radiative transfer equation of energy transfer in electromagnetic waves to describe such a cascade process. In combination with NWM, RT models provide a possibility for calculating theoretical measurements such as brightness temperatures and wet path delays using the profiles.

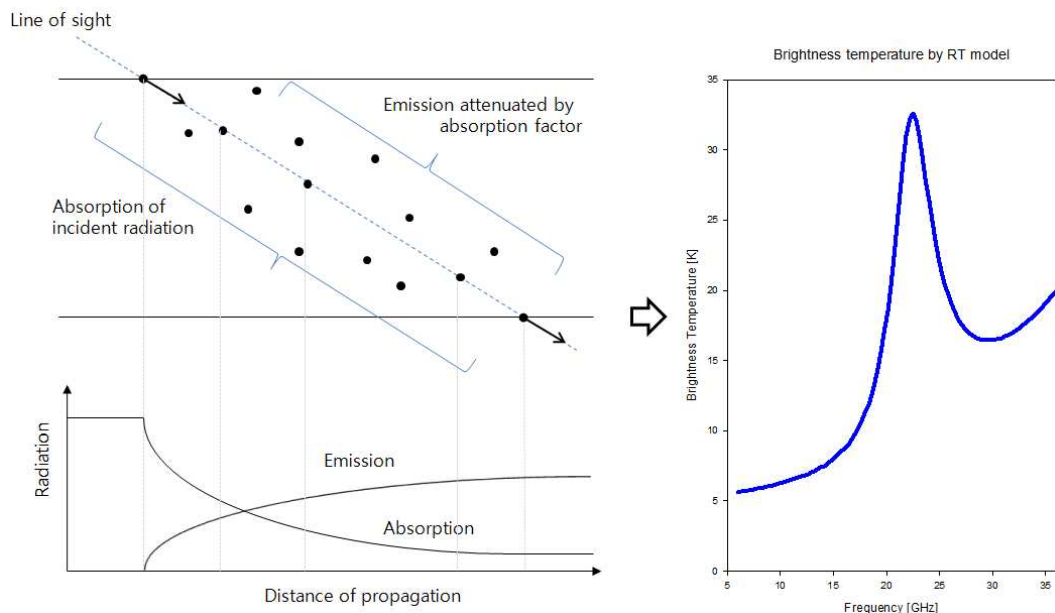


Figure 1-1. Conceptual diagram of the cascade process (left) to the brightness temperature (right) by RT model: The RT model calculates the brightness temperature using meteorological profiles provided by NWM



In order to find an improved method of retrieval, the investigations will be focused on the zenith wet delay (ZWD) by readjustment of the WVR measurements based on the model calculations. It may be possible to find the best readjustment through comparative investigations of geodetic parameters. This is similar to an adjustment process of the wet path delays, periodically fitting the WVR measurements to the radiosonde-derived wet path delays. In this study, radiosonde measurements will be replaced by the model calculations for the same purpose. As a final step, the readjusted ZWDs will be applied to geodetic VLBI sessions and their effects will be investigated mainly in terms of baseline repeatability and height precision. The key steps of this study are summarised below.

0. Calculate theoretical measurements using an RT model (MonoRTM; Clough *et al.*, 1989, 2005) introducing profiles from ECMWF
1. Readjust the measured ZWDs based on the theoretical calculations by the models.
2. Apply the readjusted wet path delays to the geodetic VLBI sessions
3. Investigate the effects of the delay corrections to the geodetic VLBI sessions mainly in terms of baseline repeatability and height precision.

When embarking on this thesis, it was expected that several geodetic VLBI sessions with useful WVR measurements at Effelsberg would be available eventually. However, in the course of time it turned out that only five sessions could be successfully observed. For this reason, the conclusions will have to be based on these five sessions alone.

## 1.2 Water vapour in Space Geodesy

Water vapour is one of the most pending obstacles for ground based space geodetic observations. In particular, space geodetic technologies using microwave frequencies such as GPS and VLBI mostly suffer from uncalibrated water vapour-induced delays. However, its distribution in the atmosphere is impossible to accurately predict only with atmospheric models. Thus, the wet path delay is still the limiting factor for further improvements in space geodesy.

As engineering technologies become more and more advanced, space geodesy is jumping to new levels of performance with unprecedented accuracy and precision particularly in positioning of global scale which is necessary for the maintenance of the Terrestrial Reference Frame (TRF). Until now, most of space geodetic networks are deployed on the surface of the Earth and use microwave signals for measuring distances and angles. The atmospheric water vapour contributes different excess path lengths to the distance measurements from individual sites in the global network, because each site is subject to different weather conditions. To meet the high performance of the observations themselves, the wet path delays have to be handled properly and corrected in more sophisticated manners.

### 1.2.1 Path delays induced by atmosphere

Ground-based space geodetic instruments observe microwave signals that are emitted from sources in outer space, such as Quasars and artificial satellites. The

microwave signal inevitably passes through the atmosphere to be detected at the surface of the Earth. Figure 1-2 depicts a typical condition of geodetic VLBI observations with two distant telescopes. The microwave signal reaching ground receivers includes the overall effects of error sources between the sources and the receivers. The signal experiences slowing and bending while it passes through the atmosphere. The atmosphere can be divided into two layers that are described in figure 1-2 in terms of delay causing factors.

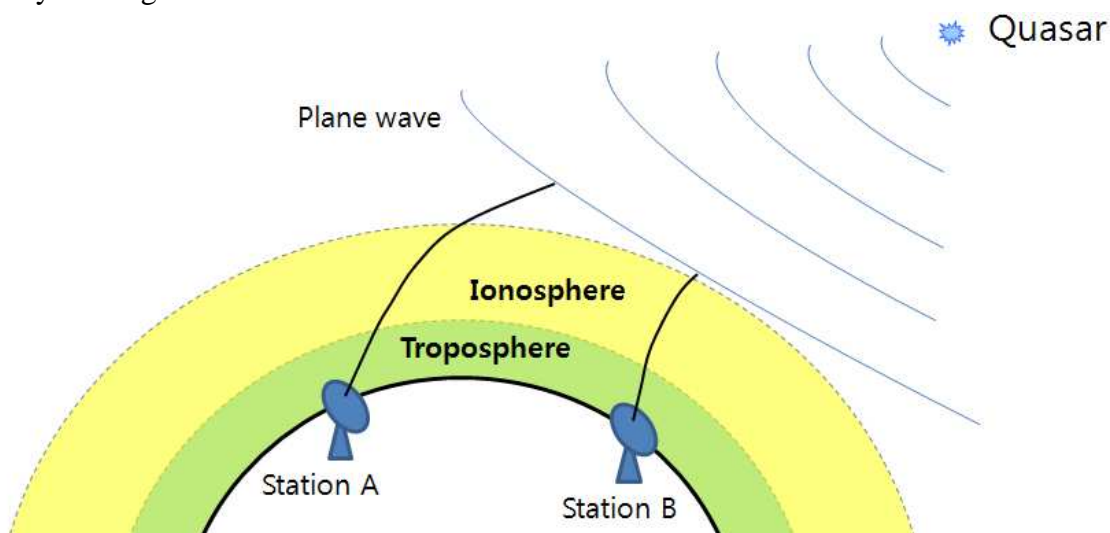


Figure 1-2. Microwave signal propagation at two separate geodetic VLBI stations

As can be seen in the figure, the microwave signal propagates through the ionosphere and troposphere. These layers affect the microwave signal with extra path delays in different ways. In the ionosphere, the signal is refracted mainly by dispersive constituents such as ionized molecules and free electrons. The level of the retardation by the dispersive medium depends on the frequency of the signal. It means that the ionospheric delays can be corrected by using differencing techniques between the two observed frequencies. This is the reason that VLBI and GPS use dual-frequency observation and ionosphere-free combinations to correct the ionospheric delays.

The troposphere is filled with neutral molecules such as nitrogen, oxygen, water vapour, etc. The second refraction takes place in the approximately ten-kilometre thick layer above the ground. Those neutral molecules have non-dispersive characteristics with respect to the microwave signal. It means that the tropospheric refraction depends on the amount of the non-dispersive constituents. Under the assumption of the homogeneous distribution of the neutral gases, the total loading by the constituents can be precisely estimated by measuring the atmospheric pressure at the ground. However, water vapour partial loading cannot be precisely estimated in the same way.

### 1.2.2 Path delay induced by water vapour

To extract the wet path delay from the tropospheric delay, it is convenient to start with a single antenna as depicted in figure 1-3. The wave propagates to the antenna along the curved path S instead of the straight path G due to gradients of refractive index. It also travels slower through the layers of certain density than it would in a vacuum. The tropospheric delay is the sum of these two effects.

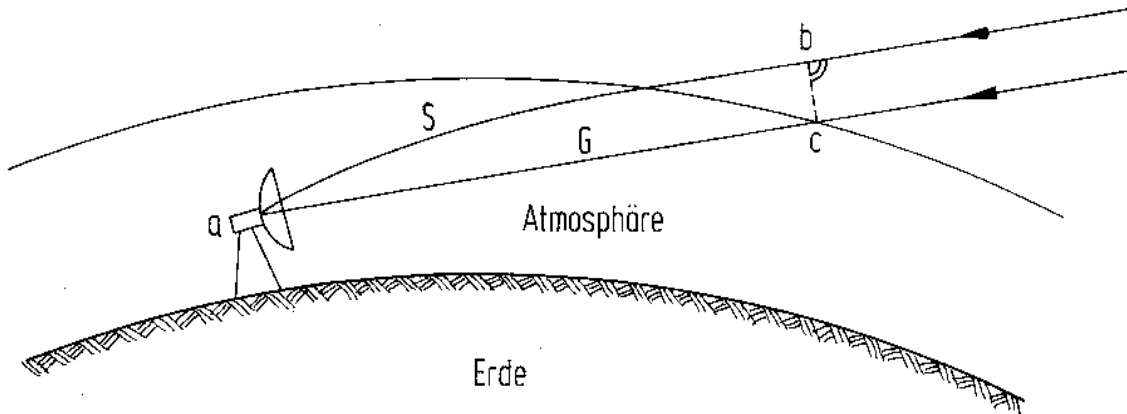


Figure 1-3. Signal propagation through the atmosphere (Elgered, 1993)

If the refractive index  $n$  is known, the electrical path length  $L$  of a signal propagating along  $S$  results in

$$L = \int_S n ds \quad (1.1)$$

As can be seen from the figure, the total excess path length by the troposphere  $\Delta L$  can be described as (Elgered, 1993)

$$\Delta L = \int_S n ds - G = \int_S (n - 1) ds + S - G \quad (1.2)$$

the first term on the right is due to the slowing effect and the remaining two terms ( $S-G$ ) are due to the bending effect that are known as 'the geometrical delay' or 'the delay due to bending'. The first term is more dominant than the second term, even at low elevation angles. The difference between remaining two terms vanishes in the zenith direction. Referring  $\Delta L$  to zenith and dividing it by the speed of light  $c$  results in the zenith total delay (ZTD) of the troposphere. This total tropospheric delay toward the zenith direction can be divided into two components; zenith hydrostatic delay (ZHD) and zenith wet delay (ZWD).

The previous equations can be reformulated with the atmospheric refractivity  $N$ , which is the key parameter to all theories concerning radio wave propagation.

$$N = 10^6 (n - 1) \quad (1.3)$$

Equation (1.2) can be written for the zenith direction

$$ZTD \cdot c = \Delta L^{zenith} = 10^{-6} \int_S N ds \quad (1.4)$$

Since Smith and Weintraub (1953) published the classic formula for  $N$ , the formula has been modified by several authors (Thayer, 1974; Hill *et al.*, 1982; Bevis *et al.*, 1994) taking into account non-ideal gaseous behaviour. The typical form of the formula is

$$N = k_1 \frac{P_d}{T} Z_d^{-1} + k_2 \frac{e}{T} Z_w^{-1} + k_3 \frac{e}{T^2} Z_w^{-1} \quad (1.5)$$

where  $P_d$  is the partial pressure of the dry constituents of air in mbar,  $e$  is the partial pressure of water vapour in mbar,  $T$  is the absolute temperature in K, and  $Z_d^{-1}$  and  $Z_w^{-1}$  are the inverse compressibility factors for dry air and water vapour, respectively. The inverse compressibility factors are corrections for the differences between non-ideal gas behaviours and ideal gas assumptions. Owens (1967) determined these two factors. The constants of  $k_1$ ,  $k_2$ , and  $k_3$  were determined from laboratory experiments. The latest values were given by Bevis *et al.* (1994) as  $k_1 = 77.6 \pm 0.05$  K/mbar,  $k_2 = 70.4 \pm 2.2$  K/mbar, and  $k_3 = 373900 \pm 1200$  K<sup>2</sup>/mbar, respectively.

The first term on the right of equation (1.5) is the dry refractivity ( $N_d$ ) and the other two terms are the wet refractivity ( $N_w$ ). Equation (1.5) can be written as

$$N = N_d + N_w \quad (1.6)$$

In order to express the total refractivity in terms of hydrostatic and wet terms, Davis *et al.* (1985) presented a modified equation of the refractivity using the gas law

$$P_i = \rho_i R_i T Z_i \quad (1.7)$$

where  $P_i$  is the partial pressure,  $\rho_i$  is the mass density,  $R_i$  is the specific gas constant,  $T$  is the absolute temperature, and  $Z$  is the inverse compressibility according to subscript  $i$  which is for dry and wet air. Then equation (1.5) can be modified

$$N = k_1 R_d \rho_d + k_2 R_w \rho_w + k_3 \frac{e}{T^2} Z_w^{-1} = k_1 R_d (\rho_d + \rho_w) + (k_2 - k_1 \frac{R_w}{R_d}) \frac{e}{T} Z_w^{-1} + k_3 \frac{e}{T^2} Z_w^{-1} \quad (1.8)$$

The first term on the right in equation (1.8) now contains contributions from dry air and water vapour, however, in hydrostatic equilibrium. For this reason, this term is called the hydrostatic component of the total refractivity. Equation (1.6) can then be written as

$$N = N_h + N_w \quad (1.9)$$

Finally, ZHD and ZWD can be expressed using equations (1.4), (1.8) and (1.9) for the zenith direction.

$$ZHD = \Delta L_h^{zenith} = 10^{-6} \int_S k_1 R_d (\rho_d + \rho_w) ds \quad (1.10)$$

$$ZWD = \Delta L_w^{zenith} = 10^{-6} \int_S [(k_2 - k_1 \frac{R_w}{R_d}) \frac{e}{T} Z_w^{-1} + k_3 \frac{e}{T^2} Z_w^{-1}] ds \quad (1.11)$$

$$ZTD = ZHD + ZWD \quad (1.12)$$

It is known that the ZTD is approximately 230 cm (~8 ns at sea level). The ZWD

just covers approximately 10% of the ZTD. The rest of the ZTD is covered by the ZHD which can be calculated from the measurements of surface meteorological parameters. Then, the ZWD can be estimated by differencing between the ZTD and the ZHD. Many VLBI stations operate a meteorological sensor at ground level to infer the ZHD precisely. According to Johansson *et al.* (1993), the ZWD shows geographical (latitude and height) and seasonal variations as well as biases between instruments.

If refractivity profiles from radiosonde observations are available, ZTD can be obtained from equation (1.4). Owing to the cost of radiosondes, empirical models for ZHD and ZWD are commonly used. These models use surface meteorological data and geodetic information of stations. According to Janes *et al.* (1991), the empirical models calculate ZHD with an accuracy of a few millimetres when using accurate surface pressure data. However, the empirical models for ZWD are not enough in terms of accuracy and precision.

### 1.2.3 Path delay correction in geodetic VLBI

#### *Empirical models*

Regarding the tropospheric delay corrections, several empirical models have been used. One of the most commonly-used models is the Saastamoinen (1972) model which describes the ZHD

$$ZHD = (0.0022779 \pm 0.0024) \frac{P_s}{f(\varphi, H)} \quad (1.13.a)$$

$$f(\varphi, H) = (1 - 0.00266 \cos 2\varphi - 0.00028H) \quad (1.13.b)$$

where  $P_s$  is the surface pressure,  $\varphi$  is the latitude in radians, and  $H$  is the height above the ellipsoid in kilometres. Several empirical wet delay models such as the Hopfield model (Hopfield, 1997) and the Ifadis model (Ifadis, 1986) have been developed.

$$ZWD_{Hopfield} = \frac{5}{10^6} (-12.96 T_s + 3.718 \cdot 10^5) 11000 \frac{P_v}{T_s^2} \quad (1.14)$$

$$ZWD_{Ifadis} = 0.554 \cdot 10^{-2} - 0.880 \cdot 10^{-4} (P_s - 1000) + 0.272 \cdot 10^{-4} + 2.771 \frac{P_s}{T_s} \quad (1.15)$$

where  $P_v$  is the partial water vapour pressure,  $P_s$  is the surface pressure, and  $T_s$  is the surface temperature.

In contrast to ZHD, ZWD is hard to determine precisely by a model because an accurate profile of water vapour partial pressure is not yet available. Instead, the wet path delays are estimated in geodetic VLBI with different parameterisations as described below.

#### *Mapping functions*

In general, a VLBI measurement is taken along a slant line-of-sight and the dry atmosphere is normally thicker than 50 km in altitude. Considering the fact that hydrostatic delays are corrected by a model, corrections for this atmospheric thickness require a complex elevation angle-dependent model (Takahashi *et al.*, 1997). To take into account the dependence on elevation angle of the VLBI observations, a mapping

function is needed for the conversion from zenith to any elevation angle. Considering the mapping function, the total excess path length  $\Delta L$  can be written as

$$\Delta L = \Delta L_h^{zenith} M_h(\varepsilon) + \Delta L_w^{zenith} M_w(\varepsilon) \quad (1.16)$$

where  $M_h(\varepsilon)$  is the hydrostatic mapping function,  $M_w(\varepsilon)$  is the wet mapping function, and  $\varepsilon$  is the elevation angle. Brief information regarding the mapping functions are reviewed in terms of the elevation angle dependency. The following synopsis is mainly based on Takahashi *et al.* (1997).

The dry component model was formulated based on a combination of Chao's mapping function (Chao, 1970) and Moran's zenith model (Moran, 1981) and was used extensively until the early 1980s. In terms of elevation dependency characteristics, improvements were made by the Marini model in the 1980s. There are two different types of model; the Marini and Murray model (1973) and the CFA model (Davis, 1985). While the Marini and Murray model has elevation dependency containing only a sin (elev.) term, the CFA model includes a tan (elev.) term, which is based on Chao's mapping function. Several other atmospheric delay models have also been proposed by Herring (1992) and Lanyi (1984). The Herring model adopts a different method of calculating the coefficients, and the Lanyi model uses a detailed formulation that uses separate formulations for daytime and nighttime data.

The elevation dependent mapping functions have increasingly been used in VLBI analysis since Niell (1996) proposed new mapping functions. This global model yields coefficients in the form of the continued fractions as a seasonal function, latitude, and height, without consideration of surface meteorological data. This model can be applied to elevation angles down to  $3^\circ$ , and is convenient for applying where meteorological data is not available.

Böhm *et al.* (2006) presented the Vienna Mapping Function 1 (VMF1) based on 40 years of reanalysis (ERA-40) data of the ECMWF. Some of the coefficients in the form of the continued fractions were re-determined. Unlike NWM-based mapping functions such as IMF (Niell, 2000), the new c coefficients are dependent on the day of the year, and unlike the new mapping function (Niell, 1996) they are no longer symmetric with respect to the equator.

There are several difficulties in developing an atmospheric delay model for wet components. The water vapour content of the atmosphere is quite unpredictable because water vapour distribution changes rapidly according to altitude, elevation angle, locality, and season. Moreover, every condition can vary within a few minutes to few hours, due to changes in the wind or ambient temperature. Considering these characteristics of water vapour, the use of WVR to directly measure atmospheric water vapour content can be an alternative to solving problems in determining the wet path delays without the influences explained above.

#### *Estimation of atmosphere parameters from VLBI observations*

Equation 1.16 contains 4 components for each VLBI observation. Whilst  $M_h(\varepsilon)$  and  $M_w(\varepsilon)$  are different for each observation,  $\Delta L_h^{zenith}$  and  $\Delta L_w^{zenith}$  are constant for certain time periods.  $\Delta L_h^{zenith}$  can be precisely determined from surface pressure, but  $\Delta L_w^{zenith}$  cannot be precisely determined using surface meteorological data. Thus,

$\Delta L_w^{zenith}$  remains the most uncertain parameter that is estimated with a varying time period in VLBI under the assumption of azimuthal symmetry of the atmosphere. However, in general, the atmosphere is not symmetric in azimuth angle. Thus, an atmospheric gradient in azimuth has been used. MacMillan (1995) modelled atmospheric gradient delay  $\tau$  as

$$\tau = M_h(\varepsilon) \cot(\varepsilon) [G_E \sin(\varnothing) + G_N \cos(\varnothing)] \quad (1.17)$$

where  $\varnothing$  is the azimuth angle of the radio source, and  $G_N$  and  $G_E$  are the north and east components of the gradient vector  $\mathbf{G}$ . This atmospheric gradient will be used for VLBI data processing in chapter 5.

### 1.3 Water vapour sensors

A variety of instruments to measure atmospheric water vapour have been developed. It is useful to view a water vapour sensor as a remote sensing instrument, because remote sensing techniques using electromagnetic waves provide a lot of information without direct contact with physical bodies (Sharkov, 2003).

A Water Vapour Radiometer (WVR) measures radiation energy from atmospheric water vapour molecules in microwave regions. The measurements are the brightness temperature assuming blackbody radiation of the water vapour molecules. The brightness temperature can be converted into the water vapour content by virtue of radiative transfer theory. Ground-based WVRs also measure the cosmic background microwave radiation. With knowledge of the temperature of the cosmic background radiation, a WVR can be precisely calibrated. Concerning the retrieval process, Bevis (1992) mentioned that the retrieval algorithm needs parameters which show variations in season and geographic location for allowing a WVR to exhibit its highest precision at a certain site. WVRs also have several disadvantages, such as an inconsistent structure, design, and instrument calibration by different manufacturers, and susceptibility to rain, fog, dew, and frost. Detailed fundamentals of water vapour radiometry is treated in the next chapter

Global Positioning System (GPS) is another reliable water vapour sensing tool. Since the mid 1990s, ground-based GPS meteorology has been widely used in various research areas, including geodesy. In recent years, satellite-based GPS meteorology is being used in climatology and ionosphere monitoring. (Jin *et al.*, 2007; Nilsson and Elgered, 2008; Sohn and Cho, 2010; Jee *et al.*, 2010) This can provide meteorological profiles, but it has quite a low time resolution because of an insufficient number of spaceborne GPS receivers. Ground-based GPS meteorology, which is based on microwave refraction by atmospheric water vapour, has big advantages in terms of data archiving for more than 15 years, reliable water vapour sensing tools, and continuous operation even under severe weather conditions. Recently, GPS-derived water vapour amounts were used as reference data during the verification of a radiosonde humidity sensor test (Takiguchi *et al.* 2000). They used precipitable water (PW) from GPS solutions as reference data to unreliable radiosonde-PW during a GAME-T project in the Asian monsoon season in 1998. Wang and Zhang (2008) found systematic errors in PW caused by different types of radiosonde humidity sensors in comparison with GPS-PW. They pointed out that GPS-PW data are useful for identifying and quantifying

several kinds of systematic errors in global radiosonde-PW data. It is widely accepted that GPS is presently one of the most reliable water vapour sensing tools. In this study, GPS-derived wet path delays will be used as reference data for comparisons with wet path delays from WVR observations and model calculations.

Chapter 2 describes the basic principles of water vapour radiometry and wet path delay retrieval. Chapter 3 describes the numerical weather and radiative transfer models and presents theoretical calculations. Wet path delays from Effelsberg's WVR observations and the model calculations are given in chapter 4. Effects on geodetic VLBI parameters after introducing the path delays will be shown in chapter 5. The thesis closes with a discussion and conclusions in chapter 6 and 7, respectively.



## 2. Water Vapour Radiometry

Water vapour radiometry is a measurement technique which uses electromagnetic radiation energy from atmospheric water vapour molecules in the microwave region. The water vapour radiometer used in this thesis is a ground-based and up-looking instrument. The most common electromagnetic radiation energy comes from the Sun. It reaches the ground after passing through the three atmospheric windows of the Earth, which are called the visible window, infrared window, and radio window. 51% of the energy passes through the visible window, 30% of the energy is reflected by the Earth's atmosphere, and the remainder is absorbed by atmospheric gases (Sharkov, 2003). In the infrared and radio windows, absorption takes place by minor gases such as water vapour, carbon dioxide, ozone, etc. Figure 2-1 shows the atmospheric transparency over Effelsberg in the microwave region of the radio window, if precipitable water is equivalent to a 15 mm water column. The atmospheric absorption spectrum for typical surface conditions is also shown. The highlighted frequency ranges of 18.3 to 26.0 GHz correspond to the 24 observation channels of the WVR at Effelsberg.

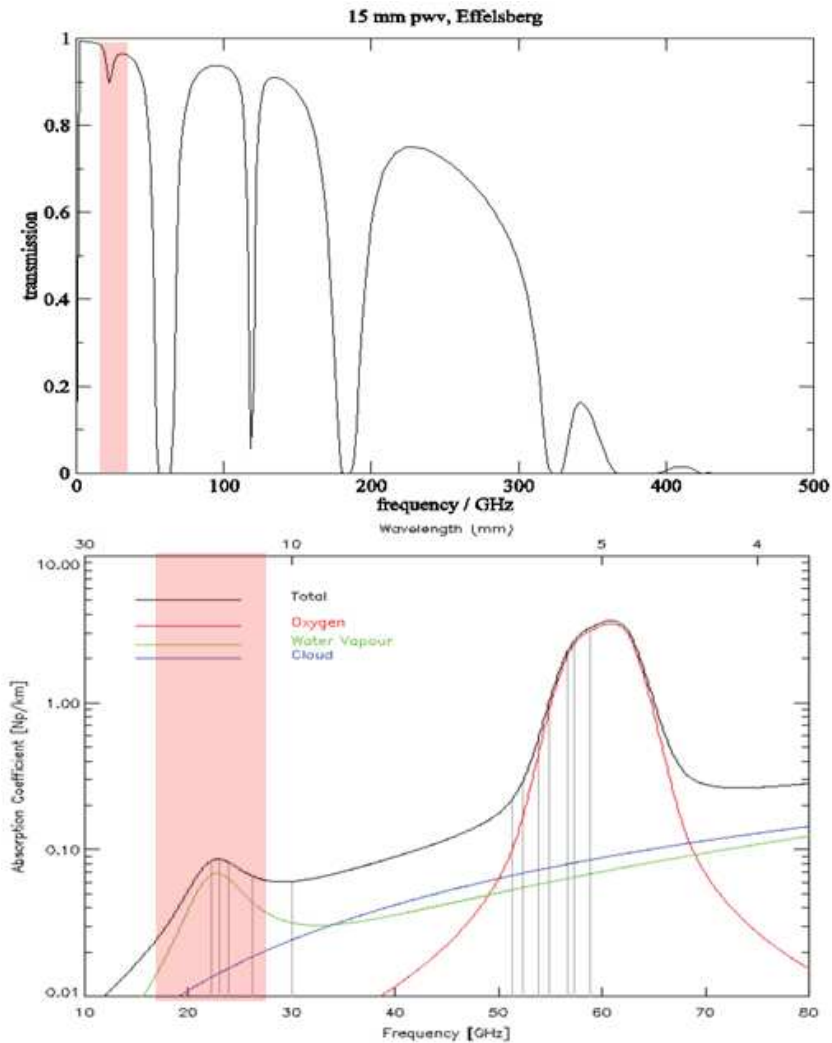


Figure 2-1. Atmospheric windows at Effelsberg, if PWV is 15 mm (Top; Roy *et al.*, 2004); Absorption spectrum for typical surface conditions:  $T = 288.15$  K,  $P = 1013.25$  hPa,  $RH = 100\%$  following Rosenkranz (Bottom; Hewison, 2007)

According to thermodynamic principles, the absorption is transformed into the thermal energy of the gases. Under the assumption of blackbody radiation, the reverse process of absorption, i.e. thermal emission, is balanced with the absorption in the atmosphere. These processes can be modeled by a radiative transfer equation. In principle, passive microwave radiometry needs a radiative transfer equation, which describes the radiant energy flow observed by the radiometer. The best-known radiative transfer equation is Chandrasekhar's (1960) equation, which introduces absorption, emission, and scattering processes. This equation has been widely used for astronomy and atmospheric sciences. In the microwave region, however, the effect of scattering on radiant energy transfer can be considered to be negligible because the microwave wavelength of not more than a few mm is still much larger than the liquid water size in drizzle or in clouds.

WVR is the instrument adopting the basic idea of radiative transfer and thermal (or blackbody) radiation theories. A WVR measures the radiation of water vapour molecules in the form of brightness temperatures, which only depends on the blackbody temperature. As mentioned in the previous chapter, the radiances consist of emissions and absorptions along the line-of-sight and are not directly proportional to the total amount of water vapour molecules because of the cascade processes as depicted in figure 1-1. Such passive and ground-based WVR instruments have been developed in different structures and ranges of frequency for various purposes, such as weather forecasting and climate, communications, geodesy and long-baseline interferometry, satellite data validation, air-sea interaction, and fundamental molecular physics (Westwater *et al.*, 2005). In recent decades, water vapour radiometry has shown great potential in quantifying atmospheric water vapour to determine excess path delays (Kuehn *et al.*, 1991, Linfield *et al.*, 1994, Tahmouh and Rogers, 2000, Niell *et al.*, 2001). WVRs can monitor water vapour content without any direct influence from the polar properties of water vapour molecules.

Figure 2-2 shows a block diagram of a common switched radiometer. In order to remove the instrument errors of WVRs, reference noise sources and tipping curve methods are normally used. If the temperature of the reference noise source and cosmic background radiation are given, one can obtain the temperature correction towards the zenith direction under clear sky conditions. One can also correct the elevation angle dependent effects when WVR measurements are provided for several different elevation angles.

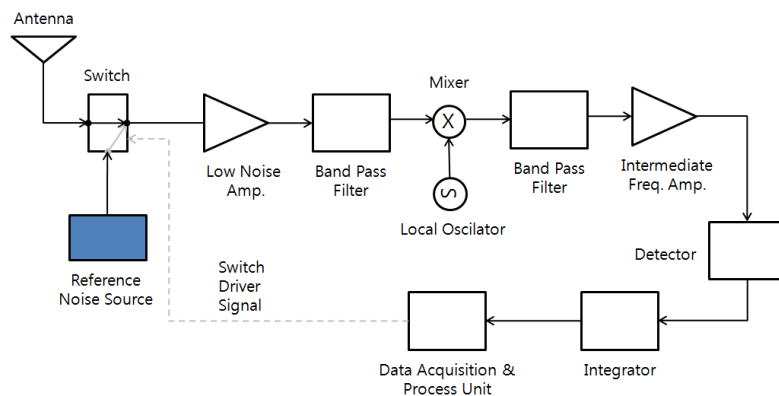


Figure 2-2. Block diagram of a switched radiometer

In the next section, the basic fundamentals of brightness temperature and comparisons of several absorption models will be summarised. Then, typical wet path delay retrieval algorithms of two-channel and multi-channel WVR instruments will be explained. Furthermore, detailed information about both WVR instruments will be introduced. Finally, various types of WVR instrument and their geodetic applications will be presented.

## 2.1 Brightness temperature

The brightness temperature is the temperature of a black body that is both an ideal absorber as well as an emitter. The term ‘black body’ is only true for the optical region, because a black body emits thermal radiation in the infrared region. The thermal radiation of a physical body, which has a physical temperature, arises from internal energy.

The internal energy enables spontaneous transitions between the rotation-vibration level of molecules in gases, oscillations of molecules in liquid and solid bodies and vibrations of a lattice in solid bodies with subsequent de-excitation of electromagnetic quanta. The radiation has a typical quantum character. The energy of radiation has a continuous spectrum and its own peak temperature. When thermal radiation is characterised by temperature at a given point, we can call it thermodynamic equilibrium or black-body radiation.

Brightness temperature is the primary observable of WVR. As a matter of fact, the radiances are an integrated quantity of two opposite processes, i.e. emissions and absorptions by water vapour molecules along the line-of-sight. It means that the radiance is not directly proportional to the total amount of water vapour molecules in the volume of the cylinder in the direction under consideration. A series of interactions between water vapour molecules during propagation through the atmosphere, which is called the cascade process, bring the integrated quantity of radiances to the WVR instrument. Figure 2-3 shows the cascade process that is a mixture of absorptions and emissions along the line of sight.

The basic equations of the brightness temperature are described below. Planck’s law describes the blackbody radiation.

$$B(f, T) = \frac{2f^2 k_B T}{c^2} \quad (2.1)$$

where  $f$  denotes the frequency,  $T$  the temperature,  $k_B$  the Boltzmann constant and  $c$  the light velocity. The brightness temperature  $T_B(f, s)$  can be expressed by the radiative flux density per frequency interval  $I(f, s)$

$$T_B(f, s) = \frac{c^2}{2k_B f^2} I(f, s) \quad (2.2)$$

The intensity  $I(f, s)$  is emitted by a blackbody radiator with the temperature  $T_B(f, s)$ .

For a non-scattering, non-refractive atmosphere in thermal equilibrium, the radiative

transfer equation takes a particularly simple form as given by Chandrasekhar (1960)

$$I(f, s_b) = I(f, s_a) e^{-\tau_f(s_a, s_b)} + \int_{s_a}^{s_b} k(f, s) B(f, T) e^{-\tau_f(s, s_b)} ds \quad (2.3)$$

where  $I(f, s_b)$  is the intensity of radiation at frequency  $f$  and position  $s_b$ ,  $k(f, s)$  the absorption coefficient at frequency  $f$  and position  $s$ , and the optical depth is quantified by

$$\tau_f(s_a, s_b) = \int_{s_a}^{s_b} k(f, s) ds \quad (2.4)$$

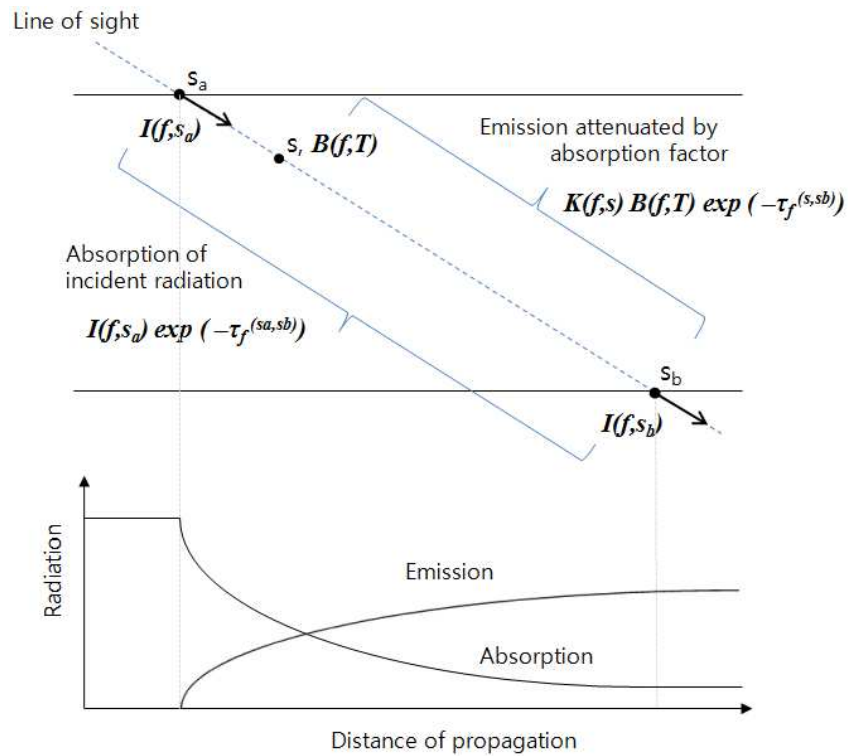


Figure 2-3. Geometry of the radiative transfer equation:

Figure 2-3 shows the geometry of the above equations. The first term on the right of equation (2.3) represents the absorption of the incident radiation while the microwave propagates through the atmosphere from  $s_a$  to  $s_b$  along the line-of-sight. The second term represents the emission along the propagation path. The emission term is also attenuated by the absorption factor  $e^{-\tau_f(s, s_b)}$ . Cruz *et al.* (1998) give the absorption coefficient of the 22 GHz water vapour with the Van Vleck-Weisskopf line shape.

Assuming a symmetric atmosphere with spherical layers, the brightness temperature can be described by the radiation transfer equation (2.3)

$$T_B(f, s) = T_{CB} e^{-\tau} + \int_0^{\infty} k(s) T(s) e^{-\tau(s)} ds \quad (2.5)$$

where  $T_{CB}$  is cosmic background radiation of 2.7 K.

## 2.2 Absorption model

As mentioned previously, ground-based microwave radiometry uses a simplified radiative transfer equation including absorption and emission processes. WVR observations can be used to retrieve information on the profiles of temperature, humidity and clouds in the troposphere. Although these retrievals can apply various techniques, most are sensitive to biases in the microwave radiometer's observations and the absorption model used in the radiative transfer calculations.

Since the time when absorption line shape models had been developed by Van Vleck-Weisskopf (1945) and Gross (1955) based on the rotational-vibrational resources of water vapour molecules, it has been known that the absorption of microwaves by water vapour is not entirely attributable to the nearby spectral line. Models for atmospheric water vapour transmittance, therefore, include an empirical component called the 'continuum' in addition to line contributions (Rosenkranz, 1998). This water vapour absorption model uncertainty is often the dominant error source for microwave remote sensing of the troposphere (Cruz *et al.*, 1998). However, the water vapour continuum contributes most of the opacity of a clear mid-latitude or tropical atmosphere at window frequencies of 30 GHz or higher.

Several absorption models have been developed and used for different purposes. Among them, only three models (MPM-series, Ros-series, and MonoRTM described below) are widely used these days. The following synopsis is based on Hewison (2006a, 2006b) except for MonoRTM:

- Millimeter-wave Propagation Model (MPM87) model (Liebe and Layton, 1987)  
The clear air absorption part of the MPM87 includes 30 water vapour lines and 44 oxygen lines all in the range of 20-1,000 GHz, based on theoretical values and a Van Vleck-Weisskopf shape function. These are supplemented by an empirically derived water vapour continuum, fitted to laboratory observations at 138 GHz. However, these observations were limited to 283—316 K, and must be extrapolated for typical atmospheric conditions.
- MPM89 (Liebe, 1989)  
The 1989 revision of MPM87 modified the parameters describing the 22 and 183 GHz water vapour lines, fitting the pressure broadened line width with four parameters, instead of one. Other components are the same as MPM87.
- MPM93 (Liebe *et al.*, 1993)  
This version of MPM, has 34 water vapour lines between 20 and 1000 GHz, defined in a slightly different manner from MPM89. The 183 GHz line is 8.5% wider and 5% stronger than in the MPM89. Like its predecessors, MPM93 includes 44 oxygen lines with the same line strengths but 5% greater widths and 15% stronger mixing than MPM89.
- Ros98 (Rosenkranz, 1998)  
Ros98 uses 15 water vapour line parameters, which are very similar to the strongest lines used in MPM89. The other half of the lines have been omitted as they were judged to have negligible impact. This model uses the same oxygen line parameters as MPM93, except at sub-millimetre frequencies, where values

from the HITRAN database (<http://www.cfa.harvard.edu/HITRAN/>) were used.

- Ros03  
In 2003, Rosenkranz updated his water vapour model to include recent measurements and a pressure line shift mechanism (Liljegren *et al.*, 2005). The intensity and air-broadened width of the 183 GHz line are 0.264% and 2% higher in Ros03 than Ros98. The other parameters of this line are unchanged.
- Lil05 (Liljegren *et al.*, 2005)  
Liljegren *et al.* (2005) used a model based on Ros03, but with a 5% smaller width of the 22 GHz line. They also suggested replacing the Ros03 continuum with MT\_CKD continuum (Mlawer *et al.*, 2004). These modifications were based on comparisons of zenith brightness temperature, modelled and observed with a radiometer. They showed that the modifications improved the fit with observed  $T_b$  trends, and also reduced the errors in profiles retrieved from them.
- MonoRTM ver. 4.2 (Clough *et al.*, 1989, 2005)  
MonoRTM is a monochromatic radiative transfer model for the microwave region, which is developed by Atmospheric and Environmental Research Inc. (AER) with support from the Atmospheric Radiation Measurement (ARM) program (Liljegren, 2001). The name is frequently used for the RT model as well as the absorption model because it is one of three widely used models in propagation and remote sensing communities adopting a Humlicek Voigt line shape (Humlicek, 1982) and MT\_CKD ver. 2.4 continuum. MonoRTM adopts a special spectroscopic line profile derived from the HITRAN\_2000 database. The MT\_CKD model includes continuum absorption due to water vapour, oxygen, nitrogen, carbon dioxide, and ozone. Regarding the water vapour continuum, it is the first model for both the self-broadening (between water vapour molecules) and the foreign broadening (between water vapour and the other molecules). Even if these two components are applied to the whole water vapour line, the effects are much more significant over the 30 GHz frequency range.  
MT\_CKD has an independent development history and continuous updates compared with MPM series models and Ros models. It covers the full spectral range from microwave to ultraviolet, and includes contributions from almost all atmospheric molecules that are unlikely to be present in other models. It also includes the latest spectroscopic advancements in radiative transfer algorithms, and has been extensively validated with high-resolution spectral measurements. MonoRTM is one of the most commonly used absorption models. A Web site has been established to host the AER radiative transfer models (<http://rtweb.aer.com>).

To compare the absorption models described above, it is helpful to summarise the features of each model. As mentioned, the water vapour continuum absorption parameterisation has two components, one accounting for broadening by foreign gases (e.g. nitrogen and oxygen) and the other accounting for broadening by water vapour (self). From the equations of the two continuum components, the foreign component increases linearly with the amount of water vapour. In contrast to the foreign component, the self component increases with the square of the amount of water vapour. To fit the line shape precisely, the Rosenkranz model used the modified parameters of MPM87,

and the MonoRTM model used the MT\_CKD continuum. Profiles of water vapour and temperature are needed as input to these microwave RT models. (Turner *et al.*, 2009) Table 2-1 lists the features of the absorption models in terms of line shape and the dependency of several parameters.

Table 2-1. Summary of commonly used absorption models

	Frequency dependence	Temperature dependence for self comp.	Temperature dependence for foreign comp.	Line shape	Gases
<b>MPM87</b>	Yes	Yes (most strong)	No	Van Vleck-Weisskopf	H <sub>2</sub> O, O <sub>2</sub> , & N <sub>2</sub>
<b>Ros98</b>	Yes	Yes	No	Modified MPM 15% increased coef. in foreign comp.	H <sub>2</sub> O, O <sub>2</sub> , & N <sub>2</sub>
<b>MonoRTM Ver. 4.2</b>	Very weak	Yes	No	Humlicek Voigt (in microwave) Lorentz (in infrared)	H <sub>2</sub> O, O <sub>2</sub> , N <sub>2</sub> , & others

Even though the models listed in table 2-2 are commonly used these days, a universally accepted definition of continuum absorption has not in fact been established. The issue of whether the absorption represents an excess or deficiency is fundamentally dependent on the line shape formulation chosen as the reference as well as on the frequency regime of interest. For example, the Van Vleck-Weisskopf line shape function has been used in Liebe and, with some modifications, Rosenkranz models to describe water and oxygen emission spectra. In both of them, an empirical continuum term has been added to account for excess attenuation between absorption spectra data and theoretical models. Cruz *et al.* (1998) identified several reasons for the excess absorption in the continuum. Although this excess has still to be understood, empirical modifications are needed to obtain more accurate agreement between measurements and theory.

In order to select an absorption model for this study, the literature has been studied for further up-to-date information. Several authors have attempted to use ground-based microwave radiometers and co-located radiosondes to check the validity of the absorption models. The following synopsis is also based on Hewison (2006a, 2006b) and edited results are only provided for frequency ranges around the water vapour peak line.

- Hewison *et al.* (2003) presented an independent validation of the performance of a microwave radiometer. Brightness temperatures observed in 12 channels from 22—59 GHz were compared with radiative transfer models, based on coincident radiosonde profiles under clear sky conditions. Overall, MPM89 provided the best fit in terms of average bias and RMS difference, although Ros98 showed improvements around the water vapour peak line.
- Cimini *et al.* (2004) conducted a similar analysis on data from 4 radiometers with a total of 19 channels between 20—59 GHz. They found that Ros98 gave the best results at 20.6—20.7 GHz channels, while MPM93 was preferable close to 22.2 GHz. These 2 models stayed within 0.3 K at 23.8 GHz, but Ros98 provided the best results in the atmospheric window (~30 GHz).
- Liljegren *et al.* (2005) analysed 5 channels between 22—30 GHz and showed that in using a 5% smaller width of the 22 GHz in Ros03 resulted in smaller biases in comparison with observed brightness temperatures, and also in

retrieved profiles. Their results also suggested that replacing the Ros03 continuum with MT\_CKD, which is used in MonoRTM, improved the fit with brightness temperature trends.

- Mattioli *et al.* (2005) compared brightness temperatures from 3 co-located Radiometrics Inc. instruments, each with channels at 23.8 and 31.4 GHz, using 2 calibration algorithms, with Vaisala RS90 radiosonde measurements forward modelled with various absorption models. Their results supported the modification of the water vapour continuum in Lil05, but not the change in width of the 22 GHz line.

As can be seen from the above summaries, the result from Hewison *et al.* (2003) and Cimini *et al.* (2004) are somewhat in contrast to each other, and a little modification of the models or new absorption models are needed for improvement. It becomes much clearer that no model can be perfectly applied to the whole spectrum. Liljegren *et al.* (2005) suggested using the MT\_CKD model instead of modification of Ros03 model. The MT\_CKD model is now used in MonoRTM, which has been selected in this study as the radiative transfer model. The reason will be explained in next chapter.

### 2.3 Retrieval coefficients

The Effelsberg WVR is a multi-channel instrument unlike the two-channel WVR instruments that are used in many other geodetic VLBI stations. Figure 2-4 depicts the observation channels of the two types of WVR instruments. Most of the two-channel WVR instruments follow the frequency pairs that were proposed by Wu *et al.* (1979). These pairs allow to separate the effects of liquid water, especially in the far-wing side, from that of the water vapour. In contrast, multi-channel or scanning type WVRs have many channels covering the peak emission line of water vapour and are able to separate water vapour emission from instrument effects and from the emission of cloud liquid water. Such differences require different retrieval methods.

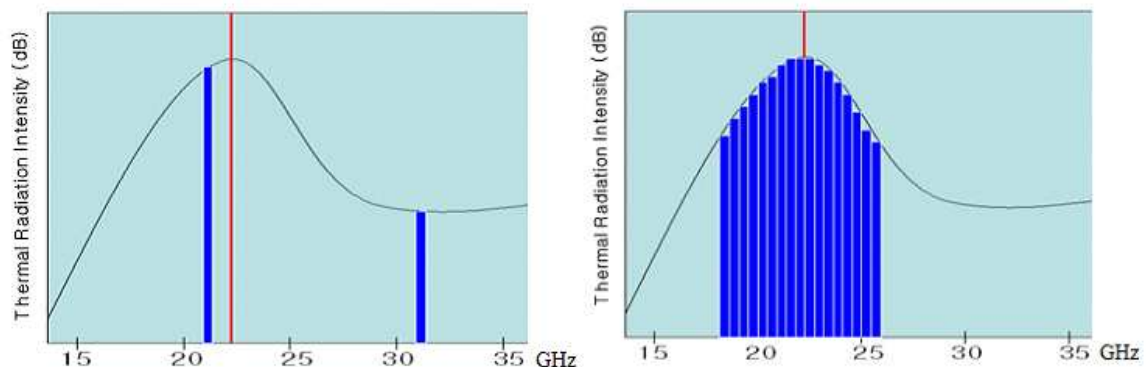


Figure 2-4. WVR observational frequency selections for typical two-channel and multi-channel instruments. The red lines mark the peak emission line of water vapour at 22.235 GHz.



In general, the retrieval process is an ill-posed problem. It means that the retrieval does not have a unique solution in time and space. Thus, there is no general retrieval for all WVR instruments. In general, the retrieval can be divided into two methods: statistical and physical (Loehnert and Crewell, 2003; Crewell and Loehnert, 2003). The statistical method requires representative data sets as true values. The data sets can be acquired from long-term radiosonde observations. In contrast, the physical method uses the radiative transfer equation to retrieve the parameters. This is sensitive to a priori profiles.

The retrieval is a conversion process from brightness temperatures in Kelvin to wet path delays in units of length. It means that the retrieval equation contains dimension-fitting coefficients between the two parameters. The coefficients normally come from comparisons between radiosonde-derived wet path delays and WVR-observed brightness temperatures on a long-term basis. Since the introduction of the general aspect of refractive correction in VLBI by Dickinson *et al.* (1970), a series of similar studies have been presented. Among them, several of the key papers are summarised below.

- Two channel retrieval method (Resch *et al.*, 1983)

$$\text{WPD} = C_{r1} + C_{r2} T_{b1} + C_{r3} T_{b2}$$

where WPD is the wet path delay,  $C_{r1}$ ,  $C_{r2}$ ,  $C_{r3}$  are Resch-Keihm type empirical coefficients, and  $T_{b1}$  and  $T_{b2}$  are the brightness temperatures of the two channels. Resch *et al.* (1982) described an experiment in which two WVRs are compared with a connected element interferometer on a 7 km baseline of the Very Large Array (VLA). In this experiment, each WVR is mounted on the 25 m telescope and uses the same optics as the interferometer which operated at 5 GHz.

- Two channel site-optimised retrieval method (Johansson *et al.*, 1993)

$$\text{WPD} = C_{j1} [ 1 + C_{j2} \text{COS}(t - C_{j3}) - C_{j4} (T_b - C_{j5}) ]$$

where  $C_{j1}$ ,  $C_{j2}$ ,  $C_{j3}$ ,  $C_{j4}$ ,  $C_{j5}$  are Johansson type coefficients,  $t$  is the day of the year, and  $T_b$  the linearized brightness temperature. Johansson *et al.* proposed seasonal variation and location dependent ZWD retrieval coefficients of the WVR measurements. They published optimised WVR ZWD retrieval coefficients for several globally distributed geodetic VLBI stations. This station-optimised coefficient method has an opposite philosophy to the global coefficients proposed by Resch (1983). Nevertheless, those two methods are normally used for dual-channel WVR instruments, which are commonly installed near geodetic VLBI antenna. The retrievals introduced up to here are the statistical methods.

- Multi-channel retrieval method (Tahmoush and Rogers, 2000)

$$\text{WPD} = C_{tr} T_{b\text{-peak}}$$

where  $C_{tr}$  is the Tahmoush and Rogers type coefficient, and  $T_{b\text{-peak}}$  the brightness temperature at peak. Tahmoush and Rogers used a scanning water vapour spectrometer and developed an improved method for determining the wet path length along the line of sight of the VLBI antenna. The scanning water vapour spectrometer instrument avoids the effects of gain drift and of emission of water droplets in clouds. They presented conversion factors from brightness temperatures to the wet

path delays using the absorption coefficients introduced by Cruz *et al.* (1998). This retrieval method is close to the physical method and was applied to the Effelsberg WVR observations scanning the spectrum from 18 to 26 GHz.

Most of the retrieval methods use a relationship between brightness temperatures measured by WVR and wet path delays measured by radiosonde observations. But each equation has a different number of coefficients because each method used different types of WVR instruments and observations from different radiosondes, as well as from different locations. The first two methods are for two-channel WVRs, whereas the last one is for multi-channel WVRs.

The first one is the most common method. A similar method was also developed by Keihm (1995). Resch *et al.* (1982) determined the three coefficients as an average value for global use. The second method was developed by Johansson *et al.* (1993), who determined coefficients for 18 sites that have their own radiosonde data. It can be considered a 'site-optimised' method. This method considered locality and seasonal variation resulting in a somewhat more complicated relationship between brightness temperature and WPD including five coefficients.

The third method is the multi-channel conversion method developed by Tahmoush and Rogers. With a scanning type of WVR instrument, a water vapour line profile model can be applied to separate the peak temperature from the liquid continuum. This method uses the van Vleck-Weisskopf water vapour line profile to determine the peak temperature directly at 22.235 GHz. A single scale factor can be used for the conversion. A multi-channel WVR instrument has been developed at Effelsberg adopting the idea of Tahmoush and Rogers. Detailed information will be given in chapter 4.






## 2.4 Various WVRs and their application for Geodesy


In terms of WVRs in geodetic applications, the first prototype instrument was developed by the Jet Propulsion Laboratory (JPL) in the late 1970s. This radiometer adopted doubly stabilised Dicke designs. The development was conducted as an R&D effort for the Crustal Dynamics Project and the Deep Space Network (Resch *et al.*, 1982). This two-channel WVR instrument had been a benchmark model for similar developments by other groups. Nowadays, numerous types of WVR instruments have been developed for various purposes. Since the time when Wu *et al.* (1979) presented their optimal frequencies pair selection for water vapour monitoring with WVRs, two channel WVRs have been widely used in atmospheric science and other applications (Rocken *et al.*, 1995, Linfield *et al.*, 1997). Some WVRs have more channels in the 20 to 30 GHz range and 50 to 60 GHz range to retrieve profiles of meteorological parameters such as humidity and temperature. A scanning type of multi-channel WVR has been introduced by Tahmoush and Rogers (2000). This type of WVR can effectively separate water vapour emission from instrument effects and cloud liquid. Roy *et al.* (2004) developed a similar type of WVR. It is operated at the Effelsberg radio telescope for scanning the spectrum from 18 to 26 GHz.

By virtue of the unparalleled principle of water vapour radiometry with other water vapour sensing techniques, WVRs have joined numerous water vapour sensing

experiments. Concerning wet path delay correction, several WVR instruments have been independently tested. Each of them has its own unique background in terms of development history and purpose. In table 2-2, several primary WVRs are summarised in terms of their frequencies and application, mainly with regard to the wet path delay correction.

Table 2-2. Summary of several WVR instruments

Instrument	Frequencies and applications
<p data-bbox="225 607 325 633">ASTRID</p>  <p data-bbox="225 853 341 880">KONRAD</p> 	<p data-bbox="518 663 1206 689">Onsala Space Observatory, Chalmers University of Technology</p> <p data-bbox="560 692 1011 719">Frequencies: 21.0 &amp; 31.4 GHz (ASTRID)</p> <p data-bbox="708 721 1059 748">20.64 &amp; 31.63 GHz (KONRAD)</p> <p data-bbox="560 750 676 777">Applied to</p> <p data-bbox="601 779 1174 842">Optimised wet path delay algorithm using WVR data (Johansson <i>et al.</i>, 1987)</p> <p data-bbox="601 844 1281 871">Inter-WVR comparison for wet path delay (Kuehn <i>et al.</i>, 1993)</p> <p data-bbox="601 873 1369 936">ZWDs comparison between NWM-derived and VLBI, GPS, and WVR (Behrend <i>et al.</i>, 2002)</p> <p data-bbox="601 938 1321 965">CONT02 (Snajdrova <i>et al.</i>, 2006) and CONT08 (Haas <i>et al.</i>, 2008)</p>
<p data-bbox="225 1093 309 1120">WAVE</p> 	<p data-bbox="518 1149 1294 1176">Effelsberg Radio Telescope, Max-Planck Institute for Radio Astronomy</p> <p data-bbox="544 1178 999 1205">Frequencies: 18.3~26.0 GHz, 25 channels</p> <p data-bbox="544 1207 660 1234">Applied to</p> <p data-bbox="585 1236 1273 1299">WVR calibration applied to European VLBI observing sessions (Nothnagel <i>et al.</i>, 2007)</p> <p data-bbox="585 1301 1195 1328">Inter-comparison WVR-GPS (Rottmann and Roy, 2007)</p>
<p data-bbox="225 1391 328 1417">AWVR 1</p> 	<p data-bbox="518 1442 951 1469">Deep Space Station, Jet Propulsion Lab.</p> <p data-bbox="560 1471 978 1498">Frequencies: 22.2, 23.8, and 31.4 GHz</p> <p data-bbox="560 1500 676 1527">Applied to</p> <p data-bbox="601 1529 1153 1592">Wet path delay correction for Deep Space Network (Oswald <i>et al.</i>, 2005)</p>
<p data-bbox="225 1731 352 1758">WVR-1100</p> 	<p data-bbox="518 1722 798 1749">Radiometrics corporation</p> <p data-bbox="560 1751 893 1778">Frequencies: 23.8 &amp; 31.4 GHz</p> <p data-bbox="560 1780 676 1807">Applied to</p> <p data-bbox="601 1809 1209 1872">Westford water vapour experiments (Coster <i>et al.</i>, 1996; Niell <i>et al.</i>, 2001)</p> <p data-bbox="611 1874 1233 1901">Inter-comparison campaign in Italy (Pacione <i>et al.</i>, 2002)</p> <p data-bbox="611 1904 1078 1930">MATRAG campaign (Haefele <i>et al.</i>, 2005)</p> <p data-bbox="611 1933 1150 1960">Wetzell inter-comparison (Schlueter <i>et al.</i>, 2006)</p> <p data-bbox="611 1962 1294 1989">Kashima VLBI station during CONT05 (Ichikawa <i>et al.</i>, 2006)</p>

<p>WVR2000</p> 	<p>ETH Zurich  Frequencies: 23.8 &amp; 31.5 GHz  Applied to  Wetzell inter-comparison (Schlueter <i>et al.</i>, 2006)  Hartebeesthoek station during CONT05(Combrinck and Nickola, 2005)</p>
--	--

In addition, many more WVRs have been developed and used for various experiments. Nevertheless, the WVRs listed above have produced results that are closely related to this study. Hereafter, several key papers together with their experimental results are summarised.

Concerning pointed WVR observations to tropospheric calibrations in geodetic VLBI, Resch and Claflin (1979) proposed WVR as a calibration tool for the wet path delay for the first time. In addition, they mentioned a plan for the co-location of WVR near VLBI. Ware *et al.* (1993) tested pointed WVR corrections for precise GPS positioning. They showed improved vertical precision compared with the zenith WVR when the pointed WVR was introduced. Haeefele *et al.* (2005) presented an improvement of GPS height precision and wet path delay estimation using WVRs. As an extension of these studies, Nothnagel *et al.* (2007) proposed a WVR-based calibration method to geodetic VLBI and pointed out improvements to baseline repeatability.

Concerning performance tests, numerous WVR instruments were tested in various experiments. The participating instruments differ in terms of design and specifications in each experiment. Moreover, other water vapour sensing tools such as radiosondes, GPS, and VLBI appeared in many cases. Since Kuehn *et al.* (1993) tested the performance of a WVR in terms of the accuracy of the wet path delays, several similar experiments have followed. In 1994, Linfield *et al.* tested WVR-based troposphere calibration for short baseline observations of VLBI. They showed that 80-90% of tropospheric fluctuations can be removed using WVR for VLBI. Westford Water Vapour Experiments (WWAVE) were conducted in August 1995 near the Haystack Observatory. This first multi-sensor inter-comparison campaign included radiosonde, GPS, VLBI, and WVR. Coster *et al.* (1996) reported offsets and standard deviations of WVR-ZWDs with respect to other instruments. Those ZWDs showed offsets of up to tens of millimetres. Niell *et al.* (2000) presented more detailed results for WWAVE. Pacione *et al.* (2002) carried out a similar inter-comparison campaign like WWAVE in Italy. They showed approximately 1 mm agreement in integrated precipitable water between GPS and WVR. Bar-Sever *et al.* (2004) proposed a multi-sensor approach for wet path delay corrections. They used co-located GPS, pointed WVR and barometer aiming at the exploitation of the strong point of each instrument. Zhang *et al.* (2008) suggested GPS-based tropospheric correction for VLBI. They found that ZWDs from GPS and VLBI agreed to within a few millimetres. Based on this agreement, a new way of tropospheric correction using GPS was suggested. Although certain systematic biases between water vapour sensing instruments used in the previous studies exist, it is hard to determine a fixed value from a one-off experiment. For the wet path delay correction, periodic comparison experiments are always needed.

IVS has a two-week special campaign of a continuous monitoring session, which is called CONT. The three network stations of CONT, which are Kokee Park, Onsala, and Wettzell, have been operating WVR instruments. Up until now, CONT campaigns had been conducted in 2002, 2005, and 2008. There are several comparisons regarding WVR. Snajdrova *et al.* (2006) presented comparisons between ZTD from VLBI, GPS, DORIS, WVR, and ECMWF. Among the comparisons, the difference between WVR and ECMWF revealed the biggest offset. But ECMWF agreed well with the other three space geodetic techniques. Ichikawa *et al.* (2006) conducted ZWD comparisons between co-located instruments; VLBI, GPS, and WVR. The agreement of averaged ZWDs between WVR and GPS was within 13 mm, while between WVR and VLBI it was more than 20 mm. They pointed at the WVR retrieval coefficient error as one of the reasons for the disparity. Haas *et al.* (2008) presented preliminary comparison results between ZWDs from VLBI, GPS, and WVR. Average offset between ZWDs from VLBI and WVR (ASTRID) was 1 mm.

In addition, numerical weather models can provide meteorological data for WVR calibration instead of radiosonde. NWM have been used for the development of mapping functions (Niell, 2001, Böhm *et al.*, 2004, 2006) and the improvement of wet path delay estimation (Hobiger *et al.*, 2008). In recent years, studies of ZWDs from NWM have been conducted. Behrend *et al.* (2002) presented comparisons between ZWDs from VLBI, GPS, WVR, radiosonde, and MM5 (PSU/NCAR mesoscale model) NWM. The difference between WVR and MM5 was  $-5.2 \pm 25.5$  mm. Niell and Leidner (2006) proposed a NWM-aided method for retrieving wet path delays. They presented ZWD corrections based on NWM, introducing a ratio between brightness temperature and wet path delay.

As summarised above, various types of WVR have been used for various geodetic applications. Most of which were two-channel WVR instruments. However, only a few studies handled a multi-channel WVR for geodetic purposes, so they should be investigated further. In addition, NWMs have emerged as an alternative to radiosondes near WVRs. Therefore, this study focuses on wet path delay corrections using a multi-channel WVR and NWM for geodetic VLBI. In the next section, details of the multi-channel WVR at Effelsberg and of the NWM used in this study will be introduced in the next chapter.

## 2.5 Effelsberg WVR instrument co-located with VLBI

Effelsberg has participated in European VLBI campaigns since 1991, and has operated a multi-channel WVR since 2004. This section focuses on the introduction of Effelsberg as a WVR station co-located with VLBI.

### *European geodetic VLBI network*

First of all, it is helpful to understand the Effelsberg radio telescope in terms of the European geodetic VLBI network. The European geodetic VLBI network comprises several stations as shown in figure 2-5. The network has participated in IVS Europe sessions since 1990 for the determination of the station coordinates and their evolution. The wet path delay of each station can be estimated by using atmospheric models and

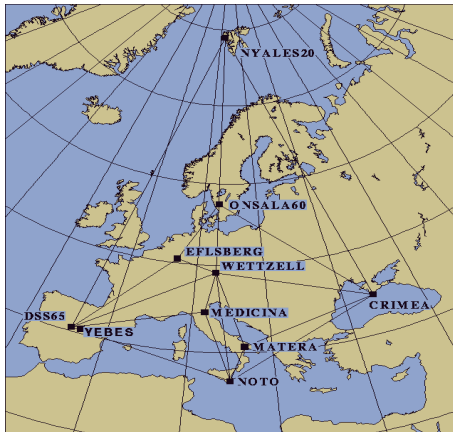


Figure 2-5. European geodetic VLBI network ([http://vlbi.geod.unibonn.de/europe/euro\\_net.gif](http://vlbi.geod.unibonn.de/europe/euro_net.gif))

meteorological data from the station log files. Each station’s log file contains in-situ meteorological measurements such as temperature, pressure, and humidity at ground level. Some of the European VLBI stations have operated various instruments such as AWS (Automatic Weather System), WVR, and GPS to calibrate the wet path delay.

Considering the WVR data availability at Effelsberg, five sessions within the IVS Europe campaign have been used in this study as summarised in table 2-3. As can be seen in the table, only three stations (Effelsberg, Onsala, and Wettzell) participated in all the five sessions.

Table 2-3. Summary of the five sessions

Sessions	Observation time (UT)	Participating Stations
Euro78	17:30 Dec. 13 – 17:30 Dec. 14, 2005	6aEbMcMhNyOnSvWz
Euro81	12:00 May 29 – 12:00 May 30, 2006	6aEbMcMhNtNyOnSmWzZc
Euro88	17:30 July 3 – 17:30 July 4, 2007	EbMcMhNtNyOnSmWz
Euro94	17:30 July 8 – 17:30 July 9, 2008	EbMhNtOnSmWz
Euro99	12:00 May 25 – 12:00 May 26, 2009	6aBdEbMcMhOnSmWzYs

*The line-of-sight WVR at Effelsberg and a typical ground-based WVR at Onsala*

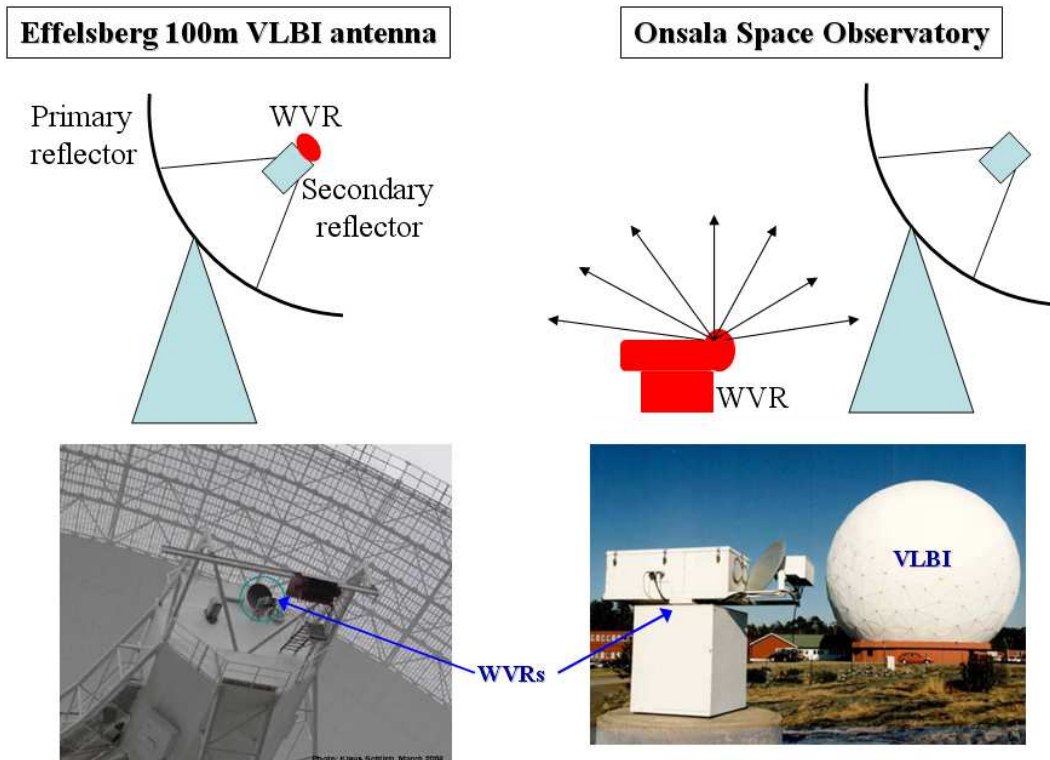


Figure 2-6. WVR instruments on the Effelsberg 100m radio telescope (left) and Onsala Space Observatory (right)

As shown in figure 2-6, the WVR at the Onsala Space Observatory as many other WVRs in the world is a typical two-channel instrument. It is installed on the ground and runs its own schedule for obtaining wet path delays in the zenith direction. In contrast, the Effelsberg WVR instrument is installed on the top of the subreflector of the 100 m radio telescope always pointing in the same direction as the primary reflector. This is currently considered the best method of WVR observations for obtaining the wet path delays for correcting VLBI observations.

The second benefit is the number of channels which covers the frequency range of 18.0 to 26.5 GHz used for separating the water vapour emission from liquid water. The Effelsberg WVR has been developed as a multi-channel instrument following Tahmoush and Rogers' prototype. The specifications of the WVR are summarised in table 2-4.

Table 2-4. Specifications of Effelsberg's WVR

Frequency	18.3 ~ 26.0 GHz
Channels	24 (originally 25 up to 10.02.2005)
Bandwidth	900 MHz
Beamwidth	1.3 degrees
Scan rate	3 seconds
Calibration	Uses noise diode continuously and occasional tipping scans

As depicted in figure 2-2, WVRs use reference noise sources for absolute calibration. Here, an external noise diode is used as a hot load, and external liquid nitrogen has been used once or twice as a cold load. In order to avoid the disadvantages of applying liquid nitrogen in terms of massiveness and accompanying riskiness in use on the focus cabin, the cold sky was used as the cold load, instead. This cold sky method should be able to obtain the sky contribution, and works well under cold and clear sky conditions. However, this method has a defect in that it is easily affected by unexpected radiations during sky temperature measurements. In general, the absolute calibration determines the reliability of WVR measurements because each spectrum acquired is calibrated by absolute calibration parameters. The cold sky method used in Effelsberg will be discussed in next chapters, particularly for handling with WVR measurements. Although the brightness temperature of the water vapour line in the spectrum is related to the wet path delay, the WVR results also depend on the age of the parameters determined by the absolute calibration. Along with the shortcomings of cold sky, the age of the absolute calibration will be discussed in next chapters.

Since the construction of the WVR at Effelsberg which was completed in 2002, several preliminary tests for instrument performances have been conducted. Rottmann and Roy (2007) summarised the results of several tests. The following experimental results are based on their report.

The WVR at Effelsberg has been used for wet path delay comparisons with other instruments such as radiosonde, GPS, and other types of WVR. The first co-location campaign with three different WVR instruments was conducted in the middle of July 2005. The second campaign with radiosonde and GPS was conducted at the end of July 2005. Figure 2-7 shows the comparison results of ZWDs from Effelsberg's WVR (MPI), Radiometrics Inc., and ETH Zurich (ETH). As shown in table 2-2, the instruments from Radiometrics and ETH are dual-frequency WVRs.

As can be seen in the figure, the relative behaviour of the zenith wet delays from the

MPI WVR and Radiometrics WVR agree well. However, there is an obvious offset of approximately 40 mm. ETH shows partially inconsistent behaviour with respect to MPI. But there is no such large offset between ETH and MPI. Possible reasons for the 40 mm offset may be incorrect calibration parameters. For the MPI WVR, zenith wet delays show unreliable behaviour at low elevation angles of under 20 degrees, as shown in the hatched boxes. It seems to be an obvious defect of the MPI WVR.

At the end of July 2005, three radiosondes were launched near the 100 m telescope at Effelsberg. To compare the wet path delays from radiosonde and GPS, five GPS stations around Effelsberg with distances ranging from 17 km to 110 km were selected. For direct comparison between the different tools, GPS ZWDs were converted into the values of the reference point height of the Effelsberg telescope. Figure 2-8 shows the comparison results of ZWDs from the three different methods. As can be seen in the figure, a weather front was passing over Effelsberg increasing the ZWD by 40 mm in 5 hours. The ZWDs from the three methods are in agreement with each other within a few tens of millimetres. Although ZWDs from the closest GPS station Euskirchen show the most similar tendency to ZWDs from MPI WVR, a different tendency is also discernable in the first two hours. ZWDs from the first two radiosonde measurements agreed with the radiometer within a few millimetres but the last radiosonde measurement shows roughly 20 mm difference with respect to the radiometer

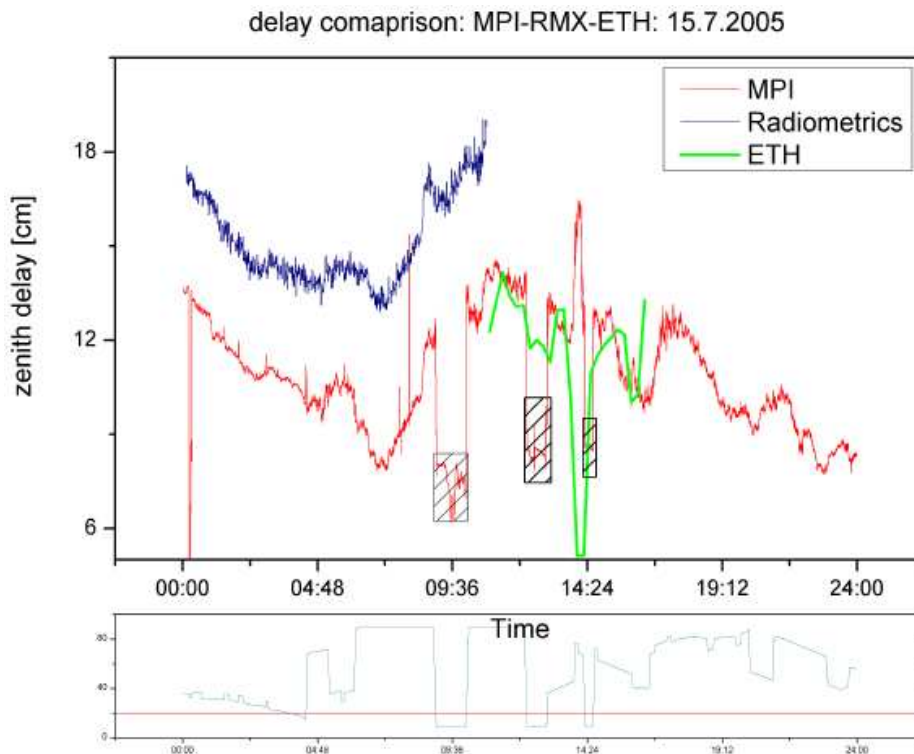


Figure 2-7. Comparison of zenith wet delays (ZWD) simultaneously measured by the three WVR. The blue line corresponds to the Radiometrics WVR, the red line to the MPI WVR, and the green line to the ETH WVR. Hatched boxes correspond to low elevation angles under 20 degrees (Rottmann and Roy, 2007)



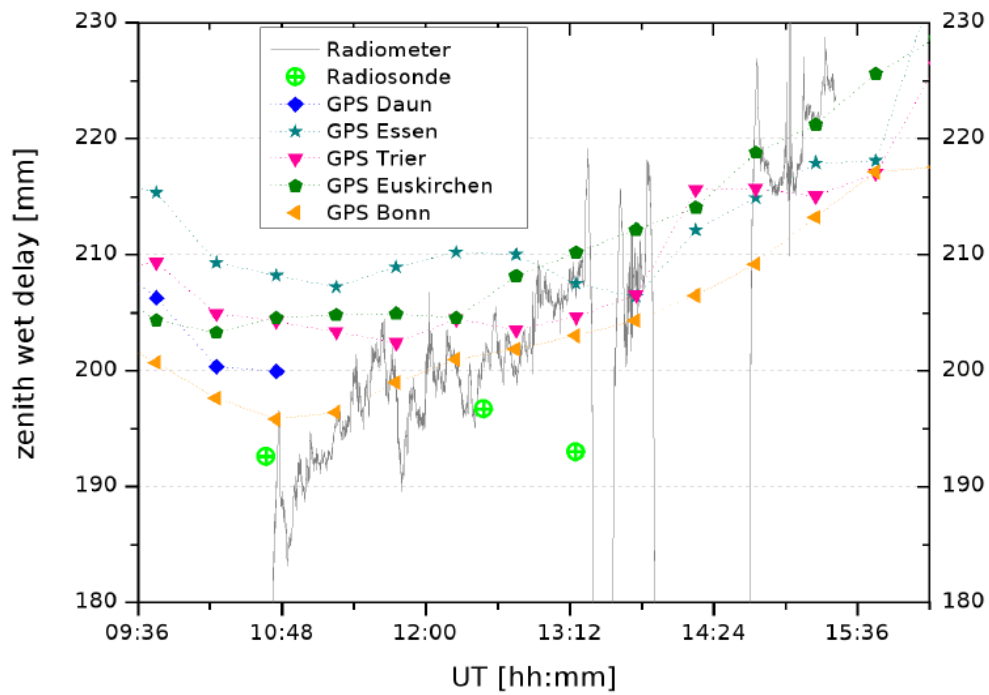


Figure 2-8. Comparison of ZWDs from the Effelsberg WVR (grey line), radiosondes (green circles), and GPS (other symbols): The final radiosonde had been lost due to communication problems, hence the corresponding point lies very low (Rottmann and Roy, 2007)

### 3. Numerical Weather Model and Radiative Transfer Model

Although the primary role of a numerical weather model (NWM) is to forecast weather states by assimilating data from meteorological sensors, NWMs have been used for various other applications. In the point of view of this study, the usefulness of NWMs is to provide meteorological profiles where radiosonde data are not available. Effelsberg has no periodic radiosonde observations that are available for the retrieval process. In order to satisfy the need of the meteorological profiles, a NWM is introduced instead of radiosonde observations. Several studies described below, reported NWM-derived wet path delays and possibilities of a NWM-aided retrieval.

According to Behrend *et al.* (2002), a NWM can be used for calculating the wet path delay. Niell and Leidner (2006) proposed using a NWM for retrieving wet path delay corrections. Tahmouh and Rogers (2000) also pointed towards the possibility of using more complex models, including multiple pressure layers, atmospheric profiling, and fitting of spectral irregularities. Böhm *et al.* (2006) updated the Vienna Mapping Function (VMF) using the 40 year reanalysis (ERA-40) data of the ECMWF (European Centre for Medium-Range Weather Forecasts) for the year 2001. In this study, ECMWF will be used as NWM to provide meteorological profiles over Effelsberg instead of radiosonde data.

As explained in chapter 2, several absorption models are commonly used as part of the radiative transfer (RT) model. Strictly speaking, an RT model should be distinguished from an absorption model because it contains a much broader spectrum of processes. In that respect, MonoRTM can be considered as a complete RT model that includes an absorption model. RT models can provide opportunities for calculating theoretical values of the brightness temperature and the water vapour amount by using meteorological profiles, which are assimilated in NWM.

In recent years, numerous RT models have been developed adopting different absorption models and spectral line databases. Melsheimer *et al.* (2005) presented inter-comparisons between newly developed RT models. Unfortunately, those models are not yet widely used. MonoRTM is currently one of the most commonly used RT models and has an independent history of development. Furthermore, it is an open source program package and is frequently updated with recent models. It provides various parameters including optical depth, radiance, and brightness temperature.

In this study, ECMWF and MonoRTM are employed as the NWM and the RT model for calculating theoretical measurements and readjusting wet path delays. Hereafter, an approach based on the two models will be referred to as ‘MonoRTM(ECMWF)’ or ‘the model’.

#### 3.1 ECMWF

NWMs from the ECMWF are often used, particularly on a global scale. These models provide meteorological profiles for temperatures, pressures, water vapour pressures, and geo-potential heights. Its horizontal resolution is approximately 25 km by 25 km. This horizontal dimension corresponds to the range of meso-scale meteorology. To figure out detailed or short-lasting changes in atmospheric water vapour, higher

resolution NWM are preferable. Nevertheless, the ECMWF model is employed for geodetic applications due to its general reliability.

Over Effelsberg, the daily and seasonal variability of the meteorological profiles from ECMWF are shown in figure 3-1 and appendix A.1. The profiles were provided by Johannes Böhm (2010). Each figure corresponds to each of the five geodetic VLBI sessions. Fortunately, the five sessions are evenly distributed in years as well as in seasons.

Each profile of the temperature and partial pressure shows different behaviour as it goes up to high altitude. While the patterns of the temperature profiles look similar to each other, independent of day and season, daily and seasonal variations of the partial pressure of water vapour are obvious. In most cases, the water vapour partial pressure is close to zero above an altitude of 7 km. This is the reason for having different scales between the temperature profiles and partial pressures profiles.

Figure 3-1 shows typical dry winter days. As can be seen in the figure, the amount of atmospheric water vapour is relatively small indicated by the WV partial pressure of 6 to 8 hPa near the surface. ECMWF profiles for the rest of the sessions are attached in appendix A.1. In appendix A.1, figure A.1-2 to figure A.1-4 show increased partial pressure near the surface. This is the typical distribution of water vapour in summer seasons. Figure A.1-4 shows an extremely humid day in May compared to figure A.1-1. These partial pressures are even higher than those of the summer profiles. In general, larger variations in partial pressure can be found on days of high humidity.

With sophisticated RT models, absorption coefficients and brightness temperatures can be calculated whenever profiles are provided. Here, the ECMWF profiles were used as input data for MonoRTM that is used as the RT model in this study. An overview and test results of MonoRTM will be shown in the next section.

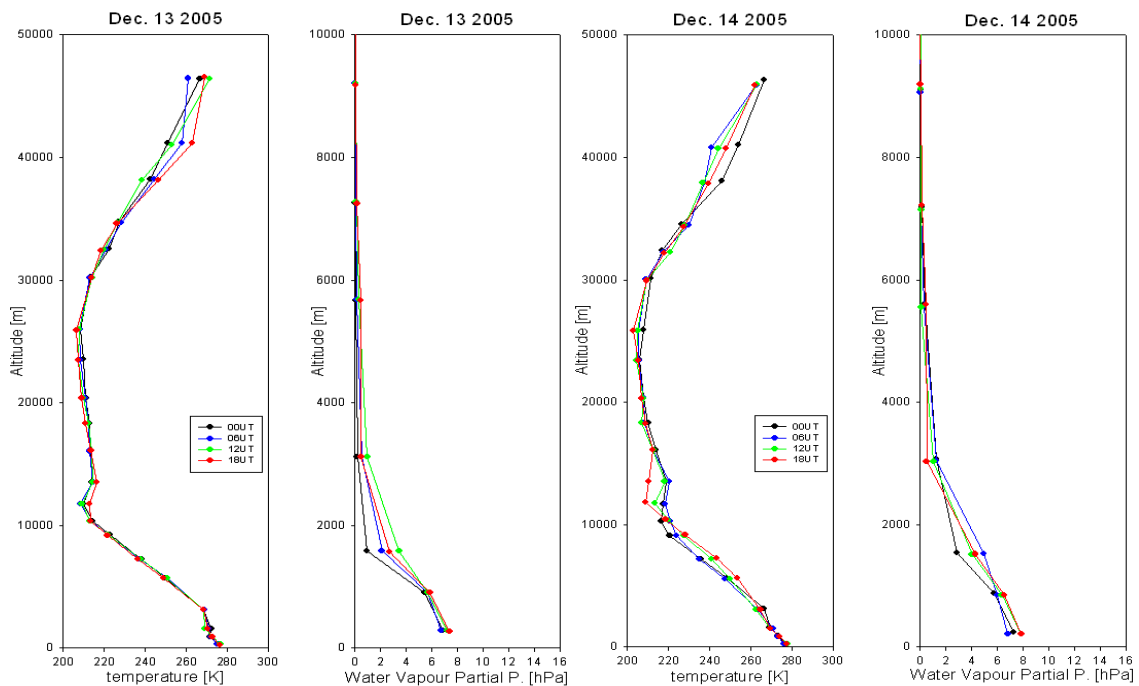


Figure 3-1. ECMWF profiles for temperatures and water vapour partial pressures over Effelsberg (13-14 Dec. 2005)

### 3.2 MonoRTM

When the state of the atmosphere is provided by measurements or NWM, the resulting brightness temperatures expected to be observed on the ground can be calculated with an RT model (Westwater *et al.*, 2004). The RT model can be used to infer the theoretical energy cascade of emitting and absorbing water vapour molecules. With this model-based energy budget, comparisons can be made with real measurements of the Effelsberg WVR. As mentioned above, the MonoRTM model is employed and will be explained in detail here.

In general, RT models describe interactions between atmospheric molecules, particularly for emissions and absorptions in the microwave region. The spectral line shape of the emission and absorption is determined by the distribution of atmospheric molecules and atmospheric states such as temperature and pressure. Thus, the amount of certain molecules can be acquired from the spectral line shape. Each model adopts a certain absorption model with improvements of the water vapour continuum absorption models still ongoing.

MonoRTM is a monochromatic model for the microwave region adopting the Humlicek Voigt line shape (Humlicek, 1982) and the MT\_CKD continuum absorption model (Mlawer *et al.*, 2004). This model is one of the most commonly used in climatology in recent years. It has advantages in both aspects of independent development history and employment of the latest advancements, while MPM models (Liebe *et al.*, 1987, 1989, 1993) and Rosenkranz models (1993, 1998, 2003) are partly related to each other because of an inter-dependent history of development. Moreover, MonoRTM includes contributions from other molecules such as ozone, nitrous oxide, and carbon monoxide, whereas the other two models only account for absorption due to water vapour, oxygen, and nitrogen.

MonoRTM originates from the Line-by-Line Radiative Transfer Model (LBLRTM; Clough *et al.*, 1992, 1995), which was developed by Atmospheric and Environmental Research (AER) Incorporate. It is an extended version of LBLRTM and is most appropriate for millimetre wave and microwave RT studies (Delamere *et al.*, 2004). One feature of the MT\_CKD model is that it has been compared extensively with simultaneous radiation and radiosonde observations near 20 and 30 GHz (Westwater *et al.*, 2005).

MonoRTM is a suitable program package for the calculation of radiances and/or brightness temperatures associated with absorption by molecules and cloud liquid water. Presently, MonoRTM version 4.2 source code is available at [http://rtweb.aer.com/monortm\\_frame.html](http://rtweb.aer.com/monortm_frame.html). Among several sub-programs of MonoRTM, the Monochromatic Optical Depth Model (MODM) is the core component of MonoRTM, dedicated to the calculation of the molecular optical depths. The latest features and data processing flow are summarised below. Most of the features were cited from Delamere *et al.* (2004) and the latest version and models added to MonoRTM were updated.

- Latest features of MonoRTM
  - Utilises the same physics and continuum model as the LBLRTM
  - Suitable for the calculation of radiances associated with absorption by molecules and

- cloud liquid water in the atmosphere
- Spectral validity only depends on the spectral region covered by the spectral lines provided in the line parameter database file (HITRAN\_2000)
- Uses the MT\_CKD version 2.4 continuum to include contributions from the far wings of the lines (Mlawer *et al.*, 2004)
- Includes line coupling effects, which are important for oxygen lines in the microwave region (Hoke *et al.*, 1989)
- Uses the Humlicek Voigt Line Shape (Humlicek, 1982)
- Cloud liquid water absorption is calculated using a model developed by Liebe, Hufford, and Manabe (1991).

As shown in figure 3-2, MonoRTM can adopt meteorological profiles as input files instead of general control parameters at the beginning.

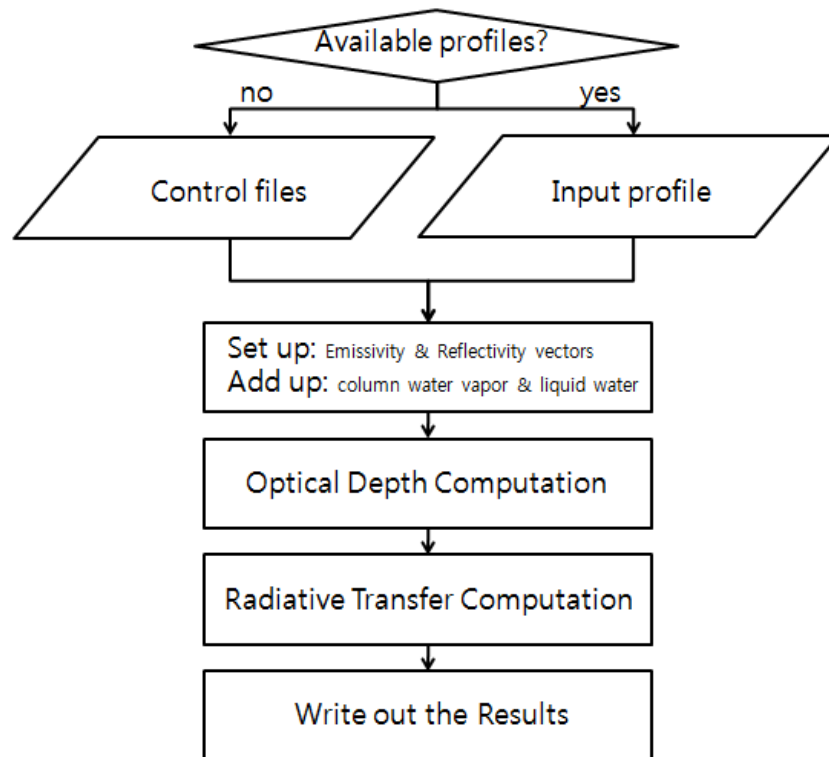


Figure 3-2. Block diagram of MonoRTM in terms of data processing flow

Figures 3-3 and 3-4 show the spectra of optical depth and brightness temperature as test results of MonoRTM before introducing ECMWF profiles. Figure 3-3 shows optical depth spectrum levels of the selective absorptions by water vapour (blue dashed line) and oxygen (green dashed line). As can be seen in the figure, the water vapour contribution is dominant in the frequency range between 18 to 29 GHz. Oxygen is of undoubted interest for remote investigations, since its abundance in the Earth's atmosphere up to altitudes of 100 km with a nearly constant quantity does not depend on seasonal conditions. The spectrum of the total optical depth (black line) is exactly the same as that of the US standard model, which is an option model of MonoRTM and

uses fixed values of pressure and temperature. Figure 3-4 shows the brightness temperature spectra where the US standard model (black line), mid-latitude Summer model (red line), and mid-latitude Winter model (blue line) were selected. Brightness temperatures show obvious variations with respect to seasons, changing roughly from 20 K to 60 K.

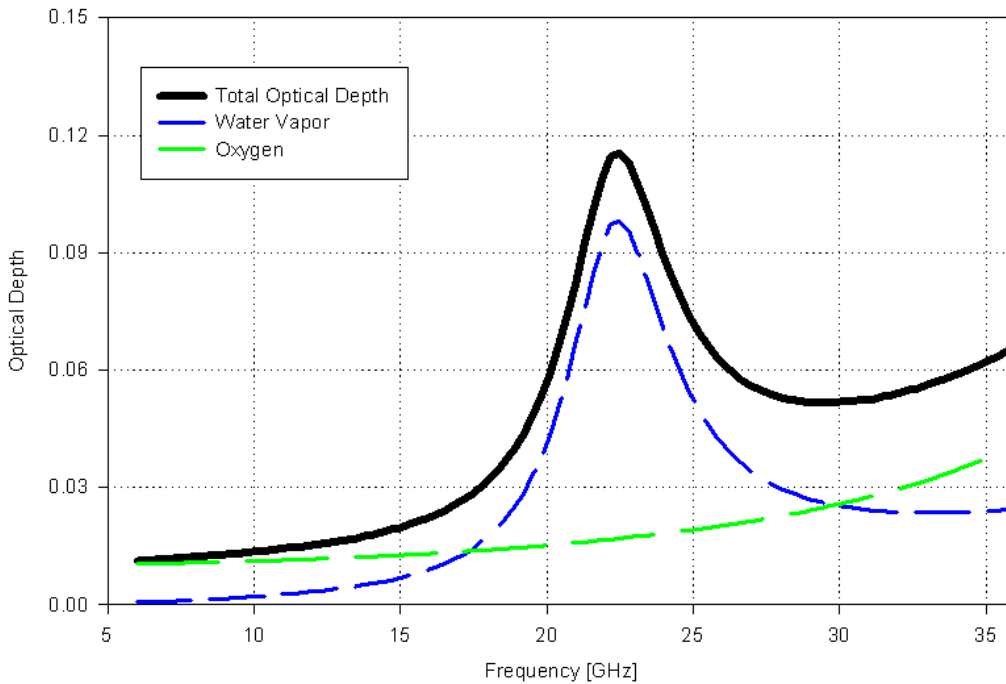


Figure 3-3. MonoRTM calculated optical depths from either water vapour, oxygen, or both (US standard model)

There are options for the self broadening and foreign broadening components, which are particularly important over the 30 GHz frequency range. In this frequency range, effects by liquid water and oxygen are more dominant than water vapour. To separate the broadening effects from the other effects, both components are switched-on for normal calculations. Both options were also applied to be switched-off, but the differences between normal calculations of the US standard model and combination of the two components were small for the frequency range that we are interested in. The comparison results are shown in figures 3-5 to 3-7.

Figure 3-5 shows the effects of neglecting the self component. The broadening effects of collision between water vapour molecules are relatively small in the 15 to 25 GHz frequency range. However, over 30 GHz frequency, it accounts for almost 5% of the optical depth of water vapour in figure 3-3.

Figure 3-6 shows the effects of neglecting the foreign component. The broadening effects of collision between water vapour molecules and other gas species molecules are relatively large, up to 25% at the most. The foreign component shows a small effect over the 30 GHz frequency range. Figure 3-7 shows the effects of neglecting both components. Effects from both components are not negligible, even for Effelsberg WVR. The WVR covers a frequency range between 18 GHz and 26 GHz that

corresponds to 25~50% of the broadening effects over 30 GHz. Both components were always switched-on during this study.

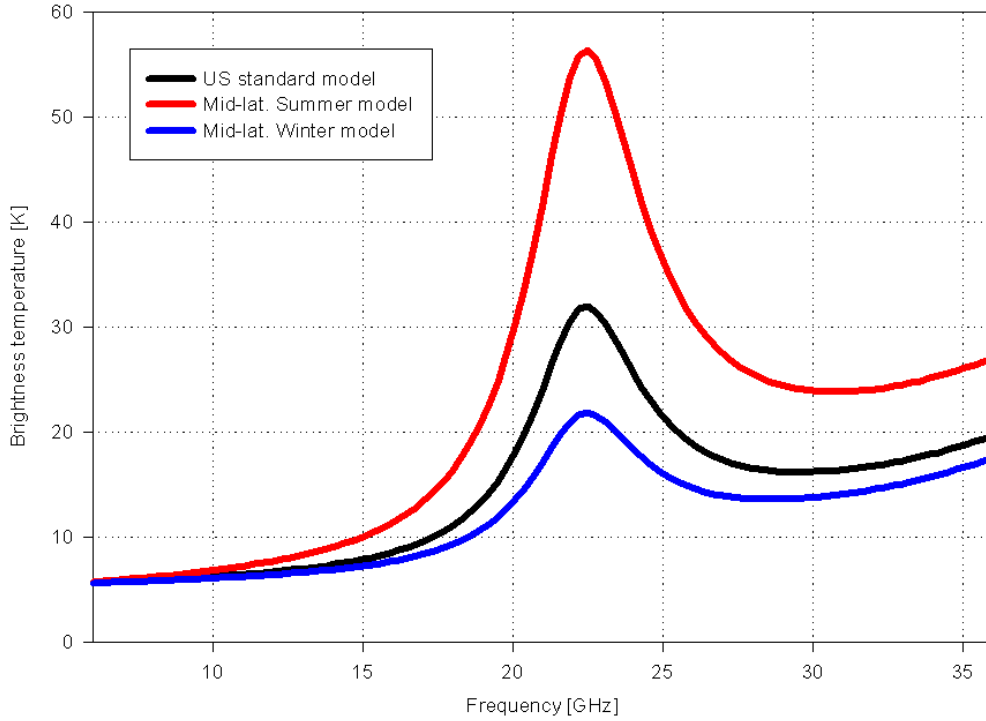


Figure 3-4. MonoRTM calculated brightness temperature corresponding to different models

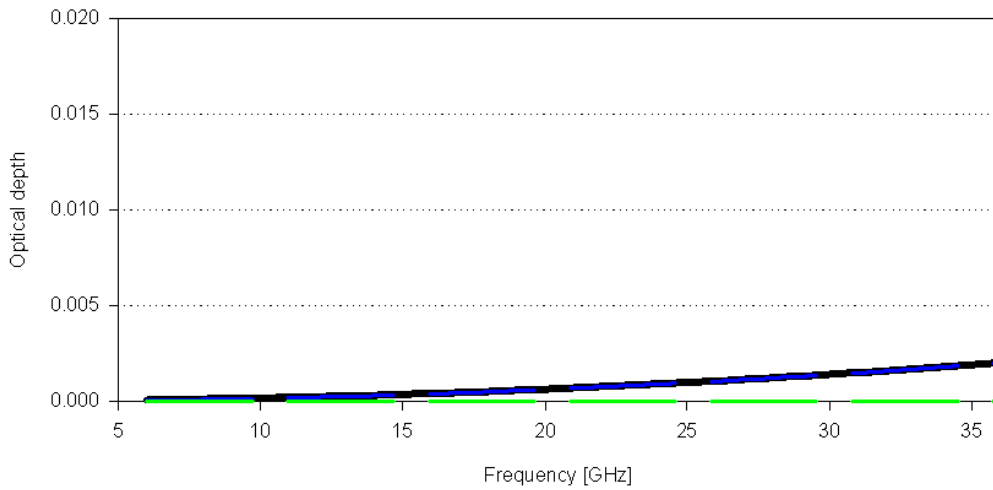


Figure 3-5. Differences (green) between normal calculation of US standard model (black) and the self component being switched-off (blue)

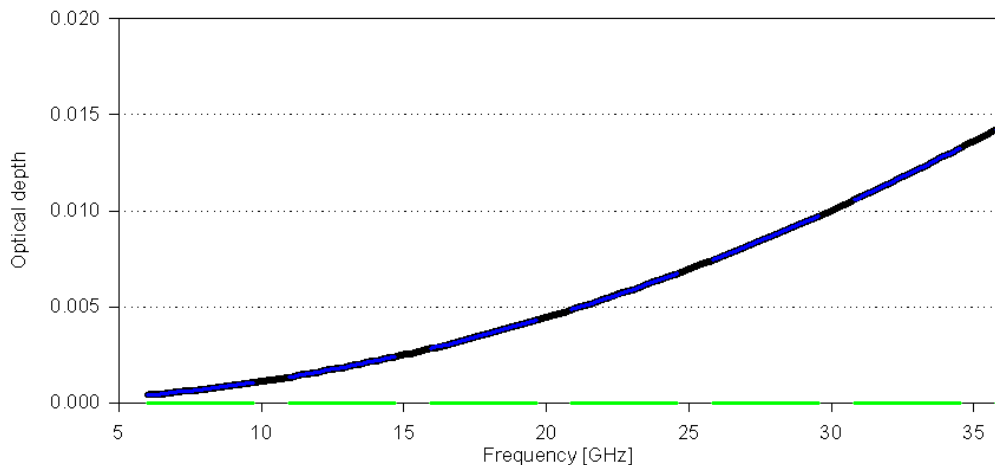


Figure 3-6. Differences (green) between normal calculation of US standard model (black) and the foreign component being switched-off (blue)

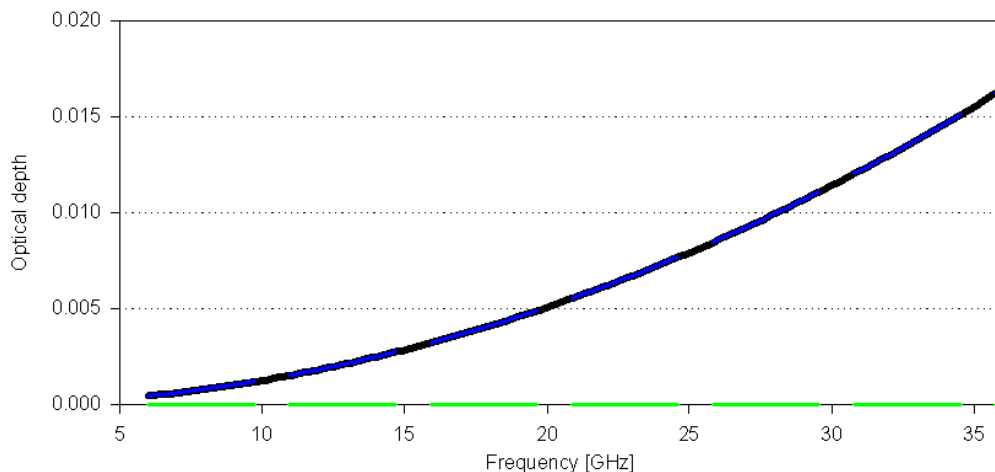


Figure 3-7. Differences (green) between normal calculation of the US standard model (black) and both components being switched-off (blue)

### 3.2.1 Profile mode

As shown in the first step of the block diagram in figure 3-2, there are two approaches for starting with the MonoRTM program. The first approach is using a control file as an input file. The control file includes all switches to activate the options available in the MonoRTM program package. This method is useful for comparisons between different models or status parameters. But it cannot provide results for a certain time and a certain place.

Another approach is using a weather profile as an input file. The MonoRTM program adopts a 20-layer-profile data format up to an altitude of 20 km. In addition, the input profile has a capacity of molecular density of several atmospheric constituents including nitrogen, oxygen, carbon dioxide, water vapour, etc. It is well known that absorption in the free atmosphere is mainly determined by selective absorption in oxygen and water vapour. Figure A.2-1 in the appendix shows the format of the first part of the profile.

Radiosonde observations or NWM assimilation data can be applied into the format



to create the input profile. As mentioned in the previous chapter, Effelsberg has no periodic radiosonde observations. However, the ECMWF model can provide a meteorological profile over Effelsberg. To create the input profile of MonoRTM, ECMWF based data were interpolated and transformed into the required format. For the column density transformation, the unit conversion functions which are provided by the Space Science and Engineering Center (SSEC), at the University of Wisconsin-Medison were used ([http://www.ssec.wisc.edu/~paulv/Fortran90/Profile\\_Utility/Introduction.html](http://www.ssec.wisc.edu/~paulv/Fortran90/Profile_Utility/Introduction.html)). The partial pressure of water vapour from ECMWF was transformed into the column density by layer using the unit conversion functions of SSEC. Table A.2-1 in the appendix summarises the integrated column density of water vapour for each session point.

### 3.2.2 Calculations

ECMWF provides four profiles at 00, 06, 12, 18 UT. Since the VLBI sessions normally cover the time between 17:30 UT to 17:30 UT on the next day, we will always present results for the eight epochs of the ECMWF epochs of the two full days covering the session. Optical depths from MonoRTM(ECMWF) are shown in appendix A.3. Calculated brightness temperature spectra are shown in the following figures. For each spectrum, ECMWF profiles were used as the input data. To compare MonoRTM calculated spectra (blue points) with Effelsberg's WVR observed brightness temperatures (red points), each figure includes two spectra.

While brightness temperatures are in the range of 15 and 25 K in winter, the range is between 35 and 60 K in summer. In most cases, disagreements were found in spectral shapes and peak brightness temperatures.

Figure 3-8 shows the spectra for clear skies typically found under dry air conditions. This sky condition is ideal for the cold sky calibration. MonoRTM calculations vary from 15 K to 25 K at peak points. In contrast to MonoRTM, Effelsberg's WVR observations vary from 10 K to 35 K. Several spectra have continuously increased wings from 22 GHz to 26 GHz, unlike those from MonoRTM.

As reported in the WVR log files, the internal temperature of the WVR set to 25°C was down to 13.7°C at 12UT, 13 Dec. 2005. Within three hours, the temperature was back to 23.3°C. This was probably caused by a temporary malfunction of the temperature control device. Since the temperature had been set to 25°C, the calibration parameters were directly applied for this temperature during the observations. Since the internal temperature variations affect the instrument gain, the resulting brightness temperatures are partly corrupted (A. Roy, personal communication, 2010). However, except for this abrupt temperature drop for a few hours, the WVR measurements of this session can be considered as not being contaminated by instrumental effects in terms of the cold sky and age of absolute calibration.

Figure 3-9 shows spectra of the 29 and 30 May 2006. MonoRTM calculations vary from 25 K to 35 K at peak point. In contrast to MonoRTM, Effelsberg's WVR observations vary from 10 K to 60 K. While several spectra agree within a few Kelvin, several spectra show large differences between MonoRTM(ECMWF) and WVR, particularly from 29 May 18UT to 30 May 12UT. Some of them have a similar shape in the high frequency range with several spectra of the previous session.

A possible reason for the discrepancies could be contamination by unknown instrumental effects (A. Roy, personal communication, 2010). The radiometer was recalibrated at 12 UT on 29 May, which is the start time of the Euro81 session. The log file also does not give any clear indications for the discrepancy.

Figure 3-10 shows spectra of the 3 and 4 July 2007. MonoRTM calculations vary roughly from 35 K to 50 K at peak points. The average levels are raised compared to the previous results. Considering 55 K of the mid-latitude summer model in figure 3-4, it appears to be dry summer days for this session. WVR observations show differences of a few Kelvin with respect to MonoRTM calculations at peak frequency. In contrast to the WVR observations in the previous session, the peak points are shifted from the nominal frequency (22.235 GHz) to a higher frequency. Furthermore, the WVR observations show saw-tooth features and some of them have wings in the high frequency range.

A possible reason for the saw-tooth features could be caused by poor calibration (A. Roy, personal communication, 2010). The poor calibration could be caused by the cold sky method because this method needs a clear and cold sky. However, this session was conducted in the summer and sky temperature measurements by elevation angle would not be exactly linear. This poor calibration is likely to cause biases. In addition, the observations were calibrated using the parameters determined on 29 May (5 weeks before). Although calibrations could normally be as old as a few months, this behaviour shows the weakness of infrequent calibrations. It would be preferable to have more frequent calibration, particularly for geodetic VLBI sessions.

Figure 3-11 shows the spectra of the 8 and 9 July 2008. MonoRTM calculations vary roughly from 40 K to 55 K at peak points. The average levels are raised compared to the previous session. Every spectrum from WVR observations shows a shape as it is expected. However, most of them have a comparably large bias with respect to MonoRTM calculations.

As reported in the WVR log files, only one day had elapsed between instrument calibration and the measurement of these spectra. This would explain the good quality in the shape, even considering the defect of the cold sky method applied in the summer. However, there are still questions remaining concerning several cases with large differences between MonoRTM(ECMWF) calculations and WVR observations. In-depth investigations were conducted whether the differences correspond to the differences between assimilated profiles from ECMWF and in-situ meteorology measurements. However, no evidence was found. Furthermore, wet path delay results from Effelsberg's GPS observations were analyzed which will be handled in the next chapter.

Figure 3-12 shows the spectra of 25 and 26 May 2009. MonoRTM calculations vary roughly from 45 K to 60 K at peak points. The average levels of the peak emission are raised compared with the previous session and it covered the most humid days of the five sessions. Every spectrum from WVR observation shows peculiarities over the 23 GHz frequency channels.

As reported in the WVR log files, the last recalibration was carried out on the 19 Feb. 2009. Drifted gains during three months amplify the affect on the whole spectra. In

addition, it was found that the drifts were occurring more regularly at high frequency over 23 GHz.

Due to the unstable performances of the WVR, mainly due to the infrequent calibration, the original intention of selective classifications based on brightness temperatures from the WVR and MonoRTM(ECMWF) could not be achieved. Brightness temperatures at peak frequency from the WVR observations and MonoRTM calculations are shown in figure 3-13 and table A.4-1 in the appendix. For direct comparison, the peak frequency of the WVR at 22.233 GHz was used, which is slightly different from the nominal peak frequency of 22.235 GHz.

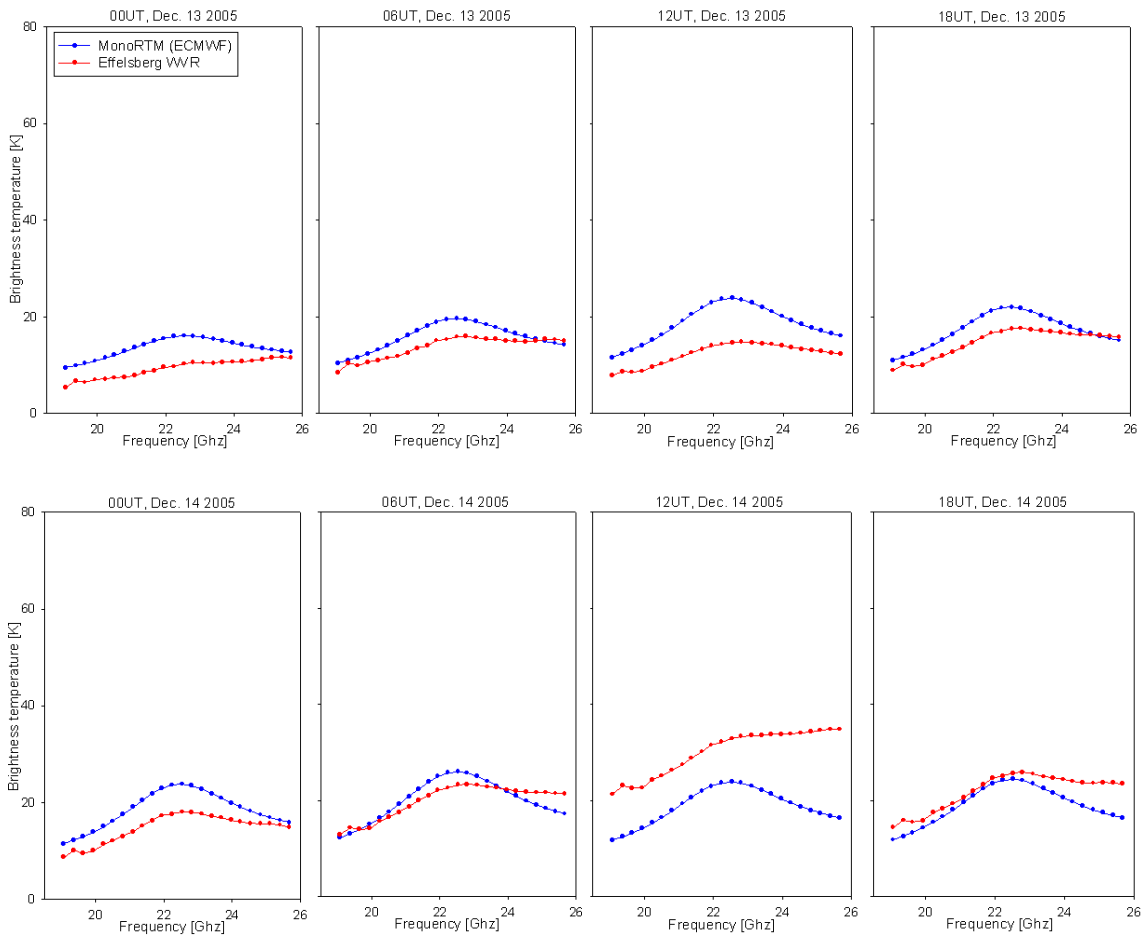


Figure 3-8. Brightness temperature spectrum comparison between MonoRTM(ECMWF) and WVR (13-14 Dec. 2005)

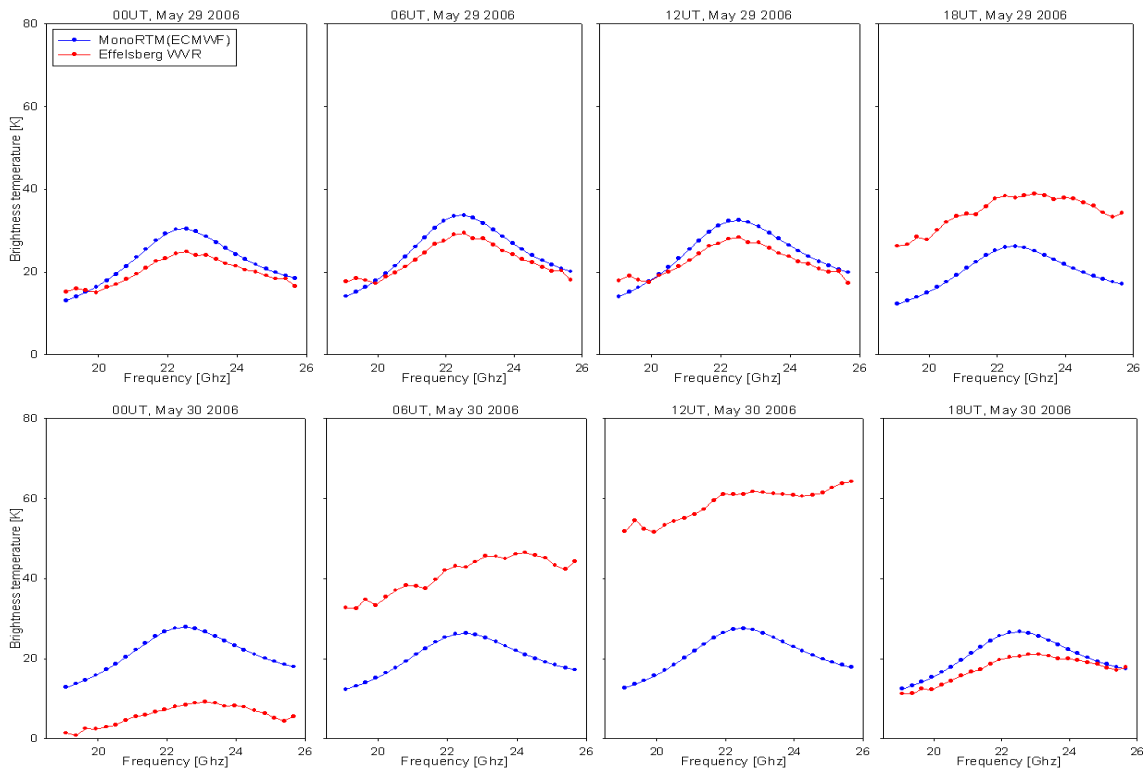


Figure 3-9. Brightness temperature spectrum comparison between MonoRTM(ECMWF) and WVR (29-30 May 2006)

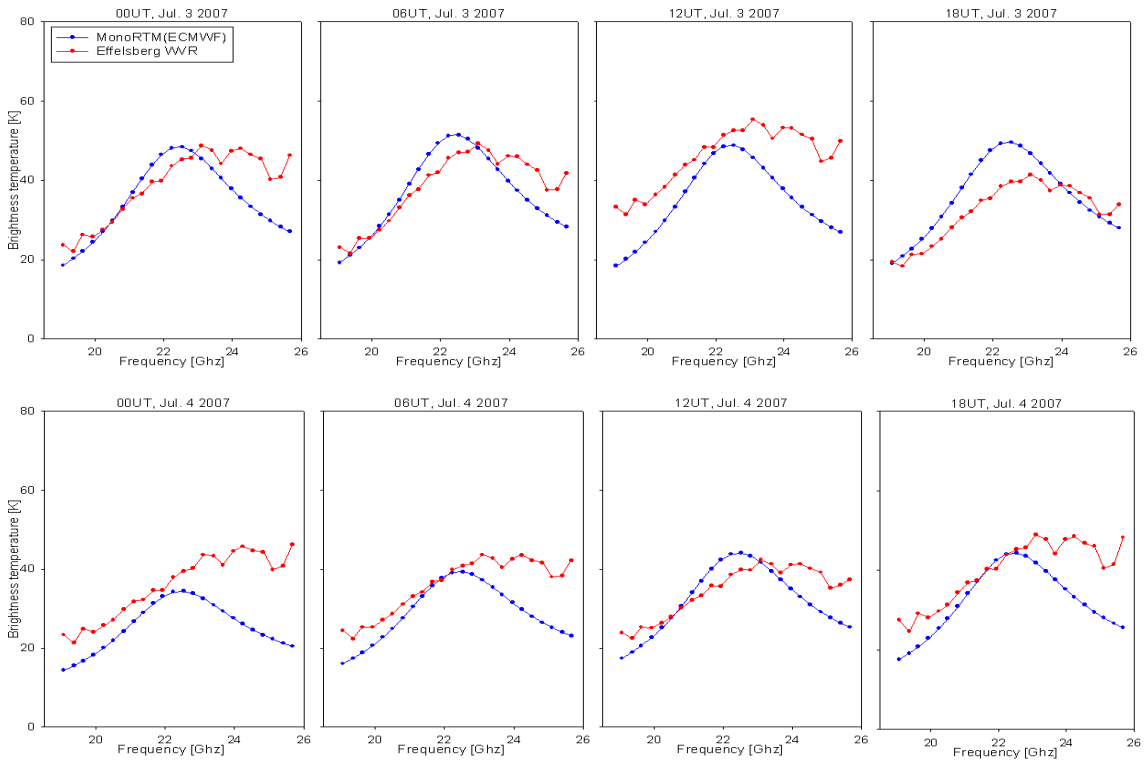


Figure 3-10. Brightness temperature spectrum comparison between MonoRTM(ECMWF) and WVR (3-4 Jul. 2007)

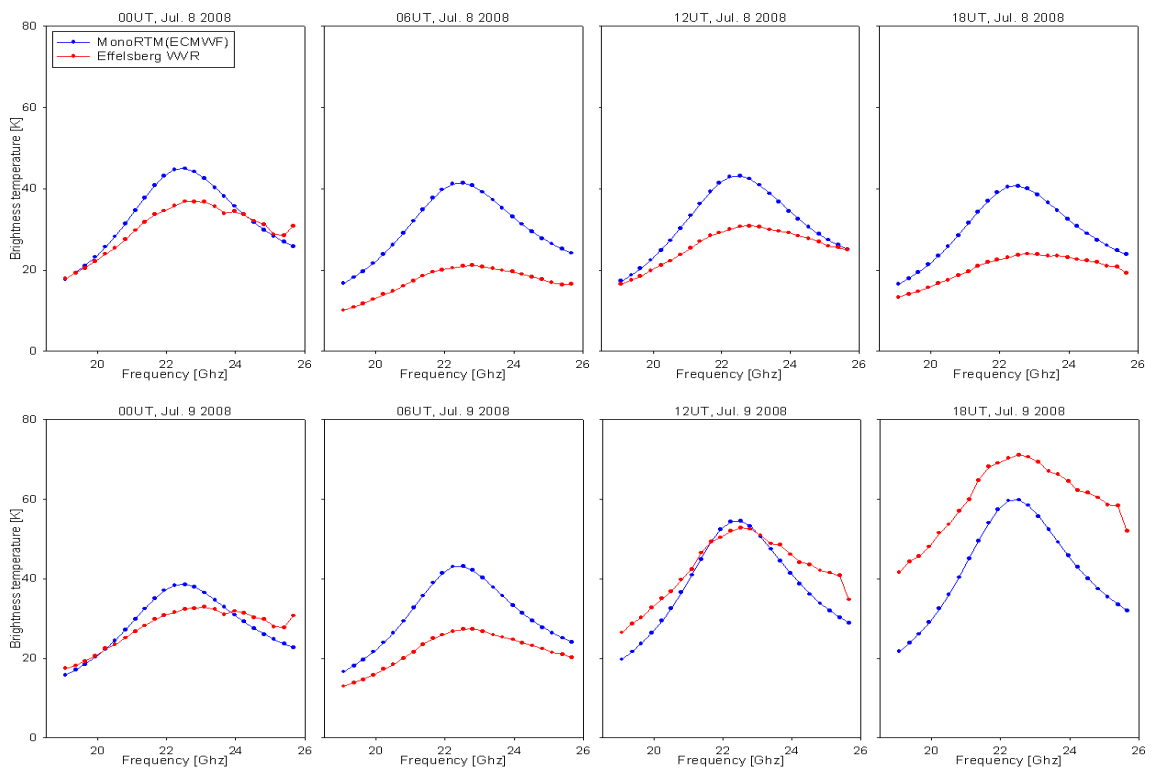


Figure 3-11. Brightness temperature spectrum comparison between MonoRTM(ECMWF) and WVR (8-9 Jul. 2008)

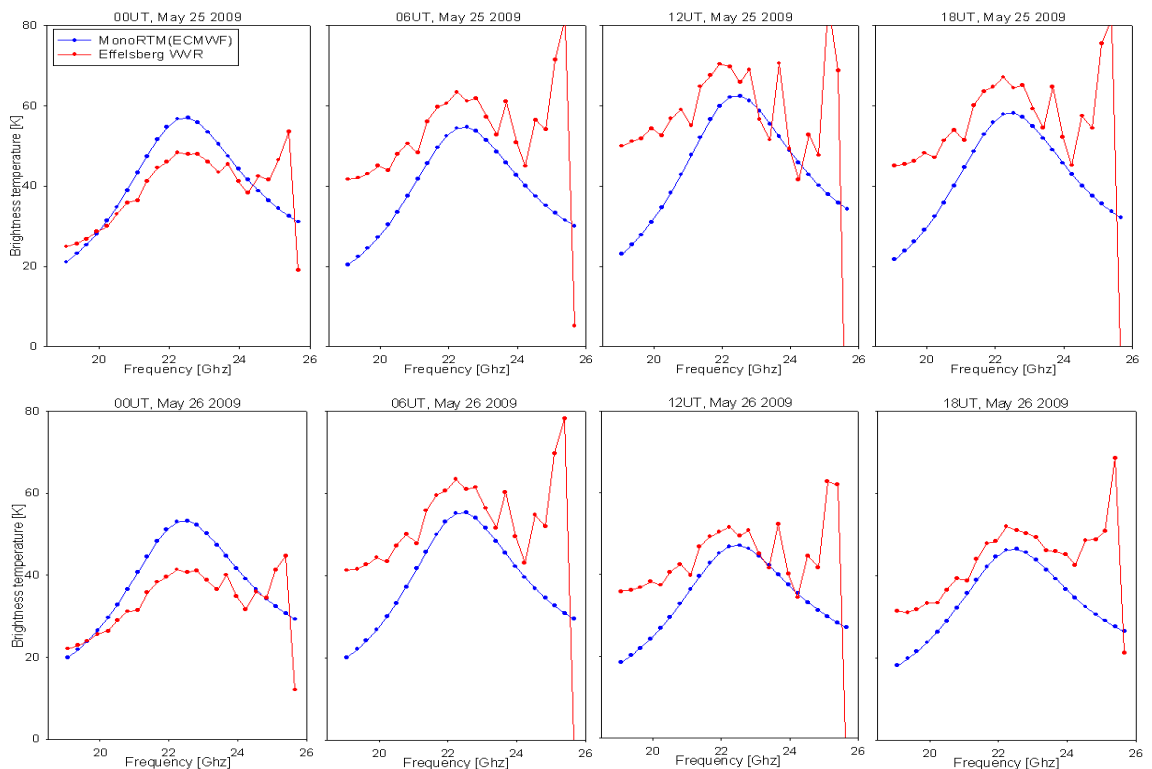


Figure 3-12. Brightness temperature spectrum comparison between MonoRTM(ECMWF) and WVR (25-26 May 2009)

As can be seen in figure 3-13 and table A.4-1, the variations in peak temperatures from the model and the WVR are approximately 40 K and 70 K, respectively. Differences between peak temperatures from both are in the range -21 K to 34 K with respect to the model calculations. This relative variation is approximately 55 K larger than the model variation itself. This large variation seems mainly to be caused by several points in the second and fourth sessions. If those points are excluded, the variation range will be reduced. In order to make a solid judgement for the exclusion, the RMS for all channels in the table can be used. The RMS values represent the level of similarity between spectra from the WVR and the model at each epoch. In terms of mean RMS of all the epochs, sixteen peak temperatures from the WVR go along with larger RMS. Among them, thirteen are higher than the models and three are lower. If these sixteen points are excluded, the peak temperature differences between the WVR and the models are reduced to a range from -16 K to 1 K. After the outlier exclusion, a negative bias of the WVR in peak temperature is dominant. Although there is a negative bias of the WVR, this range of variation is acceptable in the sense of differences between the in-situ measurements and the model calculations.

Based on the comparisons between brightness temperatures from the WVR and the model, differences in peak temperatures and spectra shape similarity are investigated. It was expected that the peak temperature difference is mainly caused by instrument calibration, and that the dissimilarity is mainly caused by instrument malfunction. In contrast to the expectation, most newly recalibrated sessions show most of the large differences at peak temperatures. The WVR for the two sessions in 2006 and 2008 were calibrated a day before the VLBI campaign. Nevertheless, the two sessions show the greatest differences among the five sessions. A possible reason for the large differences are unexpected parameter changes, such as receiver temperature and gain or weather events such as dew or rain. The last session seems to suffer from both from old-aged calibration and the malfunction of the WVR. The WVR for this session in 2009 was calibrated three months before the VLBI campaign, and the high frequency channels are contaminated by instrumental effects. Six out of the sixteen outliers are involved in this session.

As a summary of this section, brightness temperatures from the models are compared with the WVR measurements. After the outlier exclusion, the WVR measurements are in the range of 50% and 100% of the model calculations. The reasons for the outliers have not yet been uncovered. However, it is obvious that both old-aged calibration and the malfunction of the instruments produce such outliers.

MonoRTM calculations of optical depths are only dependent on input profiles. In other words, the precision of the results is dependent on the precision of the input data. To determine the error propagation through MonoRTM, several cases were tested. Errors of one percent of the total initial value were added to the temperature and water vapour partial pressure. As a result, the effects of the added error to the water vapour partial pressure were larger than those of the temperature. Detailed information of this will be presented in the next section.

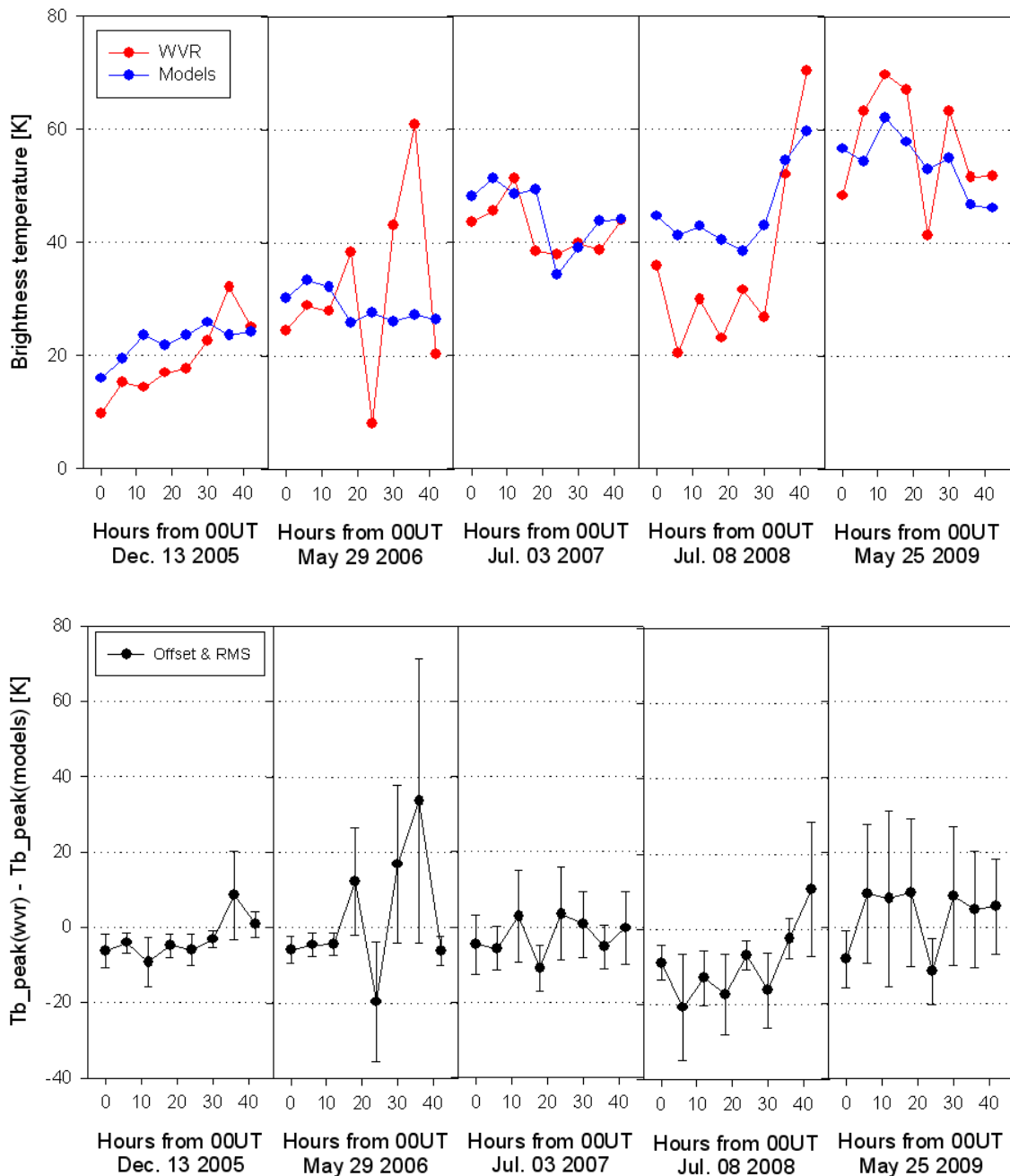


Figure 3-13. Comparison of peak brightness temperatures from the WVR and the models (top) and its offset and RMS for all channels (bottom)

### 3.2.3 Error propagation

To quantify the effects of input data from ECMWF, one percent of error was added to the water vapour partial pressure and atmospheric temperature for each layer. Using the error-added data as the input profile of MonoRTM, the effects of the error increment were quantified in terms of optical depth and brightness temperature. For the test, a few selected optical values have been chosen. According to the radiative transfer theory, i.e. the cascade process to line-of-sight, water vapour amount is not directly proportional to opacity and brightness temperature.

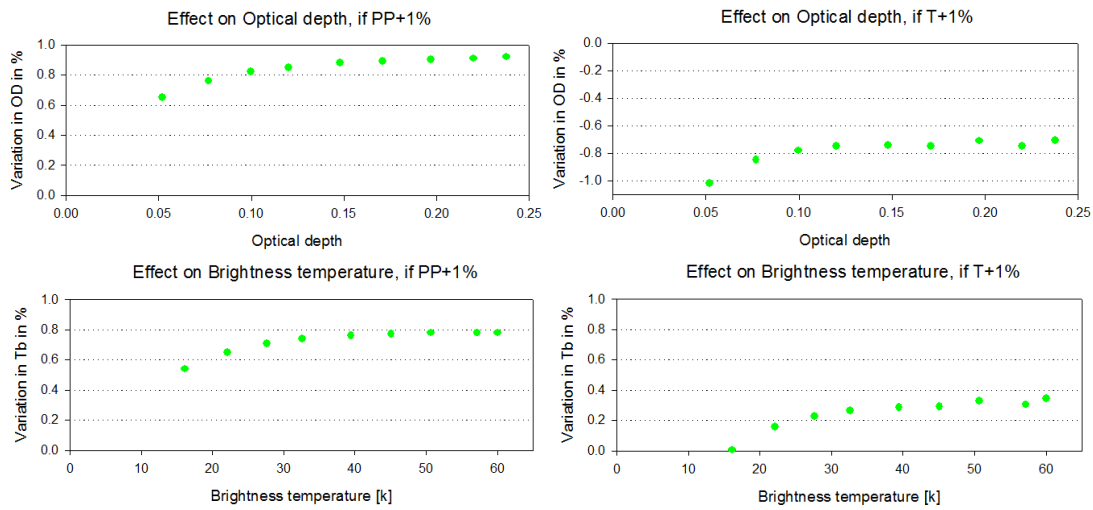


Figure 3-14. Effects of 1% error increments on water vapour partial pressure (left) and temperature (right) provided by ECMWF

As can be seen from figure 3-14, the errors in temperature and partial pressure cause asymptotic approaches to a certain threshold. For the water vapour partial pressure, these are 1% and 0.8% for optical depth and brightness temperature, respectively. For the air temperature, these are  $\sim -0.7\%$  and  $\sim 0.3\%$  for optical depth and brightness temperature, respectively. So, the effects of errors of water vapour partial pressures are larger in total than those of atmospheric temperatures on both optical depth and brightness temperature. This behaviour results from the cascade process in the radiative transfer model. It can be concluded that the partial pressure has to be determined with a much better accuracy than the air temperature.



## 4. Wet Path Delay Comparisons and Readjustments

The retrieval of wet path delays is the key process in the geodetic applications with WVR instruments. In the previous chapter, two different approaches were used to compare brightness temperatures over Effelsberg. One is in-situ measurement using the WVR and the other is theoretical calculations using MonoRTM(ECMWF). The former approach provides brightness temperature measurements and zenith wet delay conversions using the retrieval algorithm of Tahmoush and Rogers (2000), whereas the latter approach provides brightness temperature calculations and precipitable water (PW) estimates.

In order to directly compare the ZWD conversions with the PW estimates, a transformation from PW to ZWD is necessary. There are well-known coefficients presented by Bevis *et al.* (1994) for the transformation (see appendix A.5). The coefficients, which correspond to the ZWD/PW ratio, are in the range between 6~7 under normal weather conditions. In order to verify the transformed ZWDs using the coefficients, a method of layer summed ZWD was introduced (see section 4.2).

As an independent water vapour sensing technique with respect to the two approaches, GPS was chosen for comparisons in this study. In recent years, it is widely accepted that GPS derived ZWD is an accurate and reliable quantity reflecting the total amount of atmospheric water vapour. Wang and Zhang (2008) adopted GPS PW as a reference, even for comparisons with radiosonde data. In this study, GPS-derived ZWDs will be used as the reference in comparison with other ZWDs. From the comparison, a benefit of the model calculations will be shown in terms of generating reliable ZWDs.

Although the WVR has defects in the cold sky method and the infrequent instrument calibration, its observations include data for every single scan of the five sessions. In contrast, MonoRTM(ECMWF) has a benefit in generating reliable ZWDs whereas it can just provide four data points per day. To exploit the advantages of the WVR and the benefit of the model calculations, we will introduce a readjustment procedure by applying offset corrections based on the mean differences between the WVR observations and models calculations. This method can be used for the improvement of ZWDs from the WVR because the model calculations do not include any calibration effects.

In addition to the WVR-measured ZWDs, readjusted ZWDs and smoothed ZWDs are shown in this chapter. Effects of the three sets of ZWDs on geodetic parameters, such as baseline repeatability and height precision, will be discussed in the following chapters.

#### 4.1 Wet path delays from the WVR at Effelsberg

The following equations regarding the retrieval of the scanning water vapour radiometer are based on Tahmoush and Rogers (2000). Cruz *et al.* (1998) introduced the absorption coefficient described by equation (4.1)

$$k_f = 4.5671 \times 10^{-4} \left(\frac{300}{T}\right)^{3.5} \cdot \exp\left[2.143 \left(1 - \frac{300}{T}\right)\right] p_f f^2 \times \left(\frac{\Delta f}{f_0}\right) \left[\frac{1}{(f-f_0)^2 + \Delta f^2} + \frac{1}{(f+f_0)^2 + \Delta f^2}\right] \quad (4.1)$$

$$\Delta f = 2.784 \times 10^{-3} \left[p \left(\frac{300}{T}\right)^{0.6} + 4.8 p_f \left(\frac{300}{T}\right)^{1.1}\right] \text{ GHz}$$

Where,  $f$  is the frequency in GHz,  $f_0$  is 22.23510 GHz,  $p_f$  is the partial pressure of water vapour in mbar,  $p$  is the pressure of dry air in mbar, and  $T$  is the temperature in K. The relationship between observed brightness temperature and wet path delay can be derived as below. The opacity is given by

$$\tau = \int k_f dl \quad (4.2)$$

The path delay due to refractivity  $N$  (in units of parts per million) of water vapour is given by

$$d = 10^{-6} \int N dl \quad (4.3)$$

According to Thayer (1974),  $N$  of water vapour is related to the water vapour partial pressure  $p_f$  and temperature  $T$ .

$$N = 3.776 \times 10^5 \frac{p_f}{T^2} \quad (4.4)$$

Assuming water vapour in a thin layer and at constant temperature  $T$  and dry air pressure  $p$ , the relationship between the path  $d$  and the brightness temperature  $T_B$  is given by

$$d = \frac{3.776 \times 10^5 p_f T_B}{k_f T^3} \text{ mm} \quad (4.5)$$

Conversion factors by Tahmoush and Rogers can be described

$$\frac{d}{T_B} = \frac{3.776 \times 10^5 p_f}{k_f T^3} \text{ mm/K} \quad (4.6)$$

From the simulation of equation 4.6, the conversion factors are in the range of 4.0 and 5.0 under normal conditions.

As mentioned in chapter 3, ECMWF profiles are only available at 00, 06, 12, 18 UT. For better comparison, ZWDs provided by Effelsberg telescope staff are averaged for ECMWF epochs. Figure 4-1 shows an example of averaged ZWD for a six-hour-long

interval which is the total of three hours backward and three hours forward with respect to the ECMWF epoch. Figure 4-2 shows the averaged ZWDs. They are in the range between 20 and 220 mm. As mentioned in previous chapters, several spectra of brightness temperature were contaminated by the cold sky method and the infrequent calibration. Considering these defects of the WVR, the ZWDs seem to be modified in a certain way because the instrument parameters presumably used in the retrieval were out of date for many sessions. In this respect, the model based approach in the next section would provide a solution for improving the ZWDs by using the offset and the rate between the WVR observations and the model calibrations. This approach has the advantage of avoiding the effects of instrument calibration.

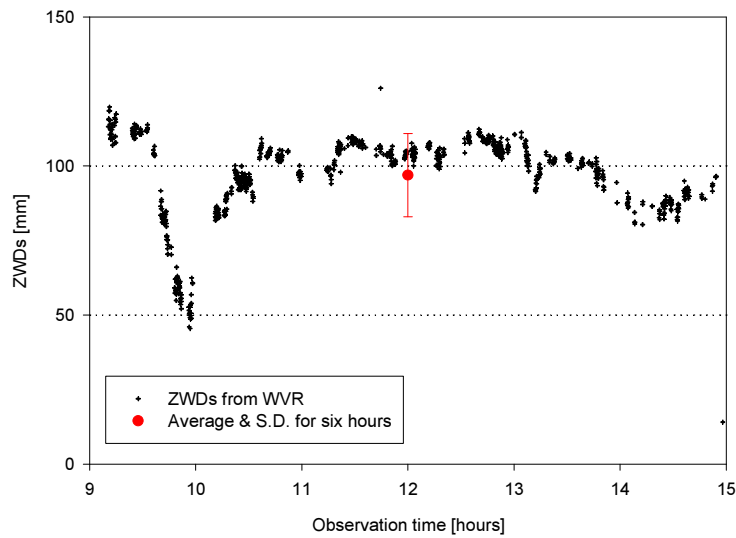


Figure 4-1. An example of the averaged ZWD for one ECMWF epoch (12UT, Jul. 3 2007)

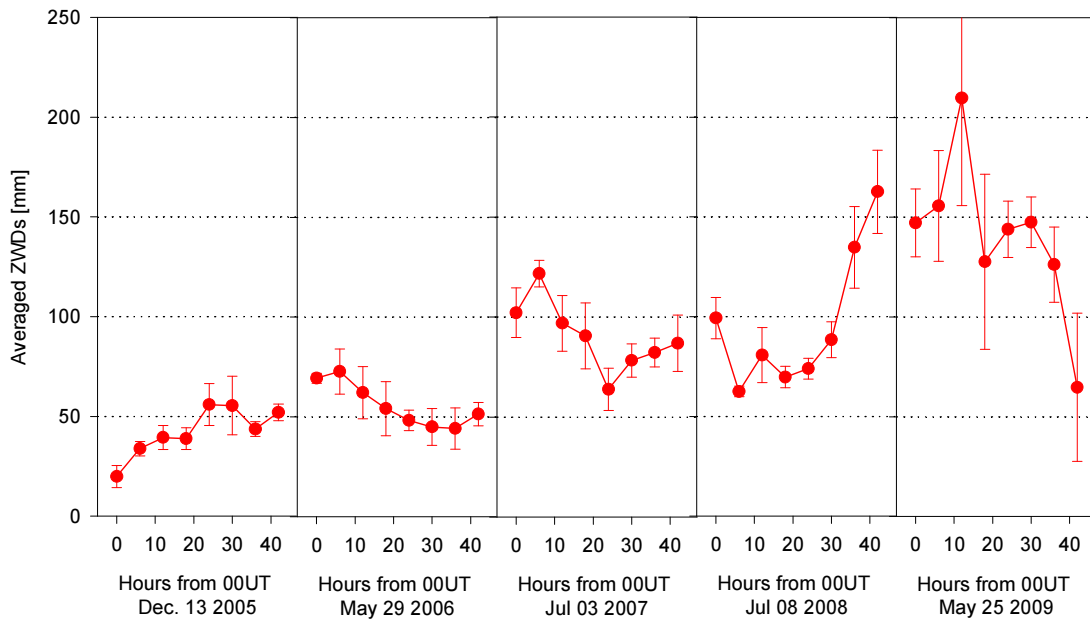


Figure 4-2. Averaged ZWDs from the WVR at Effelsberg

## 4.2 Wet path delays from MonoRTM(ECMWF)

ZWDs from MonoRTM(ECMWF) will be presented in this section. In addition, another set of ZWDs derived from an independent method (mentioned previously as the ‘layer-summed method’) will also be presented for validating the ZWDs from the models. Unfortunately, MonoRTM version 4.2 only provides PW instead of ZWD. To compare ZWDs with other approaches, PW needs to be transformed into ZWDs.

Bevis *et al.* (1994) achieved the transformation between PW and ZWD. They found coefficients whose magnitude is a function of a certain constant related to the refractivity of moist air and of the weighted mean temperature of the atmosphere. The water vapour weighted atmospheric mean temperature is a key parameter in the transformation. But the mean temperature shows variations to location, particularly in latitude. This is an uncertainty when transformation coefficients are introduced. In the global range, the ratio of ZWD/PW has values between 5.8 and 7.3. In the mid-latitude range, however, its range becomes ~6.0-6.7. According to the surface temperature of Effelsberg for the five sessions, the range between 6.1 and 6.5 were used in the transformation. Details of the calculation are in appendix A.5.

As can be seen in table A.4-1 in the appendix, PW values from MonoRTM(ECMWF) are in the range between 5 mm and 32 mm. The transformation factors are determined by the surface temperature at Effelsberg and multiplied to transform into ZWDs. As can be calculated from the equation of the transformation factors in the appendix, 1 K of mean temperature causes an approximately -0.2 change in the factor, and it also affects the transformed ZWDs. The mean temperature is calculated from the surface temperature measured at the Effelsberg weather sensor.

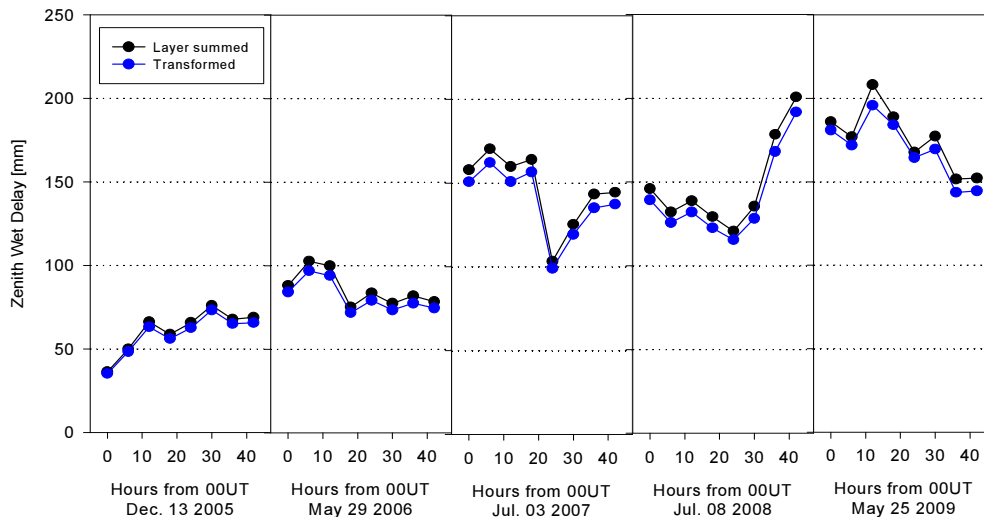


Figure 4-3. Comparison between the transformed ZWDs and the layer-summed ZWDs

To verify the transformed ZWDs, the layer-summed ZWDs were calculated for each layer using equations (4.1) to (4.4). Then the path delays are summed. Appendix A.6 summarises the layer-summed method. The ZWDs from the two different methods are compared in figure 4-3. The figure shows good agreement between the two ZWDs, with a 5.6 mm offset on average. The main reason for the offset presumably is the use of

different absorption models.

The top of figure 4-4 shows comparisons between ZWDs from the two approaches; the WVR measurements and the model calculations. The blue points are the transformed ZWDs from MonoRTM(ECMWF). The red points are ZWDs from the WVR. It is obvious that ZWDs from WVR are always smaller except for one epoch at 12UT 25 May 2009. In the case of the fifth session, most of the noisy behaviour might come from poor instrument calibration. As can be seen in the figure, ZWDs from WVR are in range between 20 and 210 mm, while ZWDs from MonoRTM(ECMWF) are in the range between 40 and 200 mm. But this comparison does not give any solid foundation to determine whether one is more reliable than the other. In the next section, GPS-derived ZWDs will be used as a reference for the comparison.

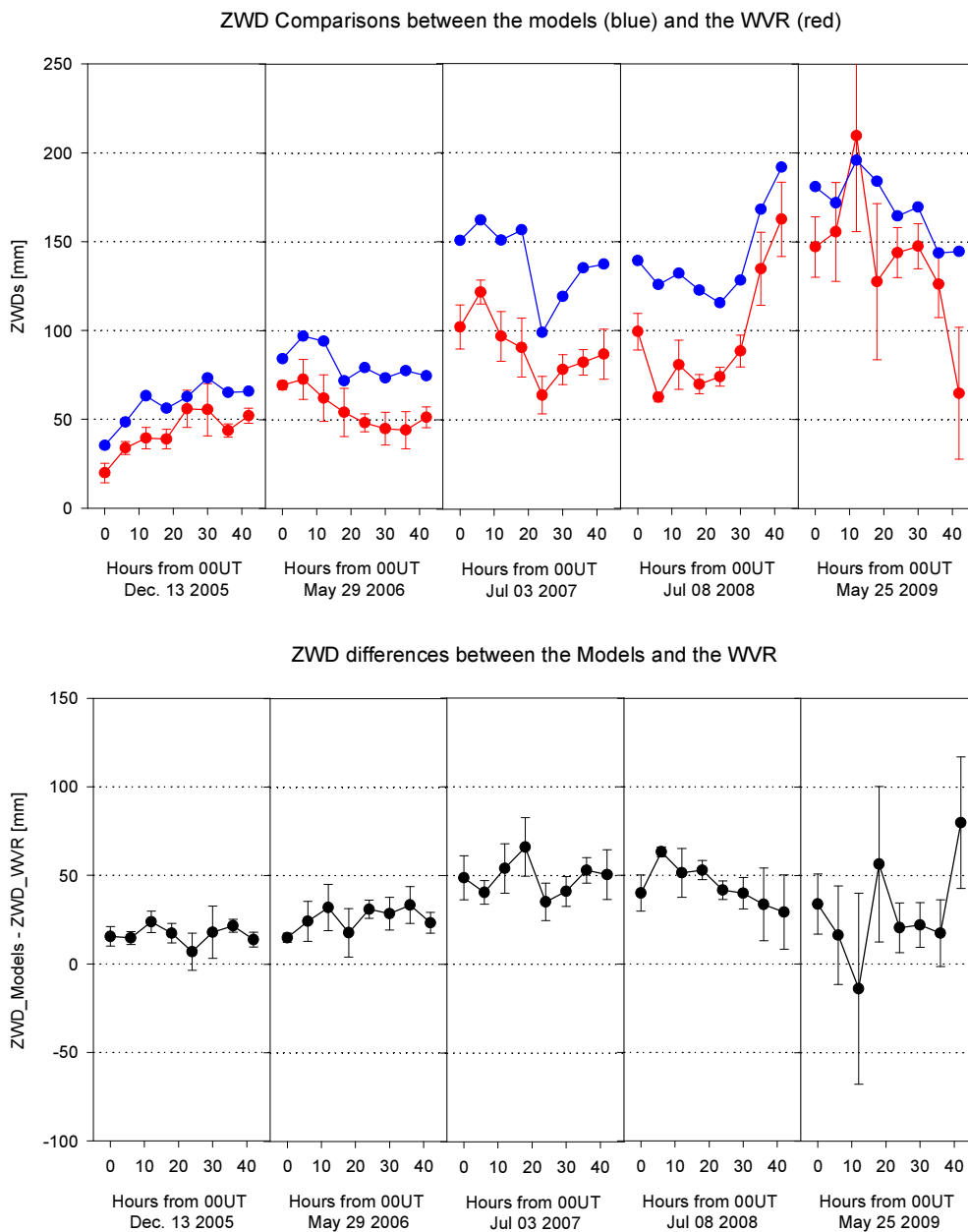


Figure 4-4. Comparison between ZWDs from the two approaches and its differences

### 4.3 Comparison with GPS-ZWDs

In order to make a judgment on the reliability of the ZWDs from the two approaches presented in the previous section, ZWDs derived from GPS at Effelsberg were used for the comparison. The GPS station at Effelsberg has been regularly operating since 2007. Thus, the last three sessions out of the five sessions are used in the comparison. The GPS antenna is on a steel mast, which is located on the roof of a building across from the 100 metre radio telescope. The height difference between the GPS antenna and the VLBI reference point of the telescope is approximately 13 m, with the VLBI reference point being higher than the GPS antenna.

This height difference causes an offset in the ZWD comparisons. If we remind ourselves about the tendencies of the water vapour profiles in the previous chapter and the ZWDs from the two approaches, it is possible to roughly estimate the offset. From the ECMWF profiles, one can determine that an average water vapour partial pressure decreases continuously from zero up to 5000 m in altitude. One can also determine that the average of the ZWDs is approximately 100 mm. Then, this yields an offset per metre of roughly 0.02 mm near the surface. A similar assumption had been made by Coster *et al.* (1996). The second possible estimation can be achieved by using general features of decrease rates of ZTD and atmospheric pressure, which are known as 2.3 mm per hPa and 1 hPa per 8 m, respectively. In this case, the ZWD's offset per metre is 0.03 mm, reminding us that ZWD is roughly 10% of ZTD. From the assumptions, it is found that a 13 m height difference causes a 0.26~0.39 mm offset in ZWD. Although the estimated offset is small, it should be used to correct GPS-derived ZWDs for direct comparison.

Many studies have presented ZWD inter-comparisons between water vapour monitoring instruments such as radiosonde, GPS, WVR, and VLBI (Linfield *et al.*, 1997; Niell *et al.*, 2000; Gradinarsky *et al.*, 2000; Haefele *et al.*, 2004; Nothnagel *et al.*, 2007; Zhang *et al.*, 2008). Behrend *et al.* (2000) extended the comparison to numerical weather models (NWM). He showed that GPS has a higher correlation to NWM than VLBI.

Figure 4-5 shows ZWDs from GPS, MonoRTM(ECMWF), and the WVR. The first set of eight points corresponds to Euro88. The sessions used in this study are reduced to the last three sessions according to the availability of the GPS data. GPS-derived ZWDs are provided by GeoForschungsZentrum (GFZ). As can be seen in the figure, ZWDs from GPS and MonoRTM(ECMWF) agree well, while ZWDs from the WVR are biased from the other two. Average offsets and standard deviations of MonoRTM(ECMWF) and WVR with respect to GPS are  $-4.3 \pm 11.0$  mm and  $-44.8 \pm 24.0$  mm, respectively.

Even if one considers continuously changing positions of the WVR with respect to the reference point according to the VLBI observation schedule every several minutes, the offset is too far away from GPS-derived ZWDs. Even if one considers the changing positions in height, it is just a few millimetres at most. In contrast to the WVR, MonoRTM(ECMWF) shows good agreement in terms of the offset and the deviation because the first layer's data of the ECMWF profiles were corrected to be started from the reference point in height. Those statistics are comparable to results by Behrend *et al.* (2002). They presented  $-2.7 \pm 14.3$  mm for the offset. It can be presumed that the relatively large offset and deviation between ZWDs from the WVR and GPS probably

came from the defects of the WVR. Internal temperature variation of the WVR affects instrument gain and the calibration parameters (A. Roy, personal communication, 2010). Detailed investigations will be considered in chapter 5.

Figure 4-6 shows ZWD correlations between the WVR, MonoRTM(ECMWF), and GPS. It is obvious that the correlation between MonoRTM(ECMWF) and GPS is 0.822, which is higher than the 0.624 between the WVR and GPS. In addition, slope values can be used for the investigation of agreement level with respect to GPS-derived ZWDs. In cases where the slope of the two sets of ZWDs is close to one, these ZWDs are in a relationship of one to one correspondence.

For the slope comparison, the standard error of each slope was calculated. While ZWDs from the model show  $0.91 \pm 0.09$  of slope and standard deviation with respect to ZWDs from GPS, ZWDs from the WVR show  $1.19 \pm 0.19$ . Considering the standard deviations, the model covers a slope range from 0.82 to 1.0 and the WVR covers a slope range from 1.0 to 1.38. Although both include 1.0 within their slope coverage ranges, the model has the closer relationship of one to one correspondence in terms of mean slope and deviation from a 1.0 slope line.

From the ZWD comparisons with GPS-derived results in this section, the model-calculated ZWDs have closer relationships in terms of offset and slope. Based on the model-calculated ZWDs, the WVR-derived ZWDs will be readjusted in next section. In appendix A.7, ZWDs from the WVR, the models and GPS are summarised in tables.

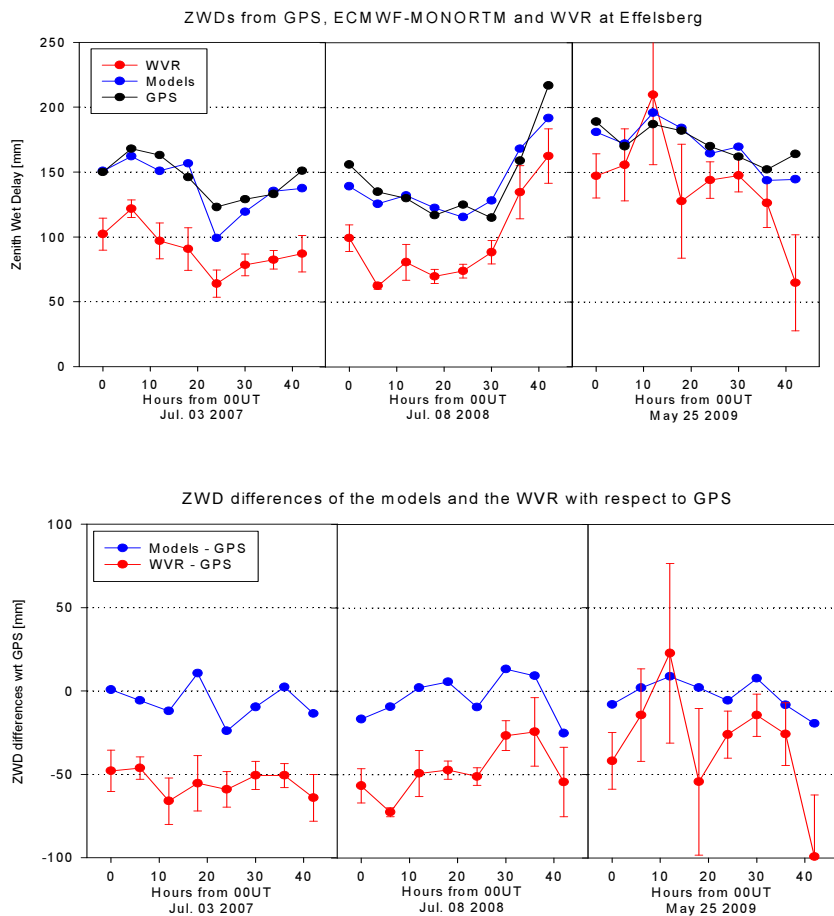


Figure 4-5. Differences between GPS-derived ZWDs and ZWDs from the two approaches

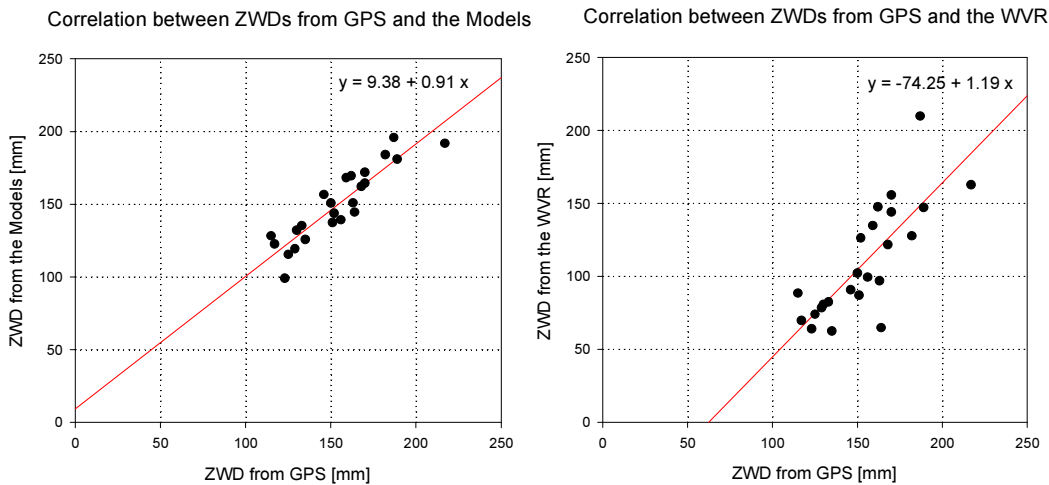


Figure 4-6. Correlation between GPS-derived ZWDs and model-calculated ZWDs (left). Correlation between GPS-derived ZWDs and WVR-observed ZWDs (right)

#### 4.4 Readjustment of ZWDs

In the last section, ZWDs from the WVR-measured and the model-calculated methods were compared with ZWDs from GPS. In the comparison, the model calculations show better agreement to GPS. Although the number of the data used in the comparison was only 24, statistics showed evident differences in terms of mean offset, standard deviation and correlation factors. Furthermore, raw measurements of ZWDs from the WVR show a certain level of noise within a few minutes and some data gaps of a similar length (see black crosses in figure 4-1).

According to these interim findings, ZWDs from the WVR-measured method will be readjusted in two steps. The first step is the computation of running means from the raw measurements of ZWDs by the WVR for data smoothing. The second step is a readjustment of the ZWDs by adding averaged offsets between the WVR-measured and the model-calculated ZWDs. The averaged offsets were calculated for each session and added to the smoothed raw measurement. Finally, the three sets of the ZWDs, the so called the WVR-measured (raw measurements), the smoothed (running mean applied), and the readjusted by the offsets were generated as final results of this chapter.

As discussed in section 3.2.2, the WVR at Effelsberg has the defects of infrequent instrumental calibration accompanying the wet path delay retrieval. Although ZWDs from the models showed better agreement to GPS-derived ZWDs, the models also have defects. The model can only provide ZWDs every six hours while the WVR provide dense observations for the ZWDs. To exploit the advantages of the two approaches, the readjustment approach will be introduced.

For smoothing the noisy raw measurement of ZWDs by WVR, different sampling intervals of observation time were applied with a range between 5 minutes and 30 minutes. Among the sampling intervals, 15 minutes with 7.5 minutes before and 7.5 minutes after the actual epoch showed the most reasonable fit. A 15 minute-interval is a good compromise which takes out the instrument noise but retains the information of the time variability of the atmosphere. The running mean with 15 minutes sampling



interval will be applied in chapter 5.

Figure 4-7 includes reduced ZWDs compared with ZWDs in figure 4-4. Each session has only five data points that are the corresponding periods to 24-hour-long geodetic VLBI sessions. As can be seen in figure 4-7, there are certain offsets between ZWDs from the WVR and the models. Figure 4-8 shows the linear regressions of the two approaches for every single session. As can be seen in the figure, the slopes differences between the two approaches can be considered to be negligible. Thus, offsets in the middle were picked up and summarised in table 4-2 as the mean offsets of each session. These offsets will be applied to the smoothed raw measurements.

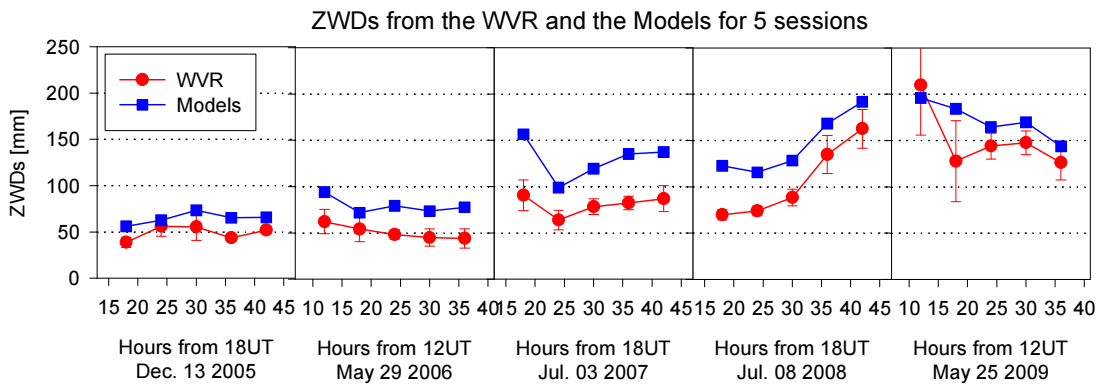


Figure 4-7. ZWDs from the WVR observations and the model calculations

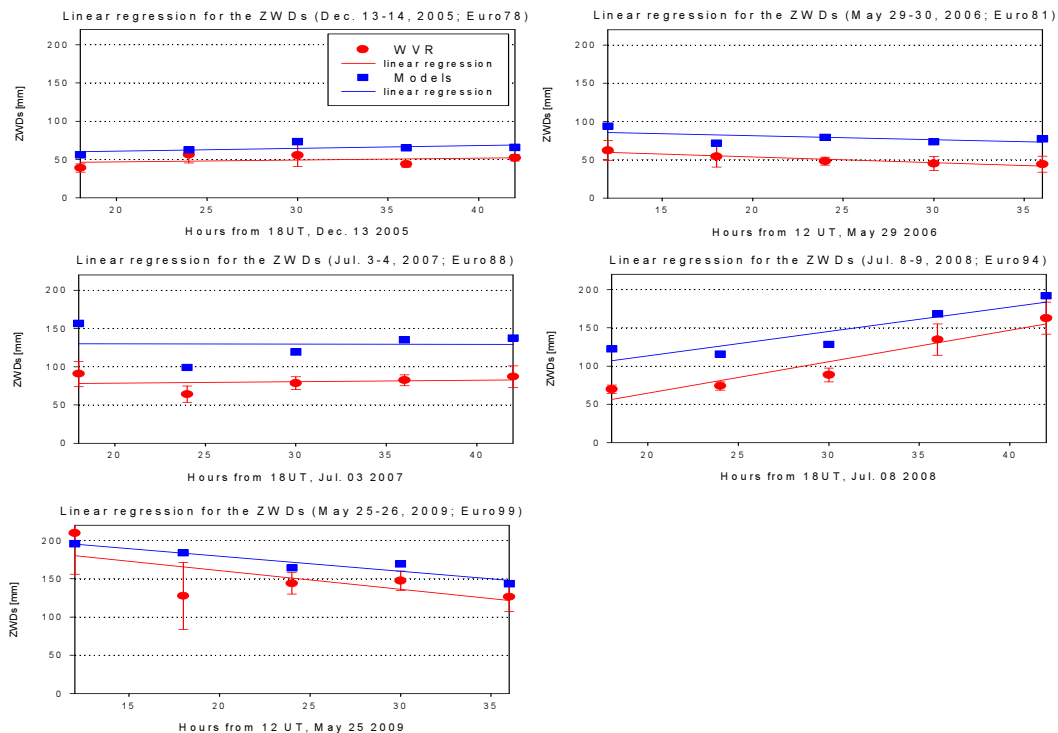


Figure 4-8. Linear regression lines of the two approaches

Table 4-1. Summary of the mean offsets in the readjustments approach

	Euro78	Euro81	Euro88	Euro94	Euro99
Mean offsets [mm]	15.4	28.5	49.1	39.4	20.5

From figure 4-9 to figure 4-13, readjusted ZWDs by the running mean method and the offset are shown together with raw measurements by the WVR. In the figures, red crosses represent the raw measurements and black solid lines represent the smoothed ZWDs with respect to the raw measurements. Blue crosses represent the readjusted one.

In chapter 5, the three sets of ZWDs will be applied for the wet path delay corrections in geodetic VLBI data processing. Hereafter, the first WVR-measured set is called ZWD (WVR<sub>r</sub>), the second WVR-smoothed set is called ZWD (WVR<sub>s</sub>) and the third readjusted by offset is called ZWD (WVR<sub>s+o</sub>).

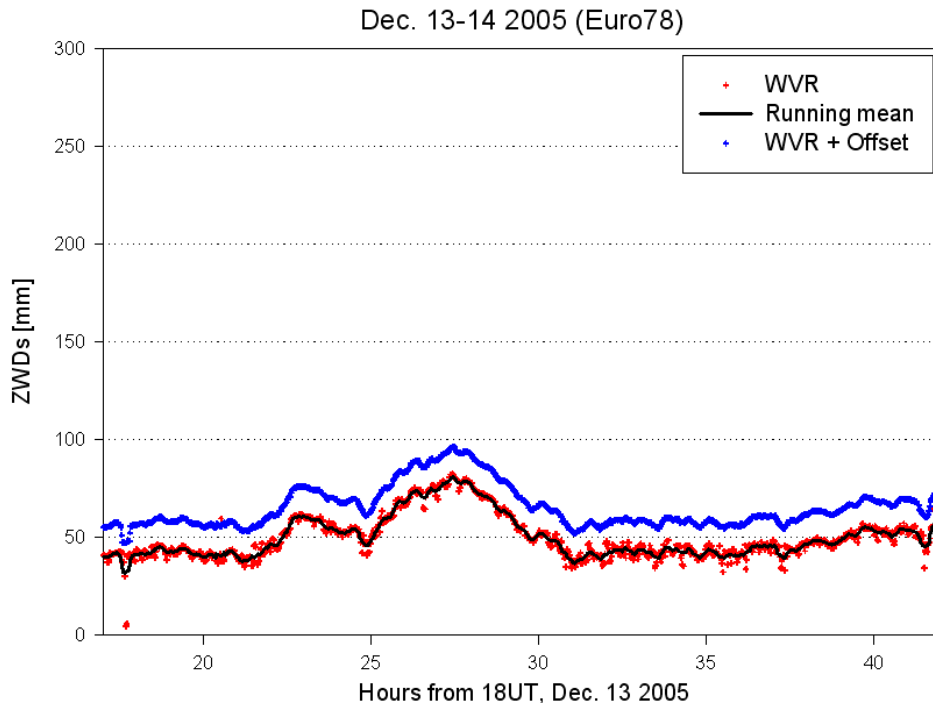


Figure 4-9. ZWDs from the three approaches for the Euro78 session

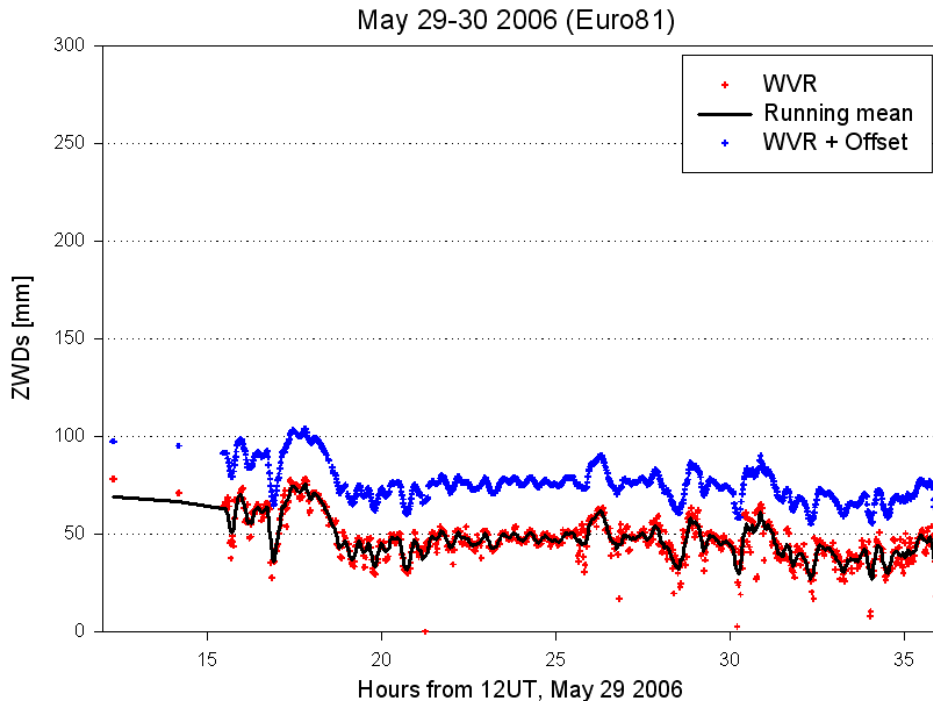


Figure 4-10. ZWDs from the three approaches for the Euro81 session

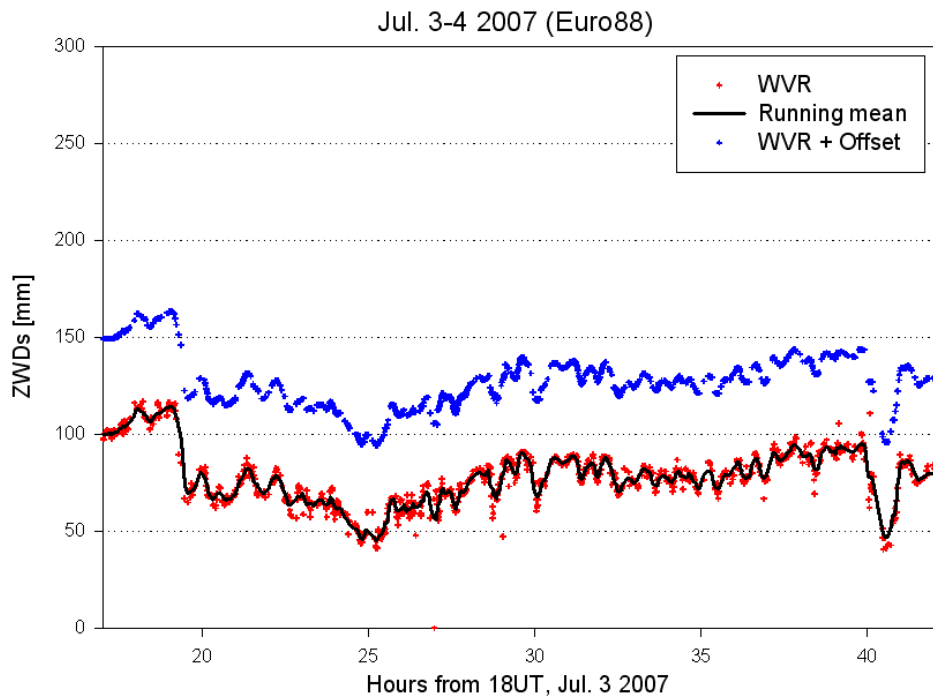


Figure 4-11. ZWDs from the three approaches for the Euro88 session

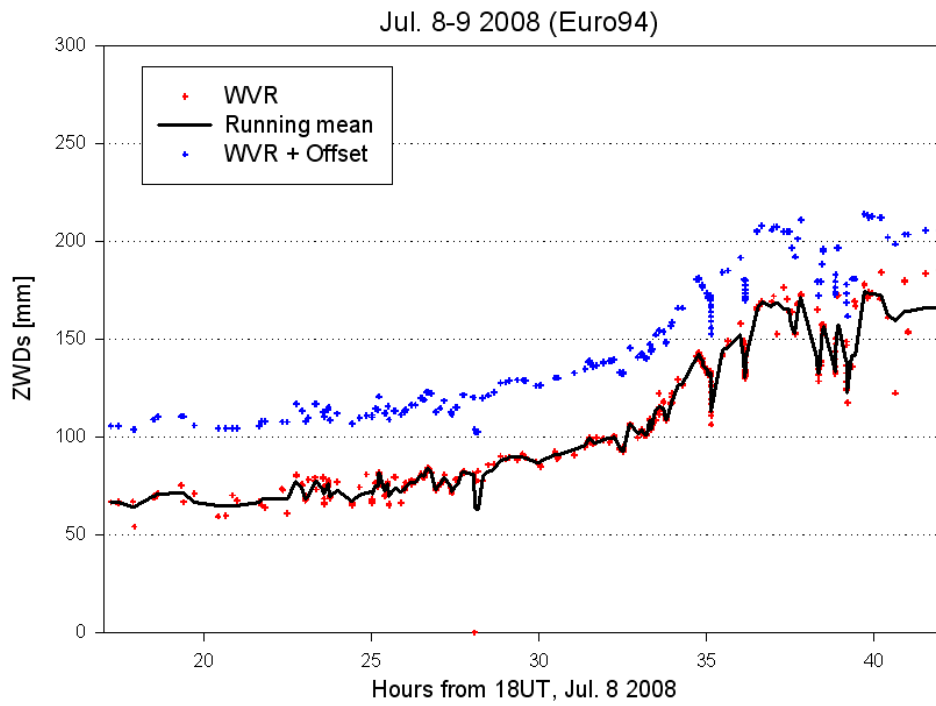


Figure 4-12. ZWDs from the three approaches for the Euro94 session

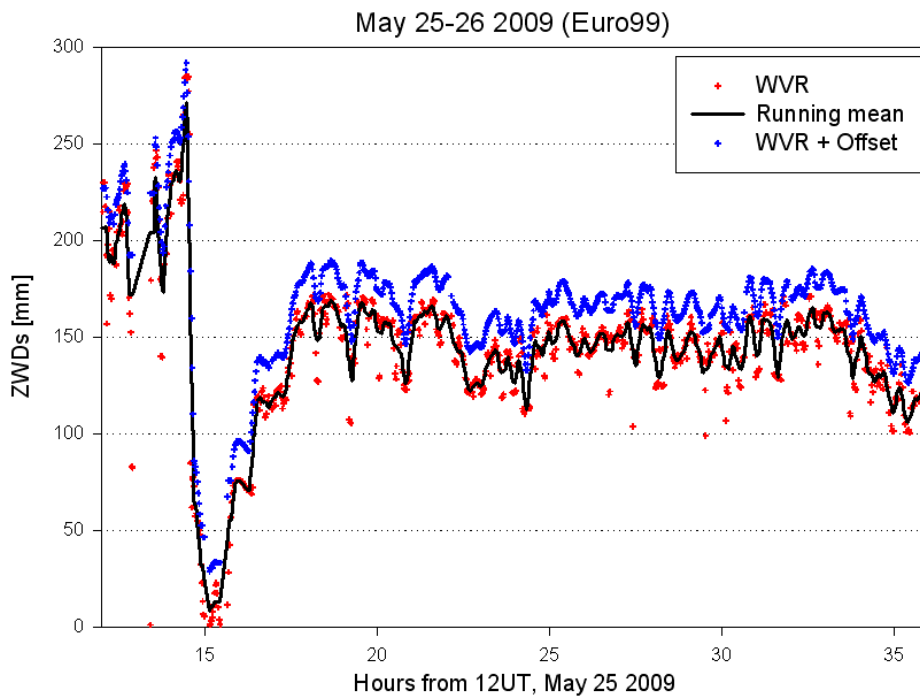


Figure 4-13. ZWDs from the three approaches for the Euro99 session

## 5. ZWDs Application to Geodetic VLBI and its Results

In this chapter, the ZWDs from the three approaches are used for direct corrections of the wet path delays in the five geodetic VLBI sessions. The impacts of the direct corrections were classified in three aspects. The first aspect is the impact on the wet path delay corrections itself. Geodetic VLBI society has been estimating the wet path delay contributions in various approaches. In this study, ZWDs estimated from the observations of five VLBI sessions were analysed. For this, three different sets of a priori calibrations were applied. For the data processing of the five geodetic VLBI sessions, CALC (Ver. 10.01) and SOLVE (release date: 21May 2010) programs were used.

The other two aspects are the impacts on baseline repeatability and height precision. According to Ware *et al.* (1986), wet path delay corrections by WVR can improve baseline length repeatability and height precision by a factor of 3. For various reasons, however, the direct correction based on WVR has not yet been used routinely. One of them is the general instrumental calibration problem.

### 5.1 Impacts on wet path delay corrections in geodetic VLBI

In geodetic VLBI data analysis, it is common that continuous piecewise linear functions (linear splines) with various time resolutions are estimated for the tropospheric zenith delays. Here, we chose to use one hour segments as a compromise of sufficient time resolution and good geometric stability. For the hydrostatic delay corrections, the Niell (1996) mapping function and the Saastamoinen (1972) model for the hydrostatic zenith delay with weather data from the network stations were applied.

The three sets of ZWDs are applied to the Effelsberg observables in the SOLVE program as direct corrections for wet path delays. DBCAL, which is the sub-program of CALC/SOLVE, is used for adding the three sets of ZWDs into the corresponding VLBI databases.

For VLBI processing, the Wettzell position was fixed as the reference station. In addition to the station coordinates, the clock parameters of the other network stations were estimated by SOLVE using quadratic polynomials and a piece-wise linear function. As described in section 1.2.3, atmospheric gradient components were also estimated. Four sets of solutions will be used. Solution A represents SOLVE-estimated atmospheric offsets every hour without introducing WVR corrections (Table 5-1). Solution B and C are the same in applying WVR corrections but they are different in WVR correction type. Solution B introduced WVR corrections as raw measurements that is  $ZWD(WVR_r)$  in the table but solution C introduced WVR corrections in the form of smoothed values, that is  $ZWD(WVR_s)$  in the table. By feature of running mean method described in section 4.4, solution C used the mean value for 15 minutes with 7.5 minutes before and 7.5 minutes after the actual epoch, while solution B used corresponding raw measurements for each epoch. Solution D represents SOLVE-estimated atmospheric offsets every hour by applying an offset between ZWDs from the model calculations and the WVR measurements to the smoothed corrections that is  $ZWD(WVR_{s+o})$  in the table. Each of the WVR corrections were applied by subtracting each type of WVR ZWD corrections during data processing. The corresponding ZWD

estimates by SOLVE for the five sessions are depicted in figure 5-1 to figure 5-10.

Table 5-1. Solution types and descriptions for ZWDs comparisons

Solution type	ZWD corrections	Estimated atmosphere parameters
Solution A; No WVR & Est.	ZWD (SOLVE)	offsets every 60 minutes without WVR corrections
Solution B; WVR & Est.	ZWD (WVR <sub>r</sub> )	offsets every 60 minutes after subtracting raw WVR corrections
Solution C; WVR <sub>rm</sub> & Est.	ZWD (WVR <sub>s</sub> )	offsets every 60 minutes after subtracting the smoothed WVR corrections
Solution D; WVR <sub>rm</sub> +Offset & Est.	ZWD (WVR <sub>s+o</sub> )	offsets every 60 minutes after subtracting the readjusted WVR corrections

The black solid circles are the results of the standard ZWD estimates by SOLVE without any corrections (ZWD(SOLVE), solution A). The red solid circles and blue solid circles are the ZWD estimates after subtracting ZWD(WVR<sub>r</sub>) and ZWD(WVR<sub>s</sub>), respectively (solution B and solution C, respectively). The black hollow circles are the ZWD estimates after subtracting the ZWD(WVR<sub>s+o</sub>) (solution D). If the subtracted ZWDs from one of the three approaches agrees well to the initial ZWD(SOLVE), the resulting ZWD estimates with corrections applied a priori should be located near the zero residual line. See tables 5-2 and 5-3 for detailed statistics of each solution including mean, RMS, and mean offset values from the ZWD(SOLVE) solutions.

As can be seen in figure 5-1, the resulting ZWD estimates of solution B and solution C are located near the zero residual line. Solution B is slightly closer to the zero line than solution C in terms of mean value in table 5-2. It means that ZWD(WVR<sub>r</sub>) have the best agreement with ZWD(SOLVE). The resulting ZWD estimates of solution D are biased towards below the zero line. In order to check the tendency similarities of the three solutions with respect to solution A, the mean offset between the ZWD estimates is subtracted and the RMS are calculated. Table 5-3 summarises the mean offsets and RMS values with figure 5-2 providing a visual impression of the differences. As can be seen in the figure, the three WVR-based approaches show similar properties with solution B having the smallest RMS. From the mean offset from the zero line and RMS, solution B is the best for the Euro78 session.

As mentioned in section 3.2.2, the most recent instrument calibration was conducted one week before the Euro78 session. This winter session was ideal for an absolute calibration with cold sky. In terms of the absolute calibration and the age of calibration interval, ZWD(WVR<sub>r</sub>) for Euro78 shows an advantage of in-situ measurements without contaminations from the effects of the instrument. The internal temperature during the session was rather stable (23.6°C ~ 24.6°C) and close to nominal temperature of 25 °C for this session.

The resulting ZWD estimates and RMS for the Euro81 session are shown in figures 5-3 and 5-4, respectively while the statistics of each solution and the mean offset are listed in tables 5-2 and 5-3, respectively. As can be seen in the figures and the tables, solution B shows the best agreement with solution A in terms of the smallest mean difference while solution D shows the best agreement in terms of the smallest RMS although the RMS values of the other solutions are not significantly larger. Thus, the three solutions can be considered to produce results of the same quality but for all a negative gradient is discernable. As with the Euro78 session, the results of solution D are located below the zero residual line. All three solutions are below the zero line at the beginning of the session. This is probably caused by a lack of ZWD data in the first few hours of the session (Fig. 4-10).

For the Euro81 session, the internal temperature of the WVR was set to 29.1°C at

the very beginning of the session. However, the temperature varied in the range between 25.6°C and 30.5°C during the session. The WVR gain per temperature coefficient is approximately  $-0.7\%$  per °C. In cases where the internal temperature is lower than the set temperature, reduced WVR gain causes lower brightness temperature measurements and also affects the ZWD results if empirical corrections are not applied to the ZWD retrieval as was the case here.

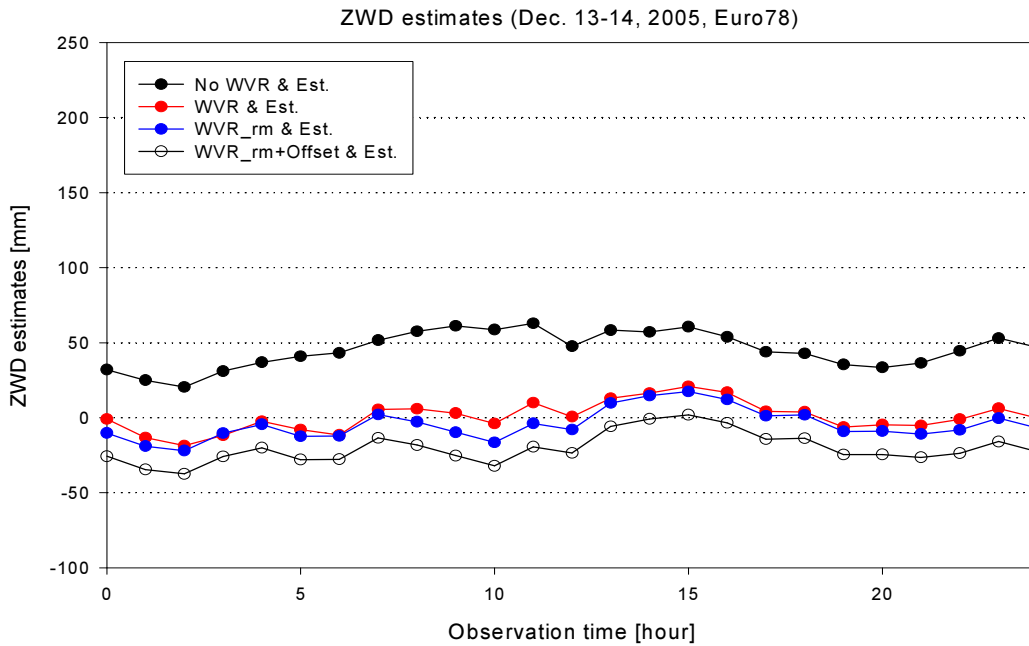


Figure 5-1. ZWD estimates from SOLVE and the three approaches for the Euro78 session

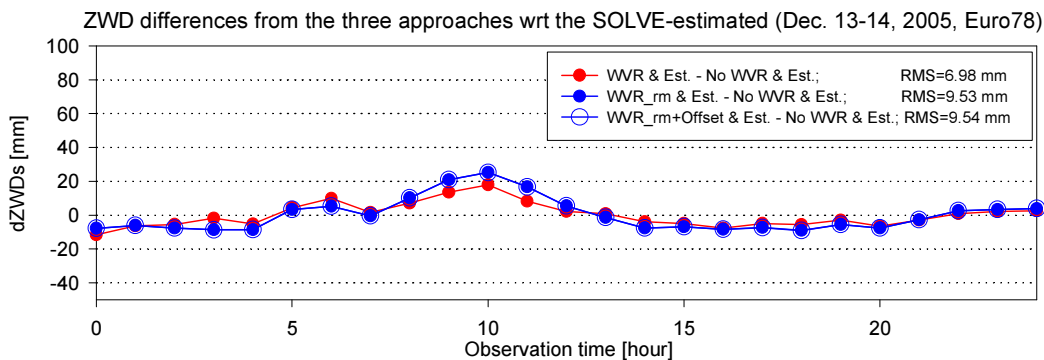


Figure 5-2. Differences of the three approaches with respect to the SOLVE-estimated ZWDs for the Euro78 session

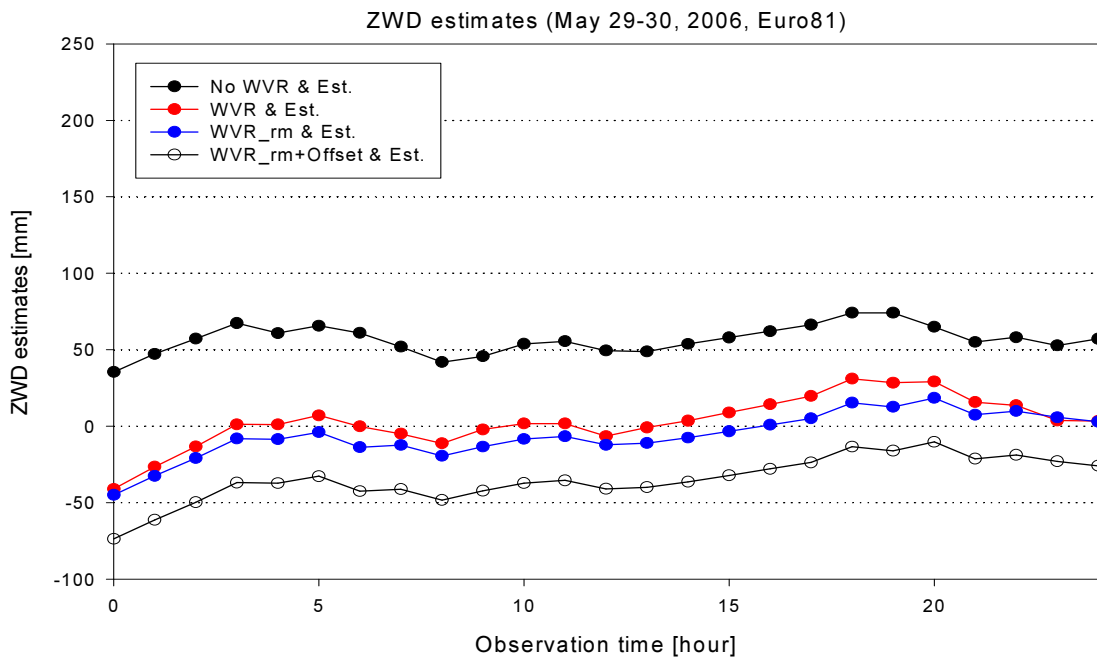


Figure 5-3. ZWD estimates from SOLVE and the three approaches for the Euro81 session

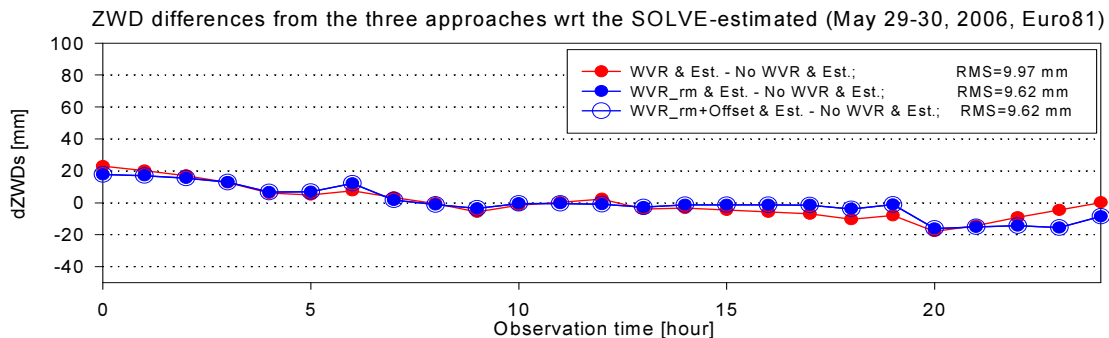


Figure 5-4. Differences of the three approaches with respect to the SOLVE-estimated ZWDs for the Euro81 session

Figures 5-5 and 5-6 show the resulting ZWD estimates and RMS for the Euro88 session. This session was conducted at summer days. An inhomogeneous and humid sky can cause poor absolute calibration, particularly with cold sky load, and this poor calibration is likely to cause offsets. As shown in the figures and in table 5-2, solution D shows the best agreement with solution A in terms of the smallest mean, while solution B shows the best agreement in terms of the smallest RMS. Solution B and solution C are biased over the zero residual line. This tendency is different from the previous two sessions.

As mentioned in section 3.2.2, the last calibration of the WVR was carried out on May 29, 2007. It means that the WVR measurements are performed with one-month-old calibration parameters. The saw-tooth features of brightness temperature are mainly due to malfunction particularly for high frequency channels. Along with the defect of the absolute calibration, old aged calibration parameters also affected the ZWD(WVR<sub>r</sub>) of



solution B. The temperature was set to 37.4°C and the temperature variations during the session were monitored in the range between 28.0°C and 32.8°C. This is considerably deviated from the nominal temperature as compared with the previous session.

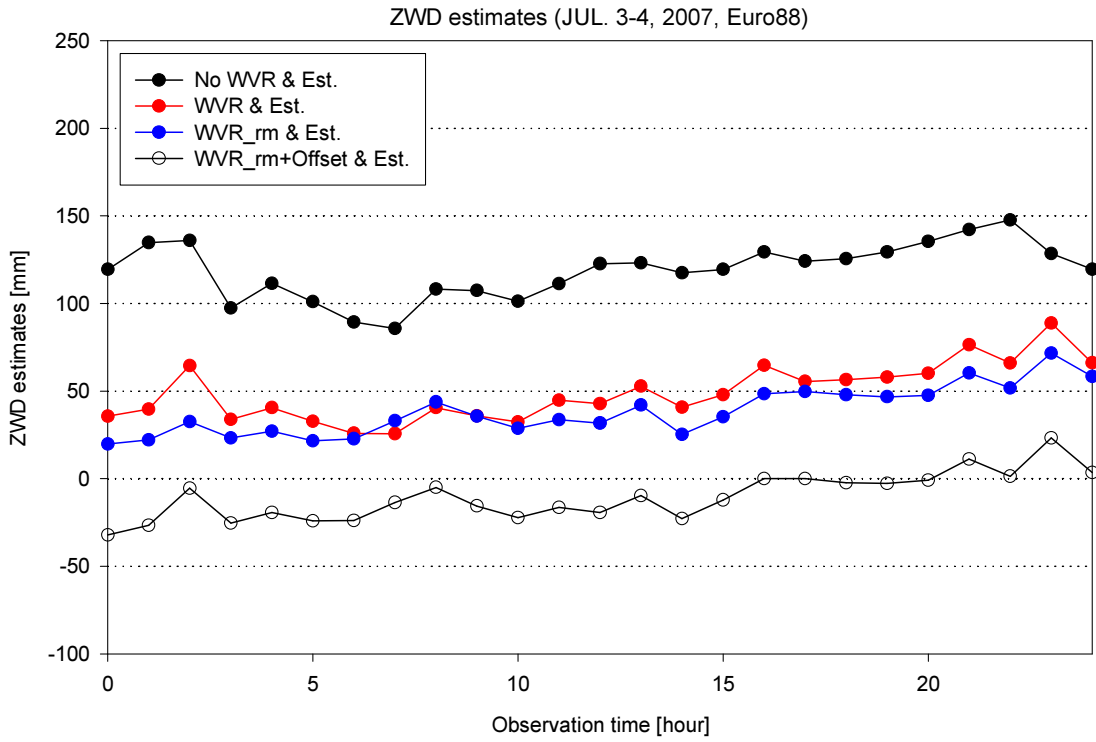


Figure 5-5. ZWD estimates from SOLVE and the three approaches for the Euro88 session

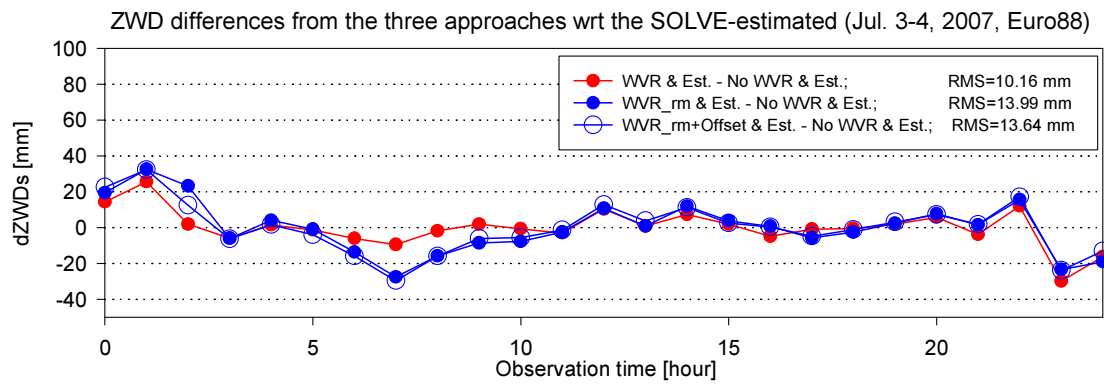


Figure 5-6. Differences of the three approaches with respect to the SOLVE-estimated ZWDs for the Euro88 session

Figures 5-7 and 5-8 show the resulting ZWD estimates and RMS for the Euro94 session. This session was also conducted over summer days. As with the Euro88 session, solution D is the nearest to the zero residual line and the other two solutions are biased over the zero line. As shown in the figures and table 5-2, solution D is the best in terms of the smallest mean offset and smallest RMS.

As mentioned in section 3.2.2, the last calibration of the WVR was carried out on 7 July 2008 including the temperature setting of 29.6°C. The internal temperature variations were in the range between 27.8°C and 30.4°C. The WVR measurements mostly show the best features of the five sessions with one day old calibration parameters. Nevertheless, the ZWD(WVR<sub>r</sub>) of solution B deviated from the initial estimates the most. Recalling the ZWD comparisons with GPS and the models in chapter 4, the Effelsberg WVR underestimates the ZWDs compared to the other two methods. This deviation is probably caused by the bad cold sky load that only works well under cold and clear sky conditions.

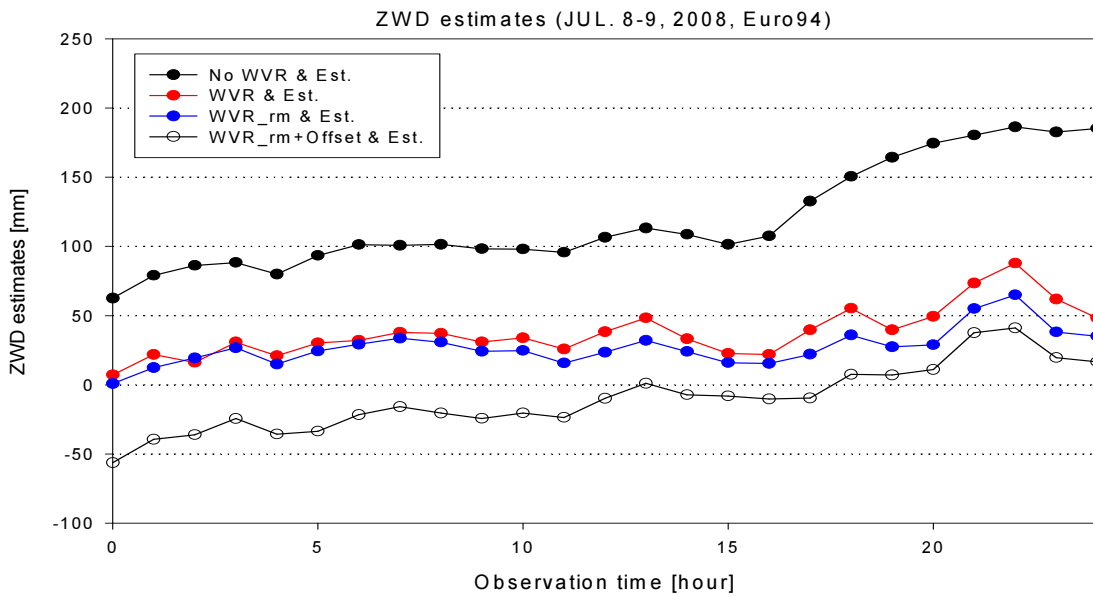


Figure 5-7. ZWD estimates from SOLVE and the three approaches for the Euro94 session

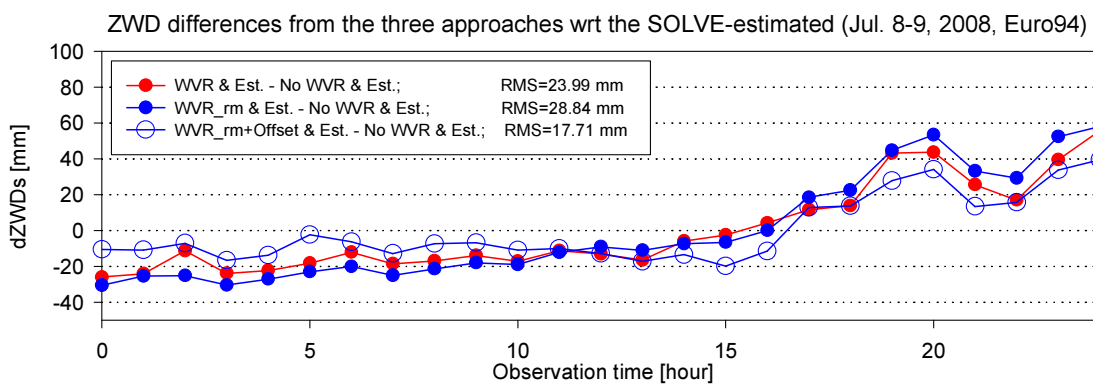


Figure 5-8. Differences of the three approaches with respect to the SOLVE-estimated ZWDs for the Euro94 session

Figures 5-9 and 5-10 show the resulting ZWD estimates and RMS for the Euro99 session. This session was conducted at the end of May. All solutions show a distinct deviation from the general tendency after about 15 hours into the session. As for the

results of the Euro88 and Euro 94 sessions, solution D is generally closest to the zero residual line.

As mentioned in section 3.2.2, the last calibration of the WVR was conducted on 19 February 2009. There was no information on the nominal temperature setting, but the internal temperature variations were recorded in the range between 35.2°C and 44.5°C. As a consequence, a rapid gain drift was also recorded during the session. It was also reported that this gain drift affected the results of the WVR measurements, particularly for the high frequency channels over 23 GHz as shown in figure 3-18 (A. Roy, personal communication, 2010).

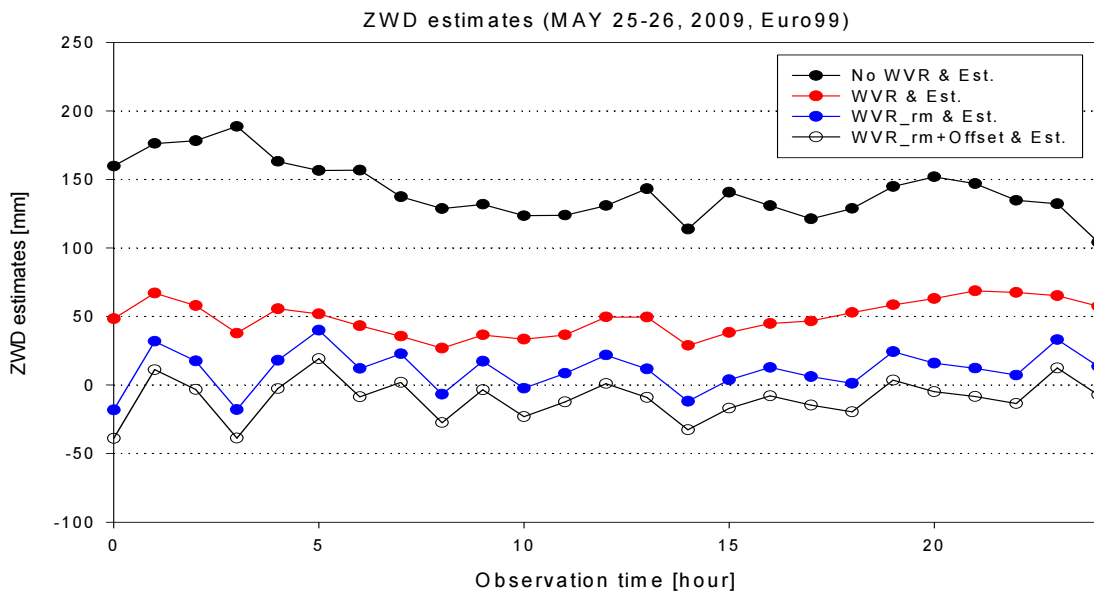


Figure 5-9. ZWD estimates from SOLVE and the three approaches for the Euro99 session

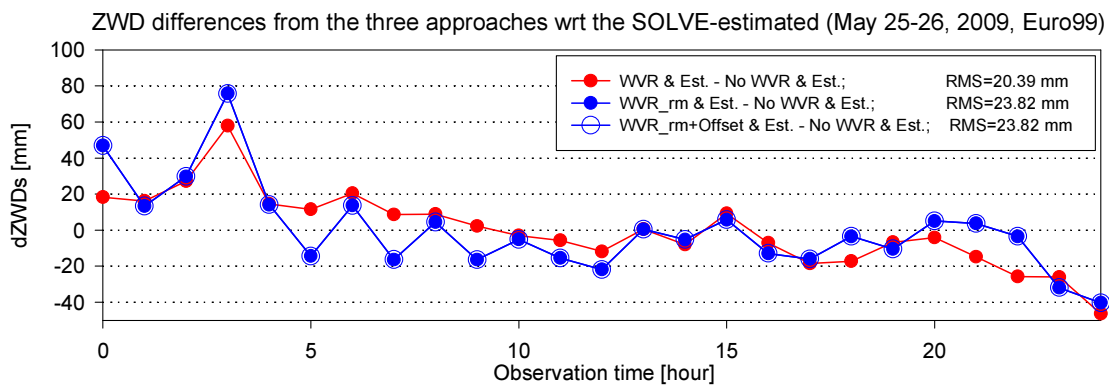


Figure 5-10. Differences of the three approaches with respect to the SOLVE-estimated ZWDs for the Euro99 session

As a summary of the previous results, figure 5-11 depicts the mean and RMS values of each solution. Table 5-2 lists the mean and RMS values after estimation by SOLVE. As can be seen in the figure, all the results of solution D are located below the zero residual line while all those of solution B are located above the zero line. The results of

solution C is always in the middle between the two solutions. Regarding closeness to the zero line, solution B are the best in the first two sessions while solution D are the best in the last three sessions. It seems that this tendency is mainly caused by the absolute calibration using the cold sky load. It can be interpreted in that the first two sessions are under more appropriate sky conditions for the cold sky load than other three sessions. In addition, effects such as out-of-date calibration parameters and internal temperature variations seem to contribute to the abnormal features of solution B in the last three sessions. Nevertheless, solution D has the smallest level of residuals which is an indication of the correctness of this approach, though not to the full extent and apparently overcompensating the effect.

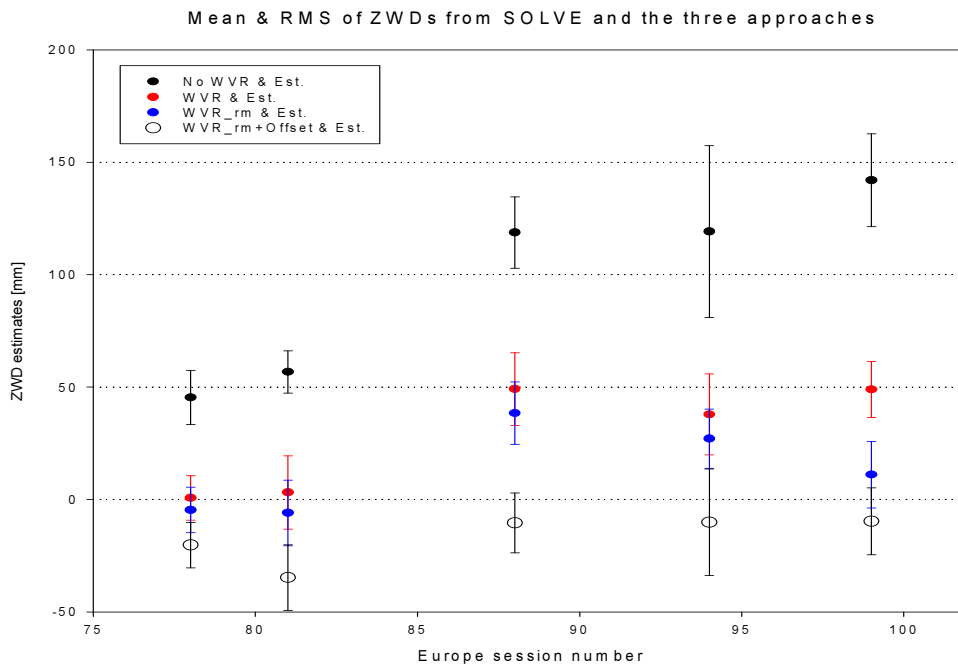


Figure 5-11. Mean and RMS of the ZWD estimates from SOLVE and the three approaches

Table 5-2. Mean and RMS of the ZWD estimates from SOLVE and the three approaches

	(No WVR) <sup>a</sup>		(WVR) <sup>b</sup>		(WVR_rm) <sup>c</sup>		(WVR_rm+Offset) <sup>d</sup>	
	Mean [mm]	RMS [mm]	Mean [mm]	RMS [mm]	Mean [mm]	RMS [mm]	Mean [mm]	RMS [mm]
Euro78	45.4	12.0	0.7	9.9	-4.7	10.1	-20.2	10.1
Euro81	56.7	9.3	3.1	16.3	-6.0	14.6	-34.7	14.6
Euro88	118.7	15.9	49.1	16.2	38.4	13.8	-10.4	13.3
Euro94	119.2	38.2	37.8	18.0	27.1	13.1	-10.2	23.7
Euro99	142.0	20.6	48.9	12.5	11.0	14.8	-9.7	14.8

Table 5-3 summarises the mean offset and RMS with respect to solution A. Along with the offset and RMS, the mean ZWDs retrieved in section 4.4 are summarised. The

mean offsets between each of the three solutions and solution A show systematic tendencies, as already shown in figure 5-11. The RMS values are the numerical representation of the agreement of the individual solutions with solution A after the bias has been removed. The three solutions are of an almost similar level. Differences between the mean offset and mean ZWD can be compared as absolute values. Almost all the differences are in the range between 10 and 20% except for two cases. The two cases are the differences between solution A and solution B for the Euro94 and Euro99 sessions. The mean offsets of these two cases are 30 to 60% smaller than the mean ZWD. Note that the mean ZWD for the two cases agree well within 10% with mean values of solution A in table 5-2. But the resulting offsets are changed. It can be inferred that the mean ZWDs used as direct tropospheric corrections were re-estimated simultaneously with other geodetic parameters by the batch least-square estimation of SOLVE. Therefore, initial mean ZWDs can be different from the mean offsets in table 5-3 after SOLVE estimation. In the next section, in-depth analyses of geodetic parameters, such as baseline repeatability and height, will be conducted.

Table 5-3. Mean offset and RMS of ZWDs with respect to the SOLVE-estimates

	Mean offset & RMS (b – a in table 5-2)		Mean ZWD [mm]	Mean offset & RMS (c – a in table 5-2)		Mean ZWD [mm]	Mean offset & RMS (d – a in table 5-2)		Mean ZWD [mm]
Euro78	-44.7	7.0	50.1	-50.1	9.5	50.1	-65.6	9.5	65.5
Euro81	-53.6	10.0	47.4	-62.7	9.6	47.4	-91.5	9.6	75.9
Euro88	-69.6	10.2	78.0	-80.3	14.0	78.1	-129.1	13.6	127.2
Euro94	-81.4	24.0	107.2	-92.1	28.8	106.8	-129.4	17.7	146.2
Euro99	-93.0	20.4	143.9	-131.0	23.8	144.3	-151.7	23.8	164.8

## 5.2 Impacts on baseline repeatability

### *Fixing baseline evolution parameters*

In this section, the impact of the wet path delay corrections by the three approaches on geodetic parameters such as baseline repeatability and height precision will be investigated. For the investigation on baseline repeatability, it is necessary to determine the baseline evolution beforehand. Note that the five sessions should not be included in the determination process of the baseline evolution; otherwise baselines from the five sessions affect the determined baseline length and baseline rate. Then, it is hard to discriminate the pure impact of the wet path delay corrections by the five sessions from those of the others.

The first criterion for selecting a session is whether Effelsberg participated. According to the criteria, fifteen sessions out of twenty-one IVS Europe sessions were chosen for the determination of the baseline lengths and the baseline rates. Among the participating network stations in the chosen sessions, Onsala and Wettzell stations are simultaneously included with Effelsberg. The only session conducted in 2010 includes Onsala and Effelsberg. This causes a different number of sessions which are used in the

determination of the baseline evolution parameters to 15 sessions for Effelsberg-Onsala and 14 sessions for Effelsberg-Wetzell.

In order to fix the baseline evolution parameters before the baseline repeatability comparisons, atmospheric offset and its rate are estimated once per day for all stations. In order to determine the pure impact of the wet path delay correction using the three ZWD correction approaches in next step, a consistent strategy of data processing applied to all sessions is the most important factor. Among the parameters, the baseline lengths and rates determined by this step will be used for the baseline repeatability investigation in a next step.

The figures below illustrate the baseline evolution for Effelsberg-Wetzell and Effelsberg-Onsala. Figure 5-12 shows the baseline evolution between Effelsberg and Wetzell. The baseline rate determined by this study is  $0.17 \pm 0.302$  mm per year. Figure 5-13 shows the baseline evolution between Effelsberg and Onsala. The baseline rate determined by this study is  $-0.05 \pm 0.321$  mm per year. In appendix A.8, baseline-lengths for the entire sessions of Effelsberg-Wetzell and Effelsberg-Onsala are listed.

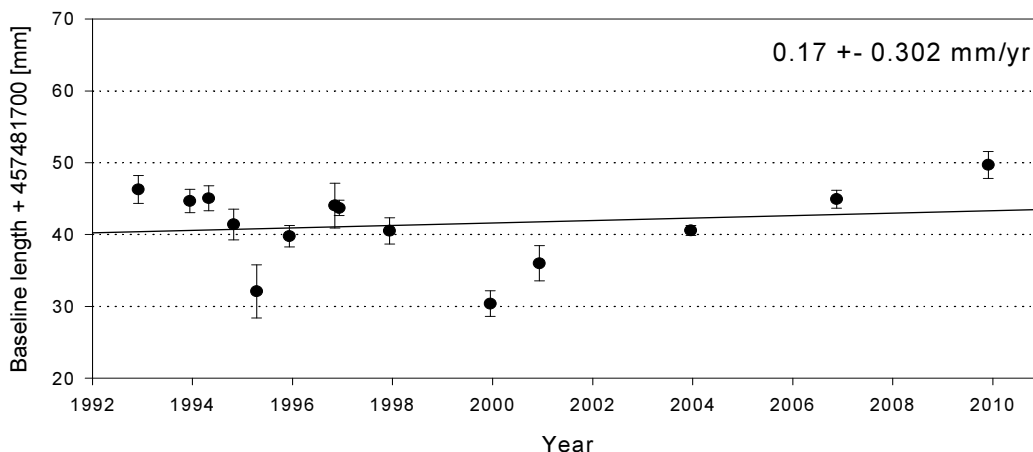


Figure 5-12. Baseline evolution between Effelsberg and Wetzell

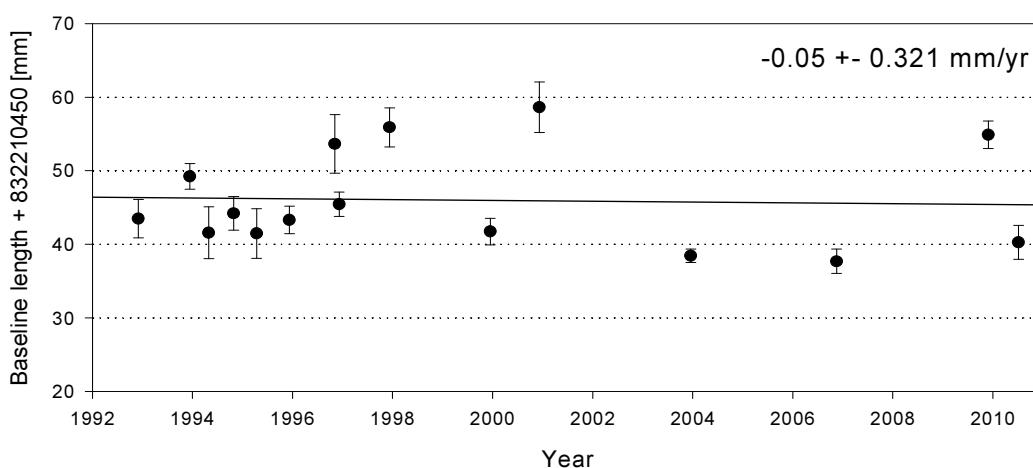


Figure 5-13. Baseline evolution between Effelsberg and Onsala

*Impacts of the four solutions on baseline repeatability*

For the baseline repeatability comparison, SOLVE estimation settings in table 5-1 were changed as summarised in table 5-4. As can be seen in table 5-4, the main change is that the atmospheric offset and its rate are estimated for all stations except Effelsberg in the cases of applying the three WVR ZWD corrections. Compared with the estimation strategy of the fixing baseline rates step, the same estimation strategy is applied. In order to assess the impact of the three corrections on baseline repeatability the atmospheric parameters for Effelsberg should, however, not be estimated. Similarly to the ZWDs comparisons in the previous section, the three sets of ZWDs are applied to the Effelsberg observables in the SOLVE program as direct corrections for wet path delays.

Table 5-4. Solution type and description for baseline repeatability comparisons

Solution type	ZWD corrections	Estimated atmosphere parameters
Solution A <sup>b</sup> : No WVR & Est.		offsets and rate per day without WVR corrections
Solution B <sup>b</sup> : WVR & No Est.	ZWD (WVR <sub>r</sub> )	offsets and rate per day after subtracting raw WVR corrections (not estimated for Effelsberg)
Solution C <sup>b</sup> : WVR <sub>rm</sub> & No Est.	ZWD (WVR <sub>s</sub> )	offsets and rate per day after subtracting the smoothed WVR corrections (not estimated for Effelsberg)
Solution D <sup>b</sup> : WVR <sub>rm</sub> +Offset & No Est.	ZWD (WVR <sub>s+o</sub> )	offsets and rate per day after subtracting the readjusted WVR corrections (not estimated for Effelsberg)

Figure 5-14 shows the variation of the baseline for Effelsberg-Wetzell by the four solutions described in table 5-4. For this baseline repeatability investigation, the baseline length and its rate determined in figure 5-12 are used. The baseline rate was included as a 0.17 mm per year, depicted as a solid black line in the figure, and the five sessions are included. In the solid black circles are the baseline results estimating the tropospheric offset and rate by SOLVE without WVR measurements (Solution A<sup>b</sup>). In solid red circles are the baseline results introducing ZWD (WVR<sub>r</sub>) without estimation of Effelsberg tropospheric parameters (Solution B<sup>b</sup>). In the solid blue circles are the baseline results introducing ZWD (WVR<sub>s</sub>) without estimation of Effelsberg tropospheric parameters (solution C<sup>b</sup>). In the hollow black circles are the baseline results introducing ZWD (WVR<sub>s+o</sub>) without estimation of Effelsberg tropospheric parameters (solution D<sup>b</sup>). RMS and weighted RMS (WRMS) values are calculated with respect to the solid black line. The RMS is listed to provide information on possible outliers. In appendix A.8, baseline-lengths for the five sessions of Effelsberg-Wetzell and Effelsberg-Onsala are listed.

As can be seen in the figure, solution D<sup>b</sup> shows the best result in terms of RMS, although significant improvement was not found in comparison with the RMS of solution A<sup>b</sup>. Solution A<sup>b</sup> shows the smallest WRMS. In general, solution D<sup>b</sup> has the shortest baselines among the four solutions except for the last session. As a conclusion for the Effelsberg-Wetzell baseline, there are no systematic effects on the baseline repeatability by the three ZWD corrections. Considering that the position of Wetzell was fixed as a reference for SOLVE processing, differences between the solutions are

purely the impacts of the three ZWD correction approaches. The differences are in the approximate range of 5 to 10 mm.

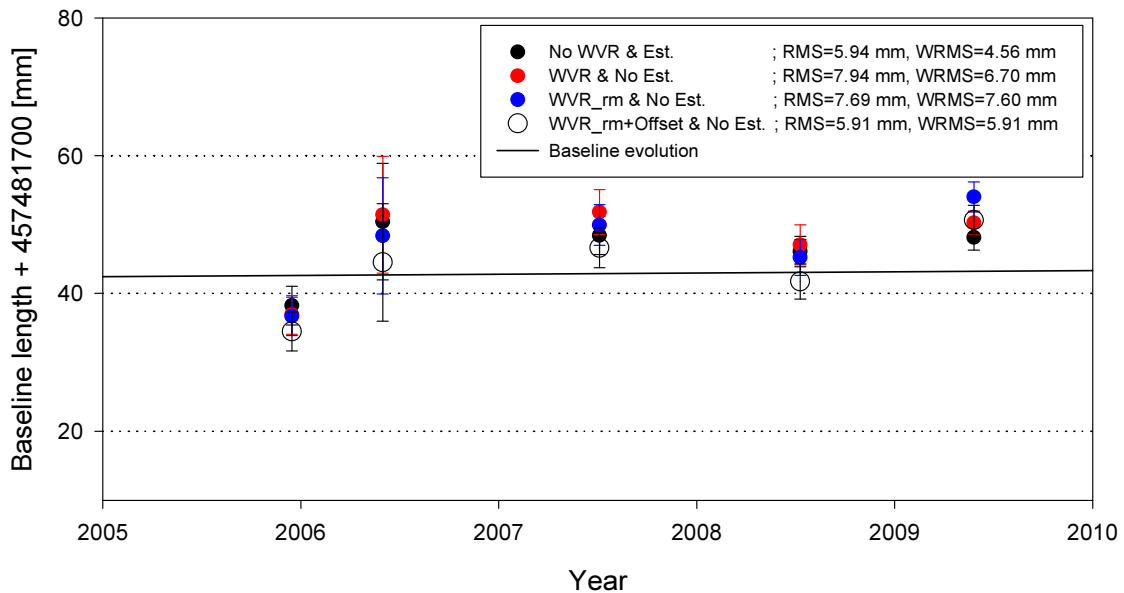


Figure 5-14. Variation in baseline between Effelsberg and Wettzell

Figure 5-15 shows the variation of the baseline for Effelsberg-Onsala for the four solutions. For this baseline repeatability investigation, the baseline and its rate as determined in figure 5-13 are used. The baseline rate used was  $-0.05$  mm per year, depicted by a solid black line in the figure, and the five sessions are included. As can be seen in the figure, solution A<sup>b</sup> shows the best agreement in terms of RMS and WRMS. As for the Effelsberg-Wettzell baseline, solution D<sup>b</sup> always has the shortest baseline lengths among the four solutions. But the other two ZWD corrections from the WVR-measured and the WVR-smoothed are located above and below with respect to solution A<sup>b</sup>. In conclusion for the Effelsberg-Onsala baseline, there are no systematic effects on the baseline repeatability by the three ZWD corrections. However, the WRMS differences between the solutions are in the range of 10 and 20 mm which is quite large. A probable reason for the large scatter is the difference in the number of observations. In general, the number of VLBI delay observations for the Effelsberg-Onsala baseline was smaller than for the Effelsberg-Wettzell baseline during each of the five sessions in the range of about -10 and -50%.

From the results of baseline repeatabilities, no conclusion can be drawn for the superiority of one of the three ZWD correction approaches. The RMS and WRMS values are no reliable indicators for a robust assessment of the approach because of the poor statistics from only a sampling number of five. While the baseline Wettzell-Effelsberg produced some promising results, the baseline Onsala-Effelsberg contradicted this impression.

In the next section, the impact of the three ZWD corrections on height will be treated as an extended analysis of the vertical component variation.



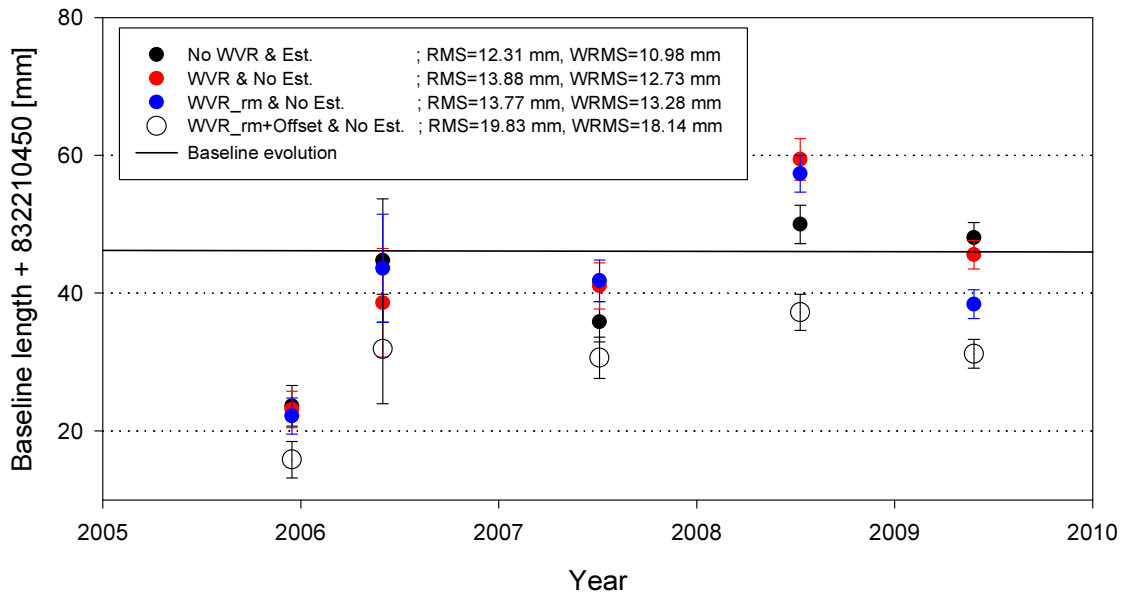


Figure 5-15. Variation in baseline between Effelsberg and Onsala

### 5.3 Impacts on height precision

As in the last analysis on the impact of the wet path delay corrections by the three approaches on geodetic parameters, the investigation in this section focuses on the precision of the height component. According to Ware *et al.* (1986), wet path delay correction by WVR can improve height precision as well as baseline repeatability. In order to check the impact on height precision, the variability of the topocentric station coordinate component is investigated with respect to the a priori coordinate. From the geophysical information, it can be deduced that Effelsberg is vertically stable within  $\pm 1\sim 2$  mm/year.

Figure 5-16 shows the change of the height component and its standard deviations for Effelsberg. The black bars illustrate the height components of solution A<sup>b</sup> for the five sessions. Red bars, green bars, and yellow bars represent the same components for solution B<sup>b</sup>, solution C<sup>b</sup>, and solution D<sup>b</sup>, respectively. The black dashed line is a mean height determined in the same way as in the previous section. Again the height components for the five sessions were excluded in order to differentiate the pure effects of the three ZWD correction approaches from the other sessions. As a result, the mean height above a reference height is determined as 43 mm. The sessions used in the mean height determination are listed in table A.9-1 in the appendix.

As can be seen in the figure, the first three solutions are above the reference height except of the height of solution B<sup>b</sup> in the last session. The results of solution D<sup>b</sup> are always below the zero line. The RMS and WRMS values agree rather well except of solution A<sup>b</sup> where the result of the Euro81 session causes the RMS to be slightly higher than the WRMS indicating a tendency of the session of being further away from the mean. However, this is compensated for by forming the WRMS.

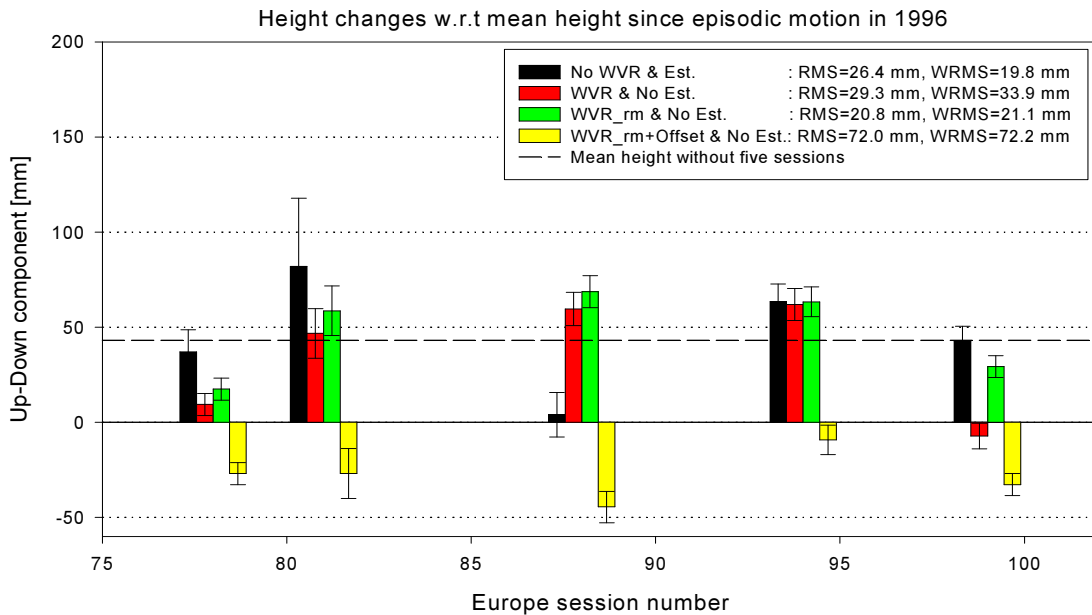


Figure 5-16. Change in height components by the four solutions with respect to mean height since the episodic motion

As summarised in table A.9-2 in appendix A.9, the standard deviations of Solution A<sup>b</sup> are always larger than those of the other three solutions with the second session being exceptionally large with about a factor of three larger than the other sessions. This indicates that the general solution setup or the observations themselves have a deficit. Within the other three solutions, the number of unknown parameters is reduced by the number of atmosphere parameters of Effelsberg. Although one would expect an increase in the standard deviations of the Effelsberg height component due to the reduced number of degrees of freedom, the opposite effect appears. This can only be caused by a reduction of the sum of the weighted residuals squared. A possible reason for this can only be the use of direct WVR measurements instead of estimations by SOLVE. While Solution A<sup>b</sup> was determined without WVR measurements, the other three solutions were determined with direct WVR measurements. In the SOLVE least squares adjustment, the application of WVR measurements seems to affect the determination of the height component in a positive way.

Another approach is to determine the height scatter with respect to the mean height of only the five sessions (Fig. 5-17). In contrast to the long-term mean in figure 5-16, this figure represents the short-term mean for each solution type. Each short-term mean is depicted by solution with the same coloured solid line. These mean values are significantly different levels with solution D<sup>b</sup> being off from the others by 60~70 mm (see table A.9-2 in the appendix). The relative behaviour of the RMS and WRMS is the same as for the long term mean because the original data is the same. Only the means are computed differently and, thus, the WRMSs are much reduced for solution D<sup>b</sup>.

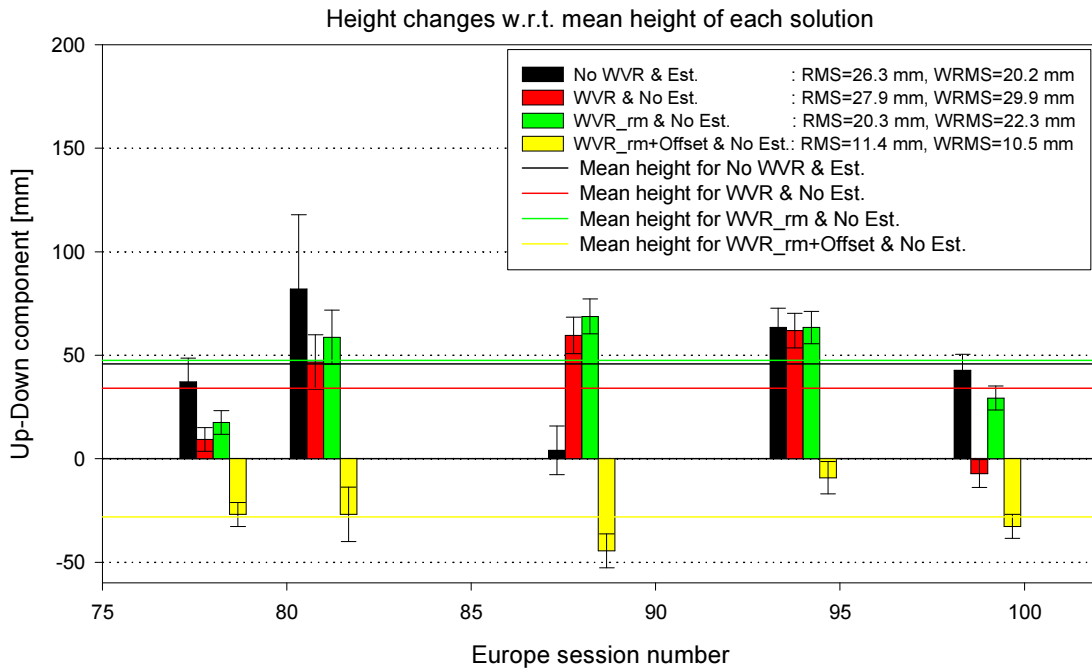


Figure 5-17. Change in height components by the four solutions with respect to mean height of each solution

As shown in the above figure, the ZWD corrections from the three approaches affected the height repeatability for the five sessions. Solution B<sup>b</sup> and Solution C<sup>b</sup> were in agreement within a few millimetres except for the last session. As described in section 4.4, ZWD(WVR<sub>r</sub>) and ZWD(WVR<sub>s</sub>) applied in Solution B<sup>b</sup> and Solution C<sup>b</sup>, respectively, were not significantly different. Thus, the good agreement between the two solutions has been expected. However, solution D<sup>b</sup> showed a negative bias in the range of 60 mm to 70 mm with respect to the other solutions, particularly solution C<sup>b</sup>. Even if one considers the offset corrections for ZWD(WVR<sub>s+o</sub>) in the range of 15 to 50 mm as shown in table 4-1, this bias is a significantly large quantity.

In order to find a reason for this bias, particularly between solution C<sup>b</sup> and solution D<sup>b</sup>, arbitrary offsets, which are 1, 5, and 10 mm, were added to ZWD(WVR<sub>s</sub>) for the Euro78 session. Then the height changes were compared with each other. From the comparisons, the height change corresponds to -2.9 mm per 1 mm of ZWD(WVR<sub>s</sub>) offset. It means that the resulting height changes are almost three times bigger than the ZWD variations. The expected relationship is  $\Delta H \approx -2 * \Delta ZD$  (Boehm, pers. comm.). Although the ratio found here is significantly larger, it can be stated that it is not too far away from the expectation taking into account that the number of sessions is rather small.

In order to investigate the reasons for this, we also checked other estimated parameters such as clock offsets and atmospheric gradients. While there were no significant changes in atmospheric gradients between the results, significant changes in clock offset estimates were found. The clock offsets changes were negative when compared with one of those of solution C<sup>b</sup> and were well matched with the resulting height changes. Nothnagel *et al.* (2002) pointed out the high correlation between clock offset and the tropospheric vertical component estimated in VLBI least squares adjustments. They showed that clock errors can be mapped onto the vertical component.

From the test computations and the previous study, it seems that the biases between solution  $C^b$  and solution  $D^b$  are mainly caused by internal effects in the least squares adjustment. One feature of the least squares adjustment is that estimated parameters are affected by the other parameters through their correlations. Considering the high correlation between the clock offset and the vertical component, the larger-than-expected bias in solution  $D^b$  can most probably be attributed to internal estimation effects.

## 6. Summary and Discussion

In order to correct the wet path delays in geodetic VLBI, line-of-sight measurements from a WVR and theoretical calculations from models were used in this study. The multi-channel WVR at Effelsberg determines these wet path delay corrections. At the same time, ECMWF provides meteorological profiles instead of radiosonde observations over Effelsberg. The radiative transfer model MonoRTM uses the profiles for theoretical calculations based on radiative transfer equations and the accompanying absorption model.

From comparisons of ZWDs from GPS analyses and different wet delay retrieval processes, a solid foundation for offset corrections of the WVR measurements was found based on the model calculations. Along with the offset corrections, the noisy tendency of ZWDs from the WVR was smoothed by computing running means. In this study, readjustment means a combination of the offset correction and the smoothing that are called  $ZWD(WVR_{s+o})$  and  $ZWD(WVR_s)$ , respectively. Together with raw measurements by the WVR ( $ZWD(WVR_r)$ ), these three sets of ZWDs were applied as wet path delay corrections to the geodetic VLBI observations and the impacts on the results were investigated in terms of baseline repeatability and height precision.

With respect to the results, several factors were determined. The baseline repeatability was slightly improved considering the RMS when ZWD corrections from  $ZWD(WVR_{s+o})$  are introduced for the Effelsberg-Wetzell baseline, but there was no improvement of the baseline repeatability for the Effelsberg-Onsala baseline. The height precision was improved by a factor of 2 in terms of WRMS with respect to the short-term mean heights when  $ZWD(WVR_{s+o})$  are introduced. However, there are significant differences in the mean heights between the different solutions which cannot be explained by the normal ratio of  $\Delta H$  vs.  $\Delta ZD$  alone. A possible reason is that the parameters estimated in the least squares adjustment are easily affected by the other parameters through high correlation coefficients, particularly between the clock offset, the tropospheric parameters and the vertical coordinate component.

Even though improvements for certain cases were found, it is difficult to make a solid judgement only based on the poor statistics of the small number of sessions. As mentioned at the start of this thesis, it was expected that several geodetic VLBI sessions with useful WVR measurements at Effelsberg would eventually be available when this study was embarked on. However, in the course of time it turned out that only five sessions could be successfully observed. For this reason the conclusions will have to be based on these five sessions alone. It is obvious that more sessions need to be used for the foundation of a more concrete judgment in the future.

For better comparison between wet path delay corrections, the delays in zenith direction were used. For the ZWD conversion, the Niell mapping function was used for the Effelsberg WVR and SOLVE. Although this conversion was inevitably necessary in this study, the advantage of the line-of-sight measurements of the Effelsberg WVR was faded out.

Regarding absolute and periodic instrument calibrations, an improved WVR is in the lab in an advanced state of construction. It will have an internal waveguide load that can be switched on under software control so that it can automatically perform daily calibrations. Concerning the internal temperature variation, it also has improved

temperature stabilisation which should reduce the calibration drift due to the temperature-dependent gain changes (A. Roy, personal communication, 2011). Along with the instrument implementations, higher resolution profiles from an advanced NWM would also be favourable for use in further studies.

Finally, the smoothing method needs to be improved. In this study, the running mean method was used for smoothing ZWD measurements by the WVR. For the running mean, fifteen minutes was selected as a sampling interval. Considering the number of VLBI observations used in SOLVE, this sampling interval includes 1~3 scans. For a perfect ZWD correction, averaging by every scan is preferred in the future. In addition, the effects of observables at low elevations under 7~8 degrees on the baseline and height repeatabilities should be checked. According to MacMillan and Ma (1994), observations at very low elevations may degrade baseline repeatabilities.

## 7. Conclusions

This study includes the first attempt to use NWM and RT models together with a WVR instrument for the wet path delay correction of geodetic VLBI. From the results of this study, several conclusions are made despite the weak statistical foundation.

- ZWD retrieval: ZWDs from MonoRTM (ECMWF) were closer to GPS-derived ZWDs than those from WVR measurements.
- Usefulness of the model approach: Since the WVR at Effelsberg suffered from infrequent instrumental calibration, the combination approach of NWP and RT models is useful for the readjustment of ZWD measurements from the WVR.
- Baseline repeatability: Considering the RMS, solution  $D^b$  using ZWD(WVR<sub>s+0</sub>) shows a slightly better agreement with respect to the baseline evolution line for the Effelsberg-Wetzell baseline. Nevertheless, improvement in baseline repeatability is not clear due to the small number of sampling sessions.
- Height precision: WRMS of solution  $D^b$  using ZWD(WVR<sub>s+0</sub>) shows an improvement by a factor of 2 with respect to the short-term mean height but there is a 60~70 mm bias between the short-term mean from solution  $D^b$  and from the other solutions.

This study has shown a possible improvement for wet path delay corrections in geodetic VLBI by the use of the WVR at Effelsberg, although the promising advantages of the instrument were faded out by insufficient absolute calibrations and adverse instrumental effects. The conclusion of this study is that the WVR observations are not perfectly suitable for wet path delay corrections yet, mainly because it has certain shortcomings with respect to instrument calibrations. It is expected that more accurate wet path delay corrections from the Effelsberg WVR will become available when the implementations for instrument calibration on the WVR are completed. On the other hand, the approach with the models used in this study could also be applied for WVR sites that have no periodic radiosonde observations. Considering the global applicability of ECMWF and RT models, the possibility of implementing the model approach for other geodetic VLBI stations is high.

# Appendix

## A.1 ECMWF profiles

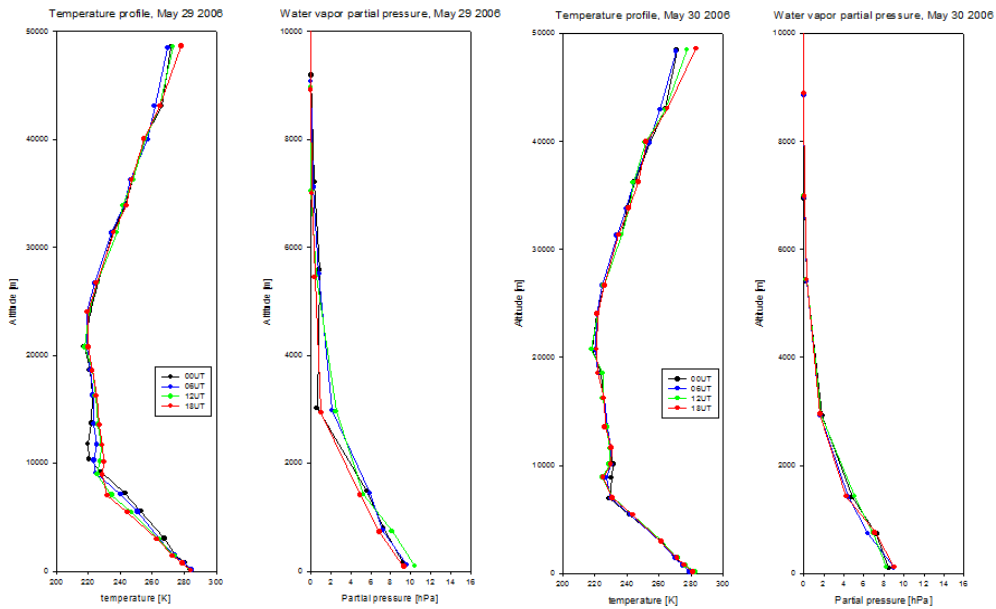


Figure A.1-1. ECMWF profiles for temperatures and water vapour partial pressures over Effelsberg (29-30 May 2006)

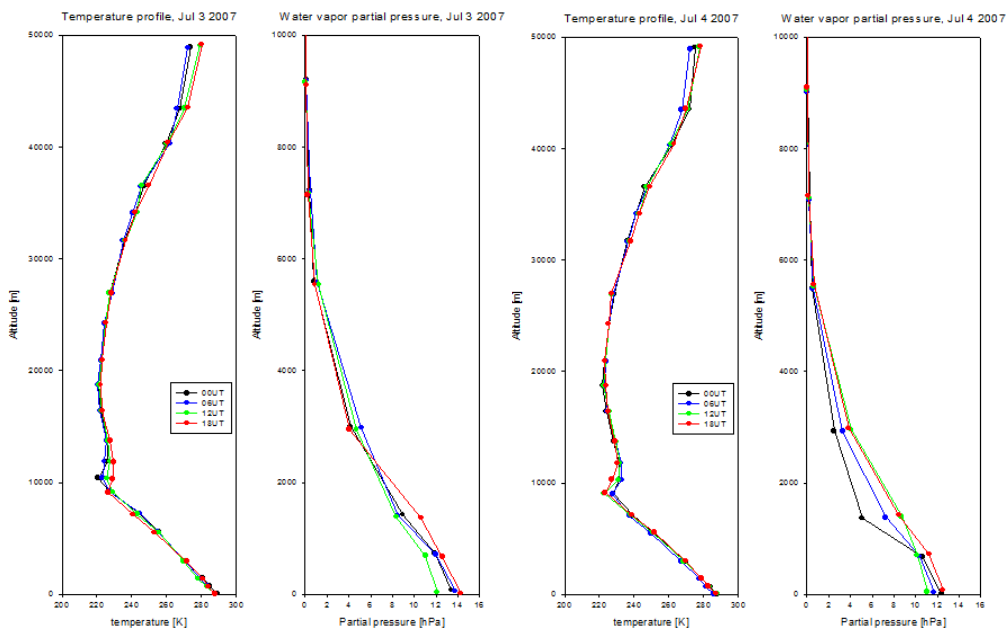


Figure A.1-2. ECMWF profiles for temperatures and water vapour partial pressures over Effelsberg (3-4 Jul. 2007)



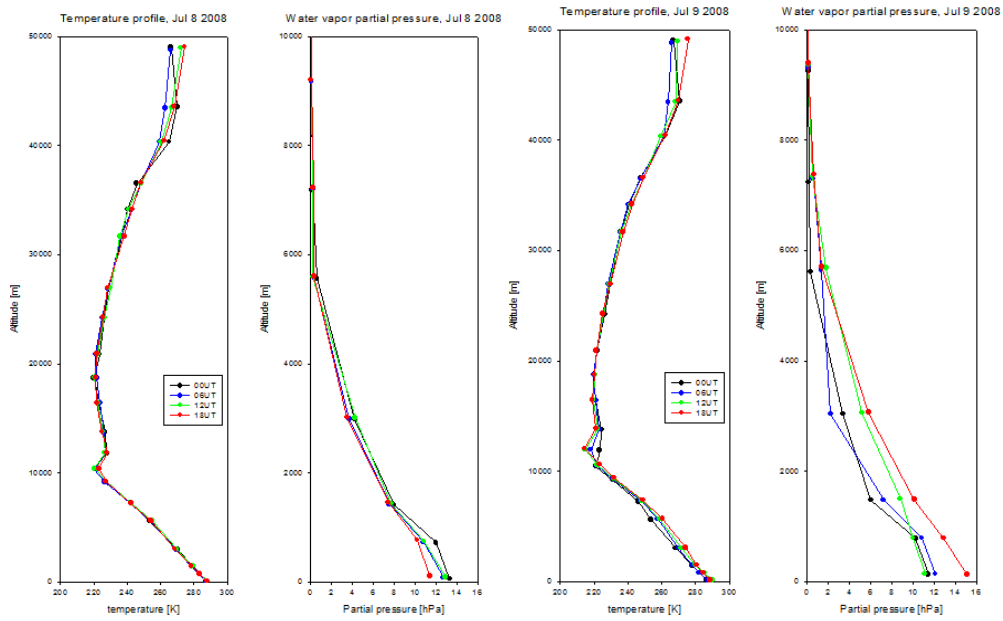


Figure A.1-3. ECMWF profiles for temperatures and water vapour partial pressures over Effelsberg (8-9 Jul. 2008)

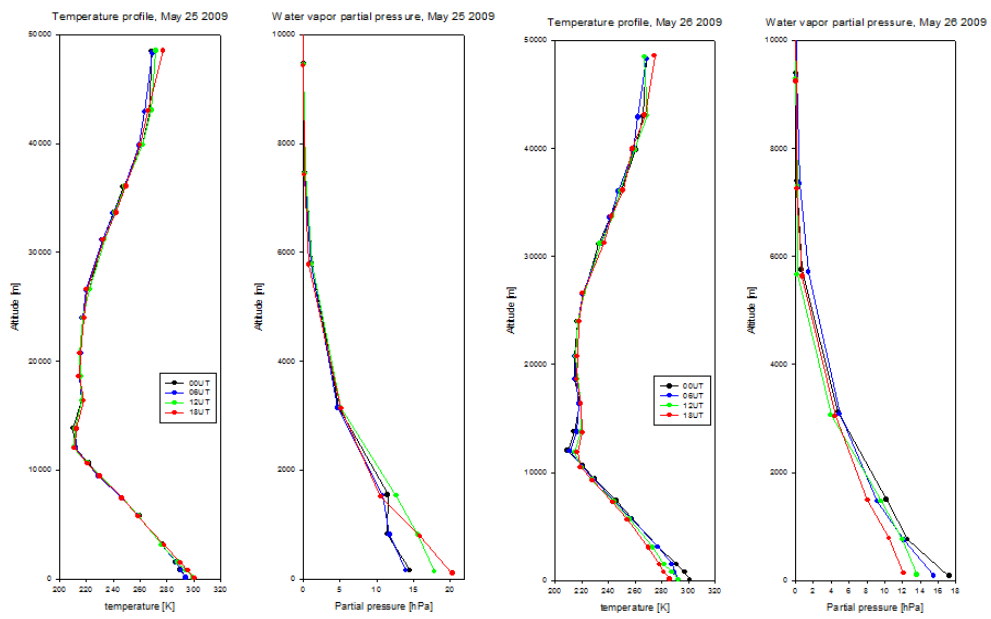


Figure A.1-4. ECMWF profiles for temperatures and water vapour partial pressures over Effelsberg (25-26 May 2009)

## A.2 MonoRTM

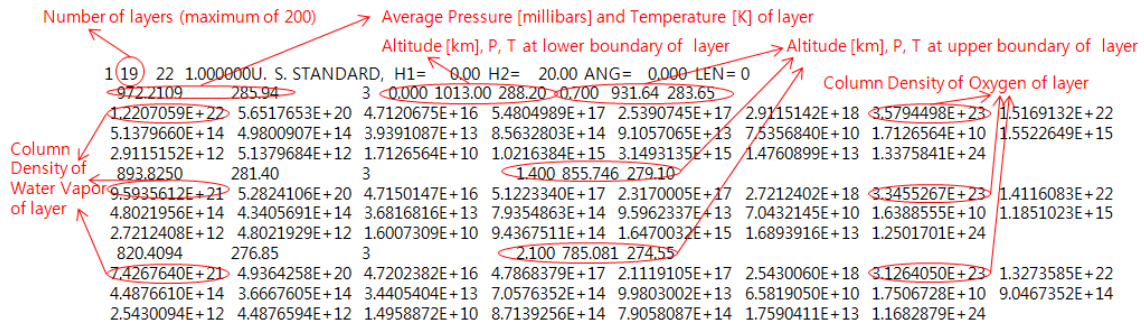


Figure A.2-1. The format of the meteorological profile for MonoRTM (Example)

Table A.2-1. Summary of integrated column density from the surface to the top of the layers

Session points	Integrated Column Density [ $10^{22}$ molecules/cm <sup>2</sup> ]
00 UT, Dec. 13, 2005	1.80179
06 UT, Dec. 13, 2005	2.46476
12 UT, Dec. 13, 2005	3.25791
18 UT, Dec. 13, 2005	2.87984
00 UT, Dec. 14, 2005	3.22064
06 UT, Dec. 14, 2005	3.72711
12 UT, Dec. 14, 2005	3.32704
18 UT, Dec. 14, 2005	3.38929
00 UT, May 29, 2006	4.36343
06 UT, May 29, 2006	5.05752
12 UT, May 29, 2006	4.92464
18 UT, May 29, 2006	3.70976
00 UT, May 30, 2006	4.08882
06 UT, May 30, 2006	3.77673
12 UT, May 30, 2006	4.01685
18 UT, May 30, 2006	3.84048
00 UT, Jul. 03, 2007	7.93224
06 UT, Jul. 03, 2007	8.51122
12 UT, Jul. 03, 2007	7.96562
18 UT, Jul. 03, 2007	8.24722
00 UT, Jul. 04, 2007	5.17235
06 UT, Jul. 04, 2007	6.23753
12 UT, Jul. 04, 2007	7.15665
18 UT, Jul. 04, 2007	7.23522
00 UT, Jul. 08, 2008	7.33081
06 UT, Jul. 08, 2008	6.62839
12 UT, Jul. 08, 2008	6.98011
18 UT, Jul. 08, 2008	6.48380
00 UT, Jul. 09, 2008	6.04097
06 UT, Jul. 09, 2008	6.75736
12 UT, Jul. 09, 2008	8.92431
18 UT, Jul. 09, 2008	10.11256
00 UT, May 25, 2009	9.52854
06 UT, May 25, 2009	9.08346
12 UT, May 25, 2009	10.74278
18 UT, May 25, 2009	9.81921
00 UT, May 26, 2009	8.71266
06 UT, May 26, 2009	9.03431
12 UT, May 26, 2009	7.71857
18 UT, May 26, 2009	7.60739

### A.3 Optical depth by MonoRTM(ECMWF)

Black solid lines represent the U.S. standard model and blue solid lines are spectra when ECMWF assimilated profiles were used as input data.

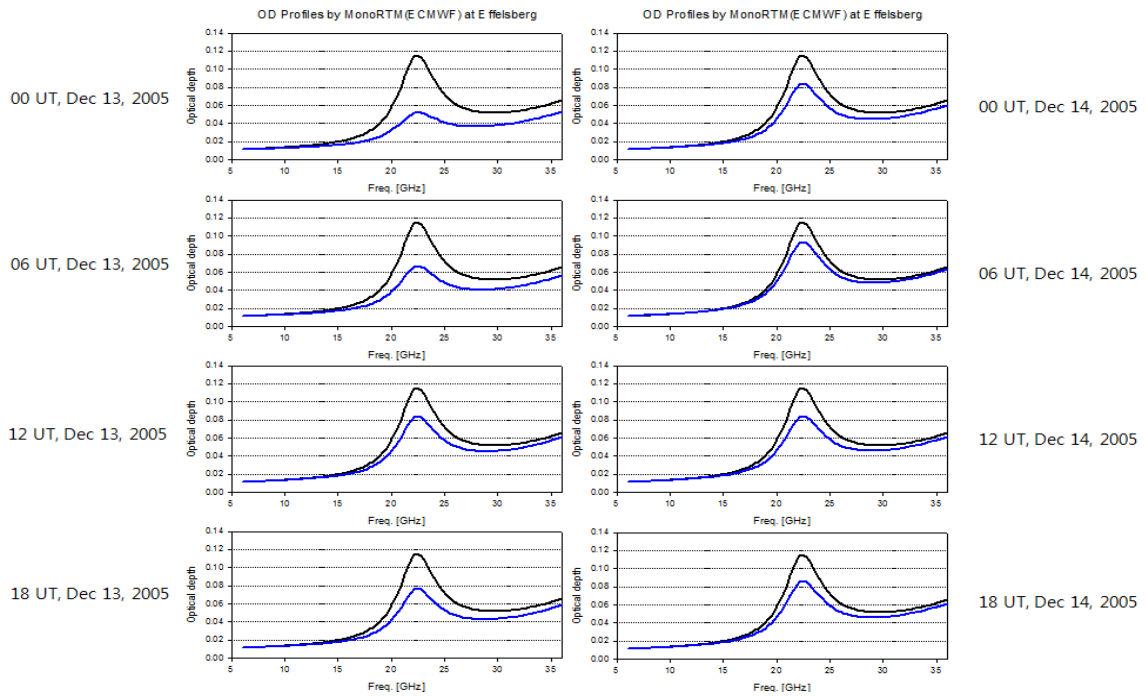


Figure A.3-1. MonoRTM(ECMWF) results of optical depth during IVS Europe session with Effelsberg (13-14 Dec. 2005)

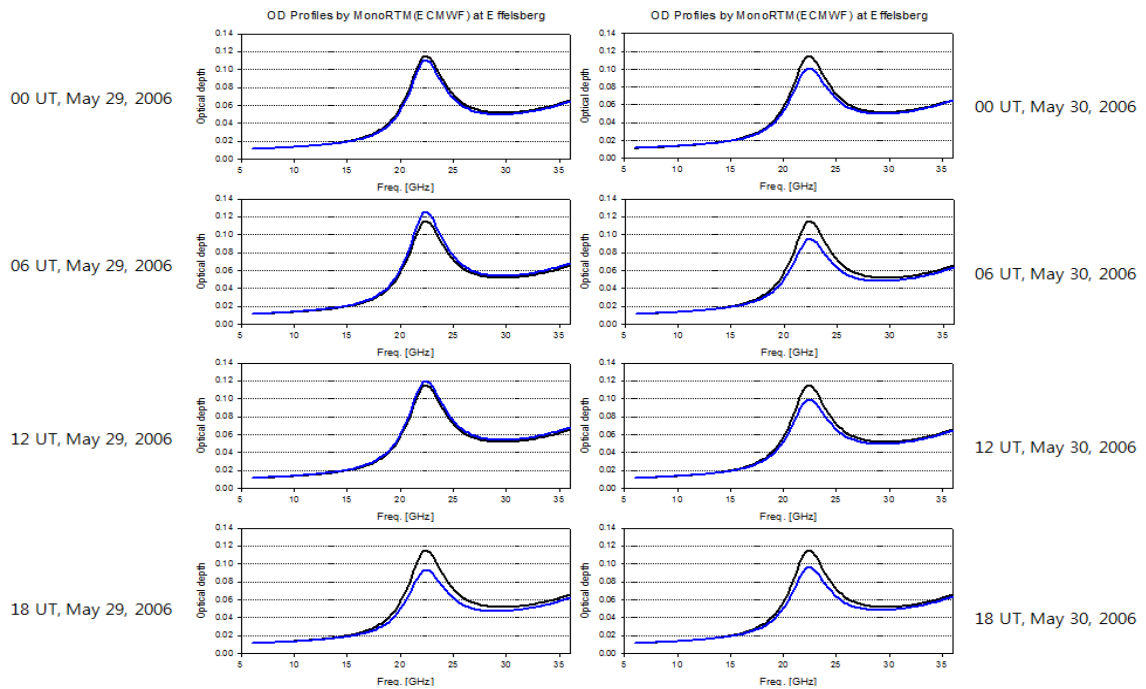


Figure A.3-2. MonoRTM(ECMWF) results of optical depth during IVS Europe session with Effelsberg (29-30 May 2006)

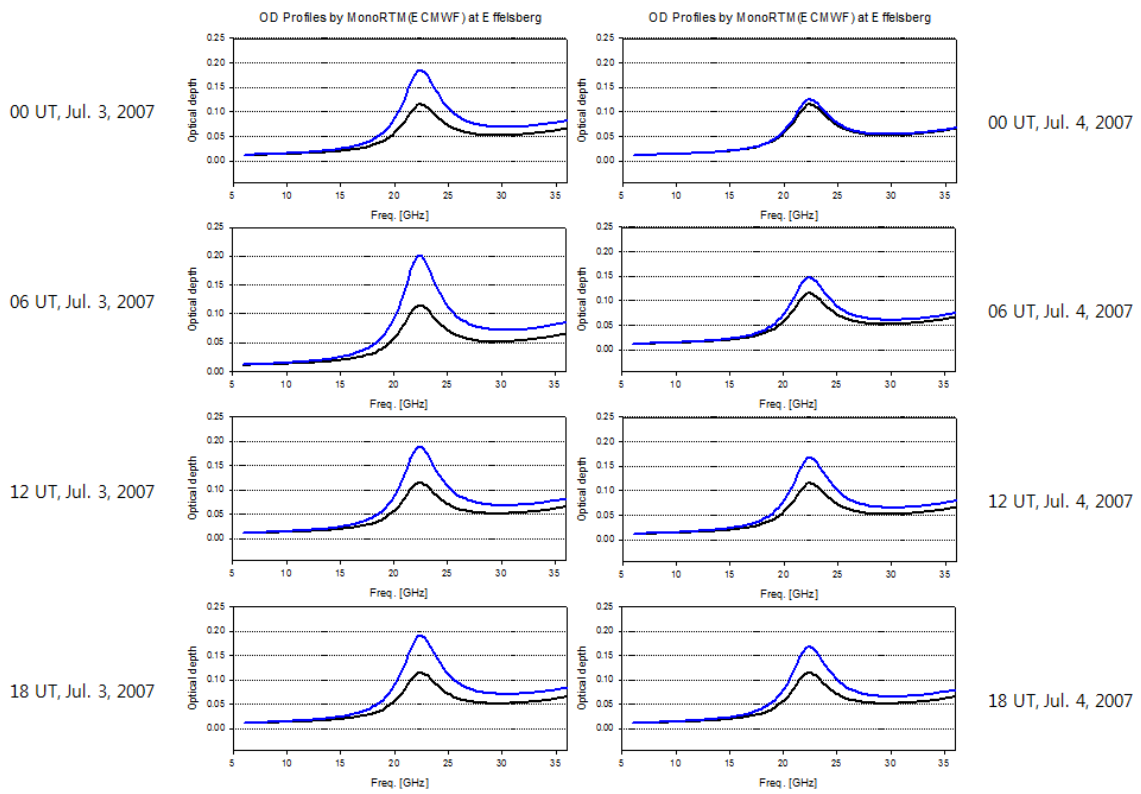


Figure A.3-3. MonoRTM(ECMWF) results of optical depth during IVS Europe session with Effelsberg (3-4 Jul. 2007)

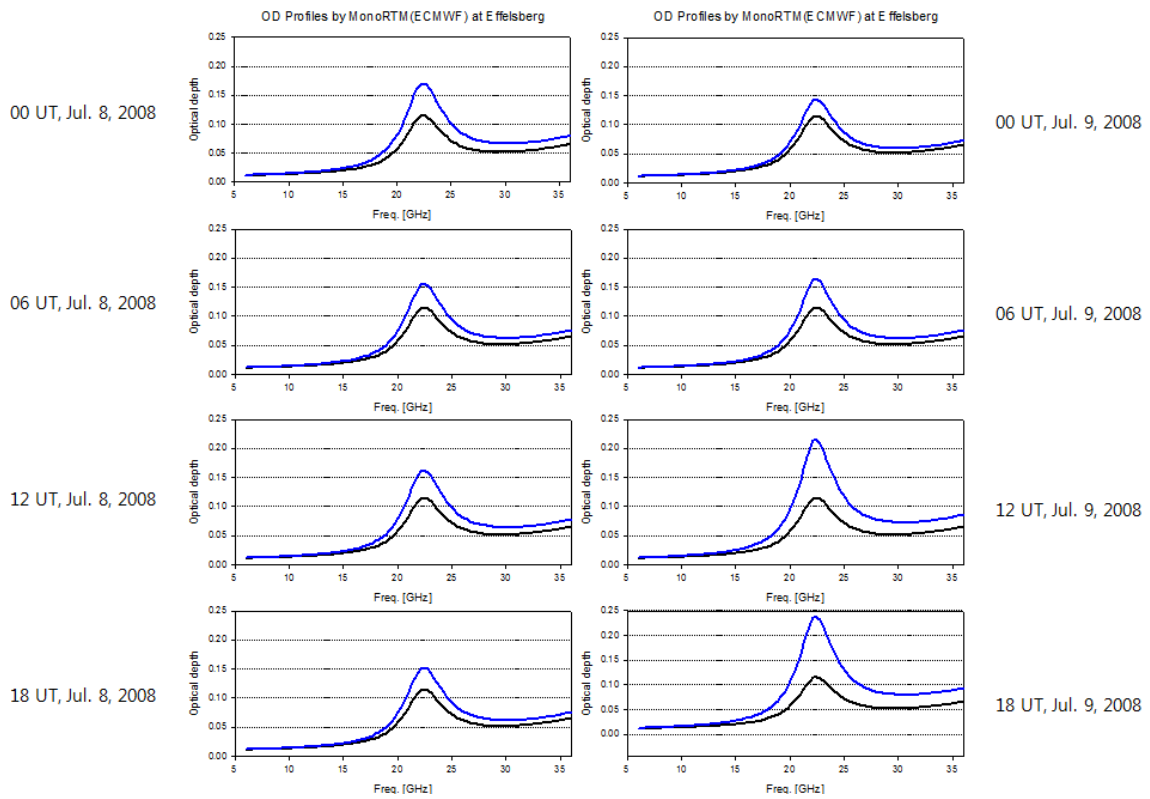


Figure A.3-4. MonoRTM(ECMWF) results of optical depth during IVS Europe session with Effelsberg (8-9 Jul. 2008)

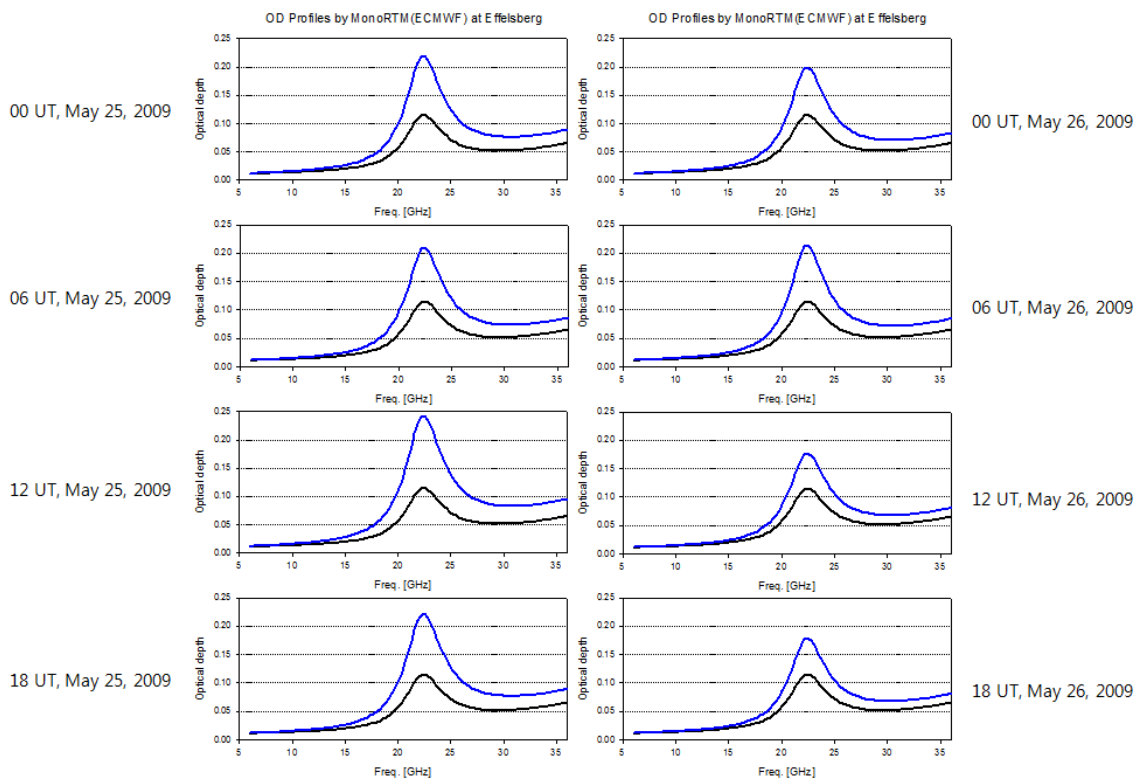


Figure A.3-5. MonoRTM(ECMWF) results of optical depth during IVS Europe session with Effelsberg (25-26 May 2009)

## A.4 Brightness temperatures from the WVR and the Models

Table A.4-1. Summary of brightness temperatures at 22.233 GHz and RMS

Sessions	Observations (K)	Calculations (K)	Obs. – Cal. (K)	RMS for all channels (K)
00 UT, Dec. 13, 2005	9.8	16.0	-6.2	4.5
06 UT, Dec. 13, 2005	15.4	19.5	-4.1	2.7
12 UT, Dec. 13, 2005	14.4	23.7	-9.3	6.6
18 UT, Dec. 13, 2005	17.0	21.9	-4.9	3.1
00 UT, Dec. 14, 2005	17.7	23.7	-6.0	4.1
06 UT, Dec. 14, 2005	22.7	25.9	-3.2	2.2
12 UT, Dec. 14, 2005	32.2	23.7	+8.5	11.8
18 UT, Dec. 14, 2005	25.1	24.3	+0.8	3.4
00 UT, May 29, 2006	24.5	30.3	-5.8	3.6
06 UT, May 29, 2006	29.0	33.5	-4.5	3.1
12 UT, May 29, 2006	28.0	32.3	-4.3	3.0
18 UT, May 29, 2006	38.4	26.0	+12.4	14.3
00 UT, May 30, 2006	8.1	27.7	-19.6	15.8
06 UT, May 30, 2006	43.1	26.2	+16.9	20.9
12 UT, May 30, 2006	61.0	27.3	+33.7	37.7
18 UT, May 30, 2006	20.4	26.5	-6.1	3.8
00 UT, Jul. 03, 2007	43.6	48.2	-4.6	7.8
06 UT, Jul. 03, 2007	45.6	51.3	-5.7	5.8
12 UT, Jul. 03, 2007	51.4	48.6	+2.8	12.2
18 UT, Jul. 03, 2007	38.5	49.4	-10.9	6.2
00 UT, Jul. 04, 2007	37.9	34.3	+3.6	12.4
06 UT, Jul. 04, 2007	39.8	39.1	+0.7	8.8
12 UT, Jul. 04, 2007	38.6	43.8	-5.2	5.8
18 UT, Jul. 04, 2007	43.9	44.1	-0.2	9.6
00 UT, Jul. 08, 2008	35.8	44.7	-8.9	4.6
06 UT, Jul. 08, 2008	20.5	41.2	-20.7	14.0
12 UT, Jul. 08, 2008	30.0	42.9	-12.9	7.3
18 UT, Jul. 08, 2008	23.1	40.4	-17.3	10.7
00 UT, Jul. 09, 2008	31.6	38.4	-6.8	3.9
06 UT, Jul. 09, 2008	26.8	43.0	-16.2	10.0
12 UT, Jul. 09, 2008	52.0	54.4	-2.4	5.3
18 UT, Jul. 09, 2008	70.3	59.6	+10.7	17.8
00 UT, May 25, 2009	48.4	56.7	-8.3	7.5
06 UT, May 25, 2009	63.4	54.4	+9.0	18.5
12 UT, May 25, 2009	69.8	62.1	+7.7	23.4
18 UT, May 25, 2009	67.1	57.9	+9.2	19.6
00 UT, May 26, 2009	41.4	53.0	-11.6	8.7
06 UT, May 26, 2009	63.4	55.1	+8.3	18.4
12 UT, May 26, 2009	51.6	46.8	+4.8	15.5
18 UT, May 26, 2009	51.9	46.2	+5.7	12.6
Average $\pm$ S.D.	37.3 $\pm$ 17.0	39.1 $\pm$ 12.9	-1.8 $\pm$ 10.6	10.2 $\pm$ 7.3

## A.5 Transformation factor

Bevis et al. (1994) introduced the transformation factor, which are corresponding to the ZWD/PWV ratio

$$\text{Transformation factor} = \frac{ZWD}{PWV}$$

$$ZWD = PWV \times \text{Transformation factor}$$

The water vapour weighted mean temperature  $T_m$  can be calculated by the equation (Bevis *et al.*, 1994)

$$T_m = 0.72 T_s + 70.2$$

where  $T_s$  is surface temperature.

Then, well-known equation of the transformation by Bevis can be used for calculation of the dimensionless parameter

$$\text{Transformation Factor} = \frac{10^6}{\rho_w \left( \frac{k_3}{T_m} + k'_2 \right) R_v}$$

where  $\rho_w$  is the density of liquid water [ $\text{kg}/\text{m}^3$ ],  $k_3$  is  $3.739 \pm 0.012$  [ $10^5 \text{ K}^2/\text{mbar}$ ],  $k'_2$  is  $22.1 \pm 2.2$  [ $10^5 \text{ K}^2/\text{mbar}$ ], and  $R_v$  is the specific gas constant for water vapour, equal to  $461.524$  [ $\text{J}/\text{kg}/\text{K}$ ].

Table A.5-1. Summary of PWV and transformation factors

Sessions	PWV [mm]	Transformation factors
00 UT, Dec. 13, 2005	5.4	6.53
06 UT, Dec. 13, 2005	7.4	6.54
12 UT, Dec. 13, 2005	9.7	6.51
18 UT, Dec. 13, 2005	8.6	6.52
00 UT, Dec. 14, 2005	9.6	6.53
06 UT, Dec. 14, 2005	11.2	6.54
12 UT, Dec. 14, 2005	10.0	6.51
18 UT, Dec. 14, 2005	10.1	6.50
00 UT, May 29, 2006	13.1	6.43
06 UT, May 29, 2006	15.1	6.42
12 UT, May 29, 2006	14.7	6.40
18 UT, May 29, 2006	11.1	6.47
00 UT, May 30, 2006	12.2	6.49
06 UT, May 30, 2006	11.3	6.50
12 UT, May 30, 2006	12.0	6.46
18 UT, May 30, 2006	11.5	6.49
00 UT, Jul. 03, 2007	23.7	6.36
06 UT, Jul. 03, 2007	25.5	6.36
12 UT, Jul. 03, 2007	23.8	6.34
18 UT, Jul. 03, 2007	24.7	6.34
00 UT, Jul. 04, 2007	15.5	6.39
06 UT, Jul. 04, 2007	18.7	6.38
12 UT, Jul. 04, 2007	21.4	6.32
18 UT, Jul. 04, 2007	21.6	6.36
00 UT, Jul. 08, 2008	21.9	6.36
06 UT, Jul. 08, 2008	19.8	6.35
12 UT, Jul. 08, 2008	20.9	6.32

18 UT, Jul. 08, 2008	19.4	6.32
00 UT, Jul. 09, 2008	18.1	6.38
06 UT, Jul. 09, 2008	20.2	6.35
12 UT, Jul. 09, 2008	26.7	6.30
18 UT, Jul. 09, 2008	30.3	6.33
00 UT, May 25, 2009	28.5	6.35
06 UT, May 25, 2009	27.2	6.32
12 UT, May 25, 2009	32.1	6.10
18 UT, May 25, 2009	29.4	6.26
00 UT, May 26, 2009	26.1	6.30
06 UT, May 26, 2009	27.0	6.28
12 UT, May 26, 2009	23.1	6.22
18 UT, May 26, 2009	22.8	6.34



## A.6 Layer-summed method

For the layer-summed method, equation (4.3) can be re-written using equation (4.4)

$$d = 10^{-6} \int 3.776 \times 10^5 \frac{P_f}{T^2} dl$$

$$d = 10^{-6} \sum_{i=1}^{19} 3.776 \times 10^5 \frac{P_f}{T^2} h_i$$

where  $h_i$  is MonoRTM layer thickness. Table A.6-1 summarizes the thickness of each layer. The first layer starts from 369 meter which is the height of the VLBI reference point of the Effelsberg telescope. Figure A.6-1 shows an example of the path delay for each layer. Although the water vapour partial pressure is mostly concentrated in the lowest layer, the path delay of the first layer is smaller than the one of the second layer just because of the thinner thickness of the first layer.

Table A.6-1. Summary of lower and upper altitudes of MonoRTM layers

Lower alt. [m]	Upper alt. [m]	Thickness [m]	Path delay [mm]
369	700	331	11.0
700	1,400	700	14.9
1,400	2,100	700	5.2
2,100	2,800	700	1.9
2,800	3,500	700	0.9
3,500	4,200	700	0.6
4,200	4,900	700	0.5
4,900	5,600	700	0.4
5,600	6,300	700	0.3
6,300	7,000	700	0.2
7,000	7,700	700	0.1
7,700	8,400	700	0.1
8,400	9,200	800	0.1
9,200	10,000	800	0.0
10,000	10,800	800	0.0
10,800	13,400	2,600	0.0
13,400	15,900	2,500	0.0
15,900	18,400	2,500	0.0
18,400	20,000	1,600	0.0

An example of the layer summed method (00UT, Dec. 13, 2005)

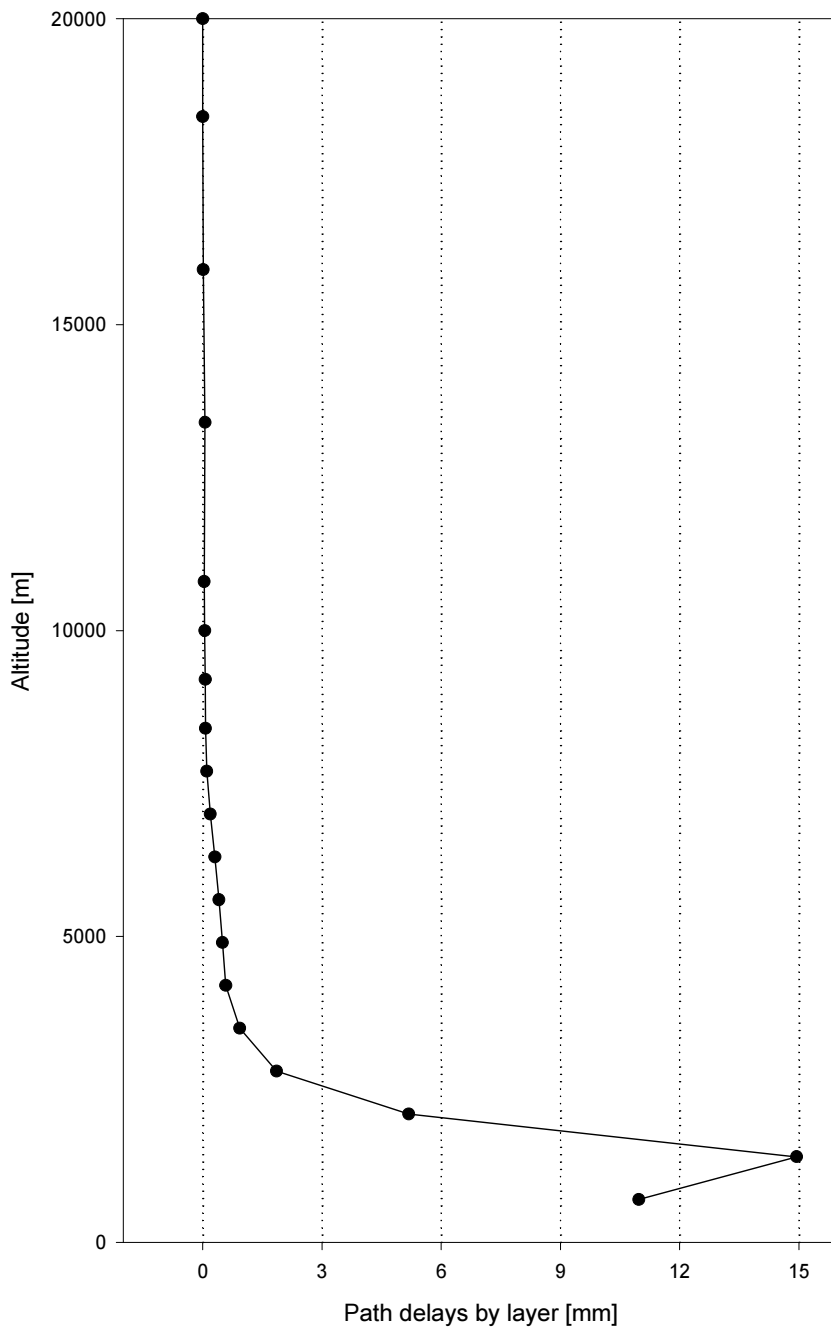


Figure A.6-1. An example of the layer-summed method for Euro78 (00UT, Dec. 13, 2005)

## A.7 Summary of ZWDs from the WVR, the Models and GPS

Table A.7-1. Summary of ZWDs

Sessions	Averaged WVR (mm)	Models (mm)	GPS (mm)
00 UT, Dec. 13, 2005	19.8	35.3	-
06 UT, Dec. 13, 2005	33.8	48.4	-
12 UT, Dec. 13, 2005	39.4	63.1	-
18 UT, Dec. 13, 2005	38.8	56.1	-
00 UT, Dec. 14, 2005	55.9	62.7	-
06 UT, Dec. 14, 2005	55.4	73.2	-
12 UT, Dec. 14, 2005	43.6	65.1	-
18 UT, Dec. 14, 2005	52.0	65.6	-
00 UT, May 29, 2006	69.3	84.2	-
06 UT, May 29, 2006	72.7	96.9	-
12 UT, May 29, 2006	62.1	94.1	-
18 UT, May 29, 2006	54.1	71.8	-
00 UT, May 30, 2006	48.2	79.2	-
06 UT, May 30, 2006	44.9	73.5	-
12 UT, May 30, 2006	44.1	77.5	-
18 UT, May 30, 2006	51.3	74.6	-
00 UT, Jul. 03, 2007	102.1	150.7	150.0
06 UT, Jul. 03, 2007	121.7	162.2	168.0
12 UT, Jul. 03, 2007	96.9	150.9	163.0
18 UT, Jul. 03, 2007	90.6	156.6	146.0
00 UT, Jul. 04, 2007	63.9	99.0	123.0
06 UT, Jul. 04, 2007	78.3	119.3	129.0
12 UT, Jul. 04, 2007	82.3	135.2	133.0
18 UT, Jul. 04, 2007	86.9	137.4	151.0
00 UT, Jul. 08, 2008	99.3	139.3	156.0
06 UT, Jul. 08, 2008	62.5	125.7	135.0
12 UT, Jul. 08, 2008	80.7	132.1	130.0
18 UT, Jul. 08, 2008	69.7	122.6	117.0
00 UT, Jul. 09, 2008	73.9	115.5	125.0
06 UT, Jul. 09, 2008	88.4	128.3	115.0
12 UT, Jul. 09, 2008	134.7	168.2	159.0
18 UT, Jul. 09, 2008	162.6	191.8	217.0
00 UT, May 25, 2009	147.1	181.0	189.0
06 UT, May 25, 2009	155.6	171.9	170.0
12 UT, May 25, 2009	209.7	195.8	187.0
18 UT, May 25, 2009	127.6	184.0	182.0
00 UT, May 26, 2009	143.9	164.4	170.0
06 UT, May 26, 2009	147.5	169.6	162.0
12 UT, May 26, 2009	126.2	143.7	152.0
18 UT, May 26, 2009	64.7	144.6	164.0
Average $\pm$ S.D.	85.1 $\pm$ 42.6	117.8 $\pm$ 45.1	-
Last 3 sessions	109.0 $\pm$ 38.3	149.6 $\pm$ 25.5	153.9 $\pm$ 25.4

Table A.7-2. Comparisons between ZWDs in mm

	Min.	Max.		Mean	S.D.
Averaged WVR	62.5	209.7	GPS- Averaged WVR	44.8	24.0
Models	99.0	195.8	GPS-Models	4.3	11.0
GPS	115.0	217.0			

The comparisons are just for the last three sessions because of the availability of GPS at Effelsberg.

## A.8 Baseline-length

Table A.8-1. Baseline-length for Effelsberg-Wetzell

Years	Length [+457481700 mm]	Sigma [mm]
1992.9210	46.3	2.0
1993.9500	44.7	1.6
1994.3250	45.0	1.7
1994.8230	41.4	2.1
1995.2830	32.1	3.7
1995.9360	39.8	1.4
1996.8460	44.0	3.1
1996.9330	43.7	1.1
1997.9400	40.5	1.8
1999.9540	30.4	1.8
2000.9370	36.0	2.4
2003.9630	40.6	0.7
2006.8750	44.9	1.3
2009.9090	49.7	1.9

Table A.8-2. Baseline-length for Effelsberg-Onsala

Years	Length [+832210450 mm]	Sigma [mm]
1992.9210	43.5	2.6
1993.9500	49.2	1.8
1994.3250	41.6	3.5
1994.8230	44.2	2.3
1995.2830	41.5	3.4
1995.9360	43.3	1.9
1996.8460	53.6	4.0
1996.9330	45.5	1.6
1997.9400	55.9	2.7
1999.9540	41.7	1.8
2000.9370	58.6	3.4
2003.9630	38.4	0.9
2006.8750	37.7	1.7
2009.9090	54.9	1.9
2010.5120	40.3	2.3

Table A.8-3. Summary of baseline lengths for Effelsberg-Wetzell baseline

	Baseline length + 457481700 [mm]			
	SOLVE-estimated	WVR-measured	WVR-smoothed	Readjusted by offset
Euro78	38.2 ± 2.8	36.9 ± 2.8	36.7 ± 2.8	34.5 ± 2.8
Euro81	50.4 ± 8.5	51.4 ± 8.5	48.4 ± 8.4	44.5 ± 8.5
Euro88	48.4 ± 2.8	51.8 ± 3.3	49.9 ± 3.0	46.6 ± 2.9
Euro94	46.1 ± 2.2	47.1 ± 2.9	45.2 ± 2.6	41.8 ± 2.6
Euro99	48.1 ± 1.8	50.3 ± 1.7	54.0 ± 2.2	50.6 ± 2.2
RMS	5.9	7.9	7.7	5.9
WRMS	4.6	6.7	7.6	5.9

Table A.8-4. Summary of baseline lengths for Effelsberg-Onsala baseline

	Baseline length + 832210450 [mm]			
	SOLVE-estimated	WVR-measured	WVR-smoothed	Readjusted by offset
Euro78	23.6 ± 3.0	23.1 ± 2.6	22.1 ± 2.6	15.8 ± 2.7
Euro81	44.7 ± 9.0	38.6 ± 7.9	43.6 ± 7.9	31.9 ± 7.9
Euro88	35.9 ± 2.9	41.1 ± 3.4	41.8 ± 3.0	30.6 ± 3.0
Euro94	50.0 ± 2.8	59.4 ± 3.0	57.4 ± 2.7	37.2 ± 2.6
Euro99	48.1 ± 2.2	45.6 ± 2.1	38.4 ± 2.1	31.2 ± 2.1
RMS	12.3	13.9	13.8	19.8
WRMS	11.0	12.7	13.3	18.1

## A.9 Height precision

Table A.9-1. Mean height since the episodic motion in Effelsberg in Oct. 1996

Years	Component [mm]	Sigma [mm]
1996.8460	32.7	11.3
1996.9330	31.1	4.4
1997.9400	62.9	7.2
1999.9540	35.9	7.8
2000.9370	26.4	9.4
2003.9630	25.1	3.1
2006.8750	80.1	5.7
2009.9090	28.4	8.2
2010.5120	64.5	13.6
Mean	43.0 ± 20.4	-

Table A.9-2. Summary of the Up-down component variations for the five sessions

	SOLVE-estimated	WVR-measured	WVR-smoothed	Readjusted by offset
	Comp. ± σ [mm]	Comp. ± σ [mm]	Comp. ± σ [mm]	Comp. ± σ [mm]
Euro78	37.1 ± 11.5	9.4 ± 5.8	17.5 ± 5.8	-26.9 ± 5.8
Euro81	82.0 ± 35.9	46.8 ± 13.1	58.7 ± 13.1	-26.9 ± 13.2
Euro88	4.0 ± 11.7	59.5 ± 8.8	68.8 ± 8.4	-44.5 ± 8.2
Euro94	63.4 ± 9.3	61.9 ± 8.4	63.4 ± 7.8	-9.2 ± 7.8
Euro99	42.7 ± 7.8	-7.2 ± 6.8	29.3 ± 5.8	-32.8 ± 5.8
Mean	45.8	34.1	47.5	-28.1

## List of Figures

1-1	Conceptual diagram from the cascade process to the brightness temperature by RT model .....	8
1-2	Microwave signal propagation at two separate geodetic VLBI stations .....	10
1-3	Signal propagation through the atmosphere .....	11
2-1	Atmospheric windows at Effelsberg .....	17
2-2	Block diagram of a switched radiometer .....	18
2-3	Geometry of the radiative transfer equation .....	20
2-4	WVR observational frequency selections for typical two-channel and multi-channel instruments .....	24
2-5	European geodetic VLBI network .....	30
2-6	WVR instruments on the Effelsberg 100m radio telescope and Onsala Space Observatory .....	30
2-7	Comparison of zenith wet delays (ZWD) simultaneously measured by the three WVR .....	32
2-8	Comparison of ZWDs from the Effelsberg WVR, radiosondes, and GPS .....	33
3-1	ECMWF profiles for temperatures and water vapour partial pressures for Euro78 .....	35
3-2	Block diagram of MonoRTM in terms of data processing flow .....	37
3-3	MonoRTM calculated optical depths from either water vapour, oxygen, or both .....	38
3-4	MonoRTM calculated brightness temperature corresponding to different models .....	39
3-5	Differences between normal calculation of US standard model and the self component being switched-off .....	39
3-6	Differences between normal calculation of US standard model and the foreign component being switched-off .....	40
3-7	Differences between normal calculation of US standard model and both components being switched-off .....	40
3-8	Spectrum comparison between MonoRTM(ECMWF) and WVR for Euro78 .....	43
3-9	Spectrum comparison between MonoRTM(ECMWF) and WVR for Euro81 .....	44
3-10	Spectrum comparison between MonoRTM(ECMWF) and WVR for Euro88 .....	44
3-11	Spectrum comparison between MonoRTM(ECMWF) and WVR for Euro94 .....	45
3-12	Spectrum comparison between MonoRTM(ECMWF) and WVR for Euro99 .....	45
3-13	Comparison of peak brightness temperatures and its offset and RMS for all channels .....	47
3-14	Effects of 1% error increments on water vapour partial pressure and temperature .....	48
4-1	An example of the averaged ZWDs for one ECMWF epoch .....	51
4-2	Averaged ZWDs at Effelsberg .....	51
4-3	Comparison between the transformed ZWDs and the layer-summed ZWDs .....	52
4-4	Comparison between ZWDs .....	53
4-5	Differences between GPS-derived ZWDs and ZWDs from the two approaches .....	55
4-6	Correlation between GPS-derived ZWDs, model-calculated ZWDs, and WVR-observed ZWDs .....	56
4-7	ZWDs from the WVR observations and the model calculations .....	57
4-8	Linear regression lines of the two approaches .....	57
4-9	ZWDs from the three approaches for the Euro78 .....	58
4-10	ZWDs from the three approaches for the Euro81 .....	59
4-11	ZWDs from the three approaches for the Euro88 .....	59
4-12	ZWDs from the three approaches for the Euro94 .....	60
4-13	ZWDs from the three approaches for the Euro99 .....	60
5-1	ZWD estimates from SOLVE and the three approaches for the Euro78 .....	63
5-2	Differences of the three approaches with respect to the SOLVE-estimated ZWDs for the Euro78 .....	63
5-3	ZWD estimates from SOLVE and the three approaches for the Euro81 .....	64
5-4	Differences of the three approaches with respect to the SOLVE-estimated ZWDs for the Euro81 .....	64
5-5	ZWD estimates from SOLVE and the three approaches for the Euro88 .....	65
5-6	Differences of the three approaches with respect to the SOLVE-estimated ZWDs for the Euro88 .....	65
5-7	ZWD estimates from SOLVE and the three approaches for the Euro94 .....	66



5-8	Differences of the three approaches with respect to the SOLVE-estimated ZWDs for the Euro94 .....	66
5-9	ZWD estimates from SOLVE and the three approaches for the Euro99 .....	67
5-10	Differences of the three approaches with respect to the SOLVE-estimated ZWDs for the Euro99 .....	67
5-11	Mean and RMS of ZWDs from SOLVE and the three approaches .....	68
5-12	Baseline evolution between Effelsberg and Wettzell .....	70
5-13	Baseline evolution between Effelsberg and Onsala .....	70
5-14	Variation in baseline and vertical component between Effelsberg and Wettzell .....	72
5-15	Variation in baseline and vertical component between Effelsberg and Onsala .....	73
5-16	Change in height components by the four solutions for mean height since the episodic motion .....	74
5-17	Change in height components by the four solutions for mean height of each solution .....	75
A.1-1	ECMWF profiles for temperatures and water vapour partial pressures for the Euro81 .....	80
A.1-2	ECMWF profiles for temperatures and water vapour partial pressures for the Euro88 .....	80
A.1-3	ECMWF profiles for temperatures and water vapour partial pressures for the Euro94 .....	81
A.1-4	ECMWF profiles for temperatures and water vapour partial pressures for the Euro99 .....	81
A.2-1	The format of the meteorological profile for MonoRTM .....	82
A.3-1	MonoRTM(ECMWF) results of optical depth for the Euro78 .....	83
A.3-2	MonoRTM(ECMWF) results of optical depth for the Euro81 .....	83
A.3-3	MonoRTM(ECMWF) results of optical depth for the Euro88 .....	84
A.3-4	MonoRTM(ECMWF) results of optical depth for the Euro94 .....	84
A.3-5	MonoRTM(ECMWF) results of optical depth for the Euro99 .....	85
A.6-1	An example of the layer-summed method for the Euro78 .....	90

## List of Tables

2-1	Summary of commonly-used absorption models .....	23
2-2	Summary of several WVR instruments .....	27
2-3	Summary of the five sessions .....	30
2-4	Specifications of Effelsberg's WVR .....	31
4-1	Summary of the mean offsets in the readjustments approach .....	57
5-1	Solution types and descriptions for ZWDs comparisons .....	62
5-2	Mean and RMS of ZWDs from SOLVE and the three approaches .....	68
5-3	Mean offset and RMS of ZWDs with respect to the SOLVE-estimates .....	69
5-4	Solution type and description for baseline repeatability comparisons .....	71
A.2-1	Summary of integrated column density from the surface to the top of the layer .....	82
A.4-1	Summary of brightness temperatures at 22.233 FGz and RMS .....	86
A.5-1	Summary of PWV and transformation factors .....	87
A.6-1	Summary of lower and upper altitude of MonoRTM layers .....	89
A.7-1	Summary of ZWDs .....	91
A.7-2	Comparisons between ZWDs in mm .....	92
A.8-1	Baseline-length for Effelsberg- Wettzell .....	93
A.8-2	Baseline-length for Effelsberg- Onsala .....	93
A.8-3	Summary of baseline lengths for Effelsberg- Wettzell baseline .....	93
A.8-4	Summary of baseline lengths for Effelsberg- Onsala baseline .....	94
A.9-2	Mean height since the episodic motion in Effelsberg in Oct. 1996 .....	95
A.9-2	Summary of Up-down component variation for the five sessions .....	95

## References

- Askne, J., and H. Nordius (1987) *Estimation of tropospheric delay for microwaves from surface weather data*. Radio Science, Vol. 22, pp. 379-386
- Bar-Sever, Y., S. Byun, R. Haas, S. Keihm, T. Munson, A. Tanner, L. Young (2004) *A multi-sensor approach to the estimation of line of sight tropospheric delay*. Pasadena, CA : Jet Propulsion Laboratory, National Aeronautics and Space Administration
- Behrend, D., L. Cucurull, J. Vila, and R. Haas (2000), *An inter-comparison study to estimate zenith wet delays using VLBI, GPS, and NWP models*. Earth Planets Space, Vol. 52, pp. 691-694
- Behrend, D., R. Haas, D. Pino, L.P. Gradinarsky, S.J. Keihm, W. Schwarz, L. Cucurull, and A. Rius (2002) *MM5 derived ZWDs compared to observational results from VLBI, GPS, and WVR*. Physics and Chemistry of the Earth, 27, pp. 301-308
- Bevis, M., S. Businger, T.A. Herring, C. Rocken, A. Anthes, and R. Ware (1992) *GPS Meteorology: Remote sensing of atmospheric water vapor using the Global Positioning System*. J. Geophys. Res., Vol. 97, pp. 15787-15801
- Bevis, M., S. Businger, S. Chiswell, T.A. Herring, R.A. Anthes, C. Rocken, and R.H. Ware (1994) *GPS Meteorology: Mapping zenith wet delays onto precipitable water*. J. of Applied Meteorology, Vol. 33, pp. 379-386
- Böhm, J., and H. Schuh (2004) *Vienna mapping functions in VLBI analyses*. Geophys. Res. Lett., doi:10.1029/2003GL018984, 31, pp. L01603
- Böhm, J., B. Werl, and H. Schuh (2006) *Troposphere mapping functions for GPS and very long baseline interferometry from European Centre for Medium Range Weather Forecasts operational analysis data*. J. Geophys. Res., doi:10.1029/2005JB003629, 101, pp. B02406
- Böhm, J. (2010) Vienna University of Technology, Private communication, October 2010
- Chandrasekhar, S. (1960) *Radiative Transfer*. Dover Publications, New York
- Chao, C.C. (1970) *A preliminary estimation of tropospheric influence on the range and range rate data during the closest approach of the MM 71 Mars Mission*. JPL Tech. Memo, p. 391
- Cho., J. A. N. Nothnagel, M. Vennebusch, and D. Fischer (2005) *Preliminary results of applying WVR calibration to European VLBI data*. Proceedings of the 17<sup>th</sup> Working Meeting on European VLBI for Geodesy and Astrometry, Noto, Italy, April 22-23, 2005, pp. 96-101
- Cimini, C., F.S. Marzano, P. Ciotti, Y. Han, D. Cimini, S.J. Keihm, E.R. Westwater, R. Ware (2004) *Atmospheric Microwave Radiative Models Study Based on Ground-Based Multichannel Radiometer Observations in the 20-60 GHz Band*. Fourteenth ARM Science Team Meeting Proceedings, Albuquerque, New Mexico, March 22-26, 2004
- Clough, S. A., F. X. Kneizys, and R. W. Davies (1989) *Line shape and the water vapor continuum*. Atmos. Res., Vol. 23, pp. 229-241
- Clough S.A., M.J. Iacono, and J.-L. Moncet (1992) *Line-by-line calculation of atmospheric fluxes and cooling rates: Application to water vapor*. J. of Geophys. Res., Vol. 97, 15761-15785
- Clough S.A. and M.J. Iacono (1995) *Line-by-line calculation of atmospheric fluxes and cooling rates: Application to carbon dioxide, ozone, methane, nitrous oxide, and halocarbons*. J. of Geophys. Res., Vol. 100, 16519-16535
- Clough S.A., M.W. Sheppard, E.J. Mlawer, J.S. Delamere, M. Iacono, K.E. Cady-Pereira, S. Boukabara, and P.D. Brown (2005) *Atmospheric radiative transfer modeling: A summary of AER codes*. J. Quant. Spectrosc. Radiat. Transfer, Vol. 91, pp. 233-244
- Combrinck, L. and M. Nickola (2005) *Hartebeesthoek Radio Astronomy Observatory (HartRAO)*. IVS 2005 Annual Report, pp. 77-80
- Coster, A.J., A.E. Niell, F.S. Solheim, V.B. Mendes, P.C. Toor, K. P. Buchmann, and C. A. Upham (1996) *Measurements of Precipitable Water Vapor by GPS, Radiosondes, and a Microwave Water Vapor Radiometer*. ION-GPS, Kansas city, September 17-20, 1996
- Coster, A.J., A.E. Niell, F.S. Solheim, V.B. Mendes, P.C. Toor, R.B. Langley, and C. A. Ruggles (1996) *The Westford Water Vapor Experiment: Use of GPS to determine total precipitable water vapor*. ION-GPS 52th Annual meeting, Cambridge, MA, June 19-21, 1996
- Crewell, S., and U. Löhnert (2003) *Accuracy of cloud liquid water path from ground-based microwave radiometry. Part II. Sensor accuracy and synergy*. Radio Science, Vol. 38(3), 8042, doi:10.1029/2002RS002634
- Cruz, S.L., C.S. Ruf, and S.J. Keihm (1998) *Improved 20- to 32-GHz atmospheric absorption model*. Radio Sci., Vol. 33, pp. 1319-1333
- Davis, J.L., T.A. Herring, I.I. Shapiro, A.E.E. Rogers, and G. Elgered (1985) *Geodesy by Radio Interferometry: Effects of atmospheric modeling errors on estimates of baseline length*. Radio Science, Vol. 20, pp. 1593-1607
- Delamere, J.S., S.A. Clough, E.J. Mahler, S.-A. Boukabara, K. Cady-Periera, M. Sheppard (2004) *An update on radiative transfer model development at Atmospheric & Environmental Research Inc*. Proceedings of 12th ARM Science Team Meeting, St. Petersburg, Florida, April 8-12, 2004

- Dickinson, D.F., M.D. Grossi, and M.R. Perlmann (1970) *Refractive corrections in high-accuracy radio interferometry*. J. Geophys. Res., Vol. 75, pp. 1619-1621
- Elgered, G., J. L. Davis, T. A. Herring, and I. I. Shapiro (1991) *Geodesy by Radio Interferometry: Water Vapor Radiometry for Estimation of Wet Delay*. J. Geophys. Res., Vol. 96, B4, pp. 6541-6555
- Elgered, G. (1993) *Tropospheric radio path delay from ground-based microwave radiometry*. Atmospheric remote sensing by microwave radiometry, M.A. Janssen ed., John Wiley & Sons, New York, pp. 215-258
- Elgered, G. and P.O.J. Jarlemark (1998) *Ground-Based Microwave Radiometry and Long-Term Observations of Atmospheric Water Vapor*. Radio Science, Vol. 33, pp. 707-717
- Gabor, M. (1997) *Remote Sensing of Water Vapor From GPS Receivers*. ASE 389P-Remote Sensing from Space, University of Texas at Austin
- Gradinarsky, L.P., R. Haas, G. Elgered, and M. Johansson (2000) *Wet path delay and delay gradients inferred from microwave radiometer, GPS, and VLBI observation*. Earth Planets Space, Vol. 52, pp. 695-698
- Gross, E.P. (1955) *Shape of Collision-Broadened Spectral Lines*. Phys. Rev., Vol. 97, pp. 395-403
- Haas, R. and G. Elgered (2007) *The IVS Network Station Onsala Space Observatory*. IVS 2007 Annual Report, p. 84
- Haas, R., H.-G. Scherneck, and T. Nilsson (2008) *Onsala Space Observatory – IVS Analysis Center*. IVS 2008 Annual Report, pp. 295-296
- Häfele, P., M. Becker, M. Kirchner, L. Martin and E. Brockmann (2004) *Impact of WVR Measurements on Troposphere and Height Estimates by GPS*. ION GNSS 2004 meeting, Session F5 GPS Meteorology, Long Beach, September 21-24, 2004
- Häfele, P., M. Becker, E. Brockmann, L. Martin, and M. Kirchner (2005) *MATRAG—Measurement of Alpine tropospheric delay by radiometer and GPS*. Proceedings of the IGS Workshop and Symposium, Bern, Switzerland, 1– 5 March 2004
- Herring, T.A. (1992) *Modelling atmospheric delays in the analysis of space geodetic data*. Symposium on Refraction of Transatmospheric Signals in Geodesy, Netherlands Geod. Commis. Ser. 36, edited by J.C. DeMunk and T.A. Spoelstra, pp. 157-164
- Hewison, T.J., C. Gaffard, and J. Nash (2003) *Validation of Microwave Radiometer Measurements in Clear Air*. ISTRP conference, Sept. 14-20, 2003, Leipzig, Germany, pp. 136–138
- Hewison, T.J. (2006a) *Profiling temperature and humidity by ground-based microwave radiometers*. Ph.D. Thesis, The University of Reading, September 2006
- Hewison, T.J., D. Cimini, L. Martin, C. Gaffard and J. Nash (2006b) *Validating clear air absorption model using ground-based microwave radiometers and vice-versa*. Meteorologische Zeitschrift, Vol. 15, 1, pp. 27-36
- Hill, R.J., R.S. Rawrence, J.T. Priestly (1982) *Theoretical and calculation aspects of the radio refractive index of water vapor*. Radio Science, Vol. 17, pp. 1251-1257
- Hopfield, H.A. (1971) *Tropospheric effect on electromagnetically measured range: prediction from surface weather data*. Radio Science, Vol. 6, pp. 357-367
- Hobiger, T., R. Ichikawa, T. Kondo, and Y. Koyama (2008) *Fast and accurate ray-tracing algorithms for real-time space geodetic applications using numerical weather models*. J. Geophys. Res., Vol. 113, pp. 1-14
- Humlicek, J. (1982) *Optimized computation of the Voigt and complex probability functions*. J. Quant. Spect. Radiative. Transfer, Vol. 27, pp. 437-444
- Ichikawa, R., H. Kuboki, M. Tsutsumi, and Y. Koyama (2006) *Zenith wet delay comparisons at Tsukuba and Kashima VLBI stations during the CONT05 VLBI campaign*. IVS NICT-TDC News, No.27, pp. 19-22
- Ifadis, I. (1986) *The atmospheric delay of radio waves: Modeling the elevation dependence on a global scale*. Technical report No. 38L, Chalmers University of Technology, Gothenburg, Sweden
- Janes, H.W., R.B. Langley, and S.P. Newby (1991) *Analysis of tropospheric delay prediction models: Comparisons with ray-tracing and implications for GPS relative positioning*, Bulletin Geodesique, Vol. 65, pp. 151-161
- Jee, G., H.-B. Lee, Y.H. Kim, J.-K. Chung, and J. Cho (2010) *Assessment of GPS global ionosphere maps (GIM) by comparison between CODE GIM and TOPEX/Jason TEC data: Ionospheric perspective*. J. Geophys. Res., doi:10.1029/2010JA015432, 115, pp. A10319
- Jin, S.G., J. Park, J. Cho, and P. Park (2007) *Seasonal variability of GPS-derived zenith tropospheric delay (1994-2006) and climate implications*. J. Geophys. Res., doi:10.1029/2006JD007772, 112, pp. D09110
- Johansson, J.M., G. Elgered, and J.L.Davis (1987) *Geodesy by radio interferometry: Optimization of wet path delay algorithms using microwave radiometer data*. Research. Report., 152, Onsala Space Observatory, Chalmers Univ. of Tech., p. 50
- Johansson, J.M., G. Elgered, and J.L. Davis (1993) *Wet path delay algorithms using microwave radiometer data. In contributions of Space Geodesy to geodynamics*. Technology D.E. Smith and D.L. Turcotte Eds., AGU Geodynamics Series, Vol. 25, pp. 81-98
- Keihm, S.J., M.A. Janssen, and C.S. Ruf (1995) *TOPEX/Poseidon Microwave Radiometer (TMR): III. Wet troposphere range correction algorithm and pre-launch error budget*. IEEE Trans. Geosci. Rem. Sensing, Vol. 33, No. 1, pp. 147-161

- Keihm, S.J., Y. Bar-Sever, and J.C. Liljegren (2002) *WVR-GPS comparison measurements and calibration of the 20-32 GHz tropospheric water vapor absorption model*. IEEE Transactions on Geoscience and Remote Sensing, 40, 6, pp. 1199-1210
- Kuehn, C.E., W.E. Himwich, T.A. Clark, and C. Ma (1991) *An evaluation of water vapor radiometer data for calibration of the WPD in VLBI experiments*. Radio Science, Vol. 26, pp. 1381-1391
- Kuehn, C.E., G. Elgered, J. M. Johansson, T. A. Clark, and B. Ronnang (1993) *A Microwave Radiometer Comparison and Its Implication for the Accuracy of Wet Delays*. Contributions of Space Geodesy to Geodynamics: Technology, Eds. D.E. Smith, and D.L. Turcotte, AGU Geodynamics Series, 25, pp. 99-114
- Lanyi, G. (1984) *Tropospheric delay effects in radio interferometry*. TDA Progress Report 42-78, Jet Propulsion Laboratory, Pasadena, pp. 152-159
- Liebe, H.J. and D.H. Layton (1987) *Millimeter wave properties of the atmosphere: Laboratory studies and propagation modeling*. National Telecommunications and Information Administration (NTIA) Report 87-24
- Liebe, H.J. (1989) *MPM – An atmospheric millimeter-wave propagation model*. Int. J. Infrared Millimeter Waves, Vol. 10(6), pp. 631-650
- Liebe, H.J., G.A. Hufford, and M.G. Cotton (1993) *Propagation modeling of moist air and suspended water/ice particles at frequencies below 1000*. AGARD Conference Proceedings 542
- Liljegren, J.C., E.E. Clothiaux, G.G. Mace, S. Kato, and X. Dong (2001) *A new retrieval for cloud liquid water path using a ground-based microwave radiometer and measurements of cloud temperature*. J. Geophys. Res., Vol. 106, pp. 14,485-14,500
- Liljegren, J.C., S.A. Boukabara, K. Candy-pereira, and S.A. Clough (2005) *The Effect of the Half-Width of the 22-GHz Water Vapor Line on Retrievals of Temperature and Water Vapor Profiles with a Twelve-Channel Microwave Radiometer*. IEEE Trans. Geosc. Rem. Sens., Vol. 43, No. 5, pp. 1102-1108
- Linfield, R.P., S.J. Keihm, L.P. Teitelbaum, S.J. Walter, M.J. Mahoney, R.N. Treuhart, and L.J. Skjerve (1994) *A test of WVR-based troposphere calibration using VLBI observations on a 21 km baseline*. Radio Science, Vol. 31, pp. 129-146
- Linfield, R., Y. Bar-Sever, and P. Kroger (1997) *Comparison of Global Positioning System and Water Vapor Radiometer wet tropospheric delay estimates*. TDA Progress Report 42-130, August 15
- Löhnert, U., and S. Crewell (2003) *Accuracy of cloud liquid water path from ground-based microwave radiometry. Part I. Dependency on Cloud model statistics*. Radio Science, Vol. 38(3), 8041, doi:10.1029/2002RS002654
- MacMillan, D.S. and C. Ma (1994) *Evaluation of very long baseline interferometry atmospheric modeling improvements*. J. Geophys. Res., Vol. 99, No. B1, pp. 637-651
- MacMillan, D.S. (1995) *Atmospheric gradients from very long baseline interferometry observations*. Geophys. Res. Lett., 22, pp. 1041-1044
- Marini, J.W. and C.W. Murray (1973) *Correction of laser range tracking data for atmospheric refraction at elevations above 10 degrees*. NASA Technical Report X-591-73-351, Goddard Space Flight Center, Greenbelt MD
- Mattioli, V., E. Westwater, S. Gutman and V. Morris (2005) *Forward Model Studies of Water Vapor using Scanning Microwave Radiometers, Global Positioning System, and Radiosondes during the Cloudiness Inter-Comparison Experiment*. IEEE Trans. Geosci. Rem. Sens., Vol. 43, No. 5, pp.1012-1021
- Melshheimer, C., C. Verdes, S.A. Buehler, C. Emde, P. Eriksson, D.G. Feist, S. Ichizawa, V.O. John, Y. Kasai, G. Kopp, N. Koulev, T. Kuhn, O.Lemke, S. Ochiai, F. Schreier, T.R. Sreerexha, M. Suzuki, C. Takahashi, S. Tsujimaru and J. Urban (2005) *Intercomparison of General Purpose Clear Sky Atmospheric Radiative Transfer Models for the Millimeter/Submillimeter Spectral Range*. Radio Sci., RS1007, doi:10.1029/2004RS003110
- Mlawer, M.J. and D.C. Tobin, and S.A. Clough (2004) *A revised perspective on the water vapor continuum: The MT\_CKD model*. Atmos. Environ. Res., Lexington, Massachusetts ([http://rtweb.aer.com/continuum\\_frame.html](http://rtweb.aer.com/continuum_frame.html))
- Mockler, S. (1995) *Water vapor in the climate system*. Special Rep., American Geophysical Union, Dec. 1995
- Moran, J.E. and B.R. Rosen (1981) *Estimation of the propagation delay through the troposphere from microwave radiometer data*. Radio Science, Vol. 16, pp. 235-244
- Niell, A.E. (1996) *Global mapping functions for the atmosphere delay at radio wavelengths*. J. Geophys. Res., Vol. 101, pp. 3227-3246
- Niell, A.E. (2000) *Improved atmospheric mapping functions for VLBI and GPS*. Earth Planets Space, Vol. 52, pp. 699-702
- Niell, A.E., A.J. Coster, F.S. Solheim, V.B. Mendes, P.C. Toor, R.B. Langley, C.A. Upham (2001) *Comparisons of measurements of atmospheric wet delay by radiosonde, water vapor radiometer, GPS, and VLBI*. J. Atmos. Oceanic Technol., Vol. 18, pp. 830-850
- Niell, A.E. (2001) *Preliminary evaluation of atmospheric mapping functions based on numerical weather models*. Phys. Chem. Earth, Vol. 26, pp. 475-480
- Niell, A. and M. Leidner (2006) *Use of NWM forecasts for converting brightness temperature to delay*. Workshop on Measurement of atmospheric water vapour: Theory, Techniques, Astronomical and Geodetic Applications, Wettzell, Germany, Oct. 9-11, 2006

- Nilsson, T. and G. Elgered (2008) *Long-term trends in the atmospheric water vapor content estimated from ground-based GPS data*. J. Geophys. Res., DOI: 10.1029/2008JD010110, 113 (D19), pp. D19101
- Nothnagel, A., M. Vennebusch, and J. Campbell (2002) *On correlation between parameters in Geodetic VLBI data analysis*. IVS 2002 General Meeting Proceedings, pp. 260-264
- Nothnagel, A., J. Cho, A. Roy, and R. Haas (2007) *WVR calibration applied to European VLBI observing sessions*. Dynamic Planet: Monitoring and Understanding a Dynamic Planet with Geodetic and Oceanographic Tools; Series: IAG Symposia, Vol. 130, Tregoning, P. and C. Rizos Eds., ISBN: 978-3-540-49349-5, Springer, Berlin, pp. 152-157
- Oswald, J., L. Riely, A. Hubbard, H. Rosenberger, A. Tanner, S. Keihm, C. Jacobs, G. Lanyi, and C. Naudet (2005) *Relocation of Advanced Water Vapor Radiometer 1 to Deep Space Station 55*. IPN Progress Report 42-163
- Owens, J.C. (1967) *Optical refractive index of air: Dependence on pressure, temperature and composition*, applied optics, Vol. 6, pp. 51-58
- Pacione, R., E. Fionda, R. Ferrara, R. Lanotte, C. Sciarretta, and F. Vespe (2002) *Comparison of atmospheric parameters derived from GPS, VLBI and a ground-based microwave radiometer in Italy*. Physics and Chemistry of the Earth, Vol. 27, pp. 309-316
- Park, C., J. Baek, and J. Cho (2010) *Analysis on Characteristics of Radiosonde Bias Using GPS Precipitable Water Vapor*. J. Astro. Space Sci., Vol. 27, No. 3, pp.213-220
- Resch, G.M. and E.S. Claflin (1979) *Microwave radiometry as a tool to calibrate tropospheric water-vapor delay*. NASA Conference Publications, pp. 377-384
- Resch, G.M., M.C. Chavez, and N.I. Yamane (1982) *Description and overview of an instrumental designed to measure line-of-sight delay due to water vapor*. TDA Progress Report 42-72, Jet Propulsion Laboratory, Pasadena
- Resch, G.M. (1983) *Inversion algorithms for water vapor radiometers operating at 20.7 and 31.4 GHz*. TDA Progress Report 42-76, October-December
- Resch, G.M. D.E. Hogg, and P.J. Napier (1984) *Radiometric correction of atmospheric path length fluctuations in interferometric experiments*. Radio Science, 19, 1, pp. 411-422
- Rocken, C., T. Van Hove, J. Johnson, F. Solheim, R. Ware, M. Bevis, and S. Chiswell (1995) *GPS/STORM GPS sensing of atmospheric water vapor for meteorology*. J. Atmos. Oceanic Technol., Vol. 12, pp. 468-478
- Rosenkranz, P.W. (1993) *Absorption of microwaves by atmospheric gases*. Atmospheric Remote Sensing by Microwave Radiometry, Eds. by M.A. Janssen, chap. 2, John Wiley, New York, pp. 37-90
- Rosenkranz, P.W. (1998) *Water vapor microwave continuum absorption: A comparison of measurements and models*. Radio Science, Vol. 33, No. 4, pp. 919-928
- Rosenkranz, P.W. (1998) *Correction to "Water vapor microwave continuum absorption: A comparison of measurements and models"*. Radio Science, Vol. 34, No. 4, p. 1025
- Rottmann, H. and A.L. Roy (2007) *MPIfR water vapor radiometer scientific evaluation*. Max-Planck-Institute for Radioastronomy Report
- Roy, A.L., U. Teuber, and R. Keller (2004) *The water vapour radiometer at Effelsberg*. Proc. 7th European VLBI Network Symposium
- Roy, A., U. Teuber, and R. Keller (2004) *Background and status of the water-vapor radiometer at Effelsberg*. In-house progress report on the WVR project for phase correction of 3 mm VLBI (<http://www.mpifr-bonn.mpg.de/staff/aroy/wvr.html>)
- Saastamoinen, J. (1972) *Atmospheric correction for the troposphere and stratosphere in radio ranging of satellites*. The Use of Artificial Satellites for Geodesy, S. W. Henriksen et al. Eds., American Geophysical Union, pp. 247-251
- Schlueter, W., W. Schwarz, B. Buerki, A. Somieski, P. Haeefe, and J. Cho (2006) *About the Collocation of Water Vapour Radiometers, Solar Spectrometer, Radiosondes at the Fundamental Station Wettzell*. Workshop on Measurement of atmospheric water vapour: Theory, Techniques, Astronomical and Geodetic Applications, Wettzell, Germany, Oct. 9-11, 2006
- Sharkov, E.A. (2003) *Passive microwave remote sensing of the Earth*. Praxis publishing ltd., Chichester, ISBN 3-540-43946-3
- Smith, E.K. and S. Weintraub (1953) *The constants in the equation for atmospheric refractive index at radio frequency*. J. Res. Natl. Bur. Stand., Vol. 50, pp. 39-41
- Snajdrova, K., J. Böhm, P. Willis, R. Haas, and H. Schuh (2006) *Multi-technique comparison of tropospheric zenith delays derived during the CONTO2 campaign*. J. Geod., Vol. 79, doi:10.1007/s00190-005-0010-z, pp. 613-623
- Sohn, D. and J. Cho (2010) *Trend analysis of GPS precipitable water vapor above south korea over the last 10 years*. J. Astron Space Sci., doi:10.5140JASS.2010, Vol. 27, No. 3, pp. 231-238
- Stoew, B., and C. Rieck (1999) *Dual Channel Water Vapour Radiometer Development*. Proceedings of the 13<sup>th</sup> Working Meeting on European VLBI for Geodesy and Astrometry, Eds. W. Schlueter and H. Hase, pp. 261-264
- Tahmoush, D.A. and A.E.E. Rogers (2000) *Correcting atmospheric path variations in millimeter wavelength very long baseline interferometry using a scanning water vapor spectrometer*. Radio Science, Vol. 35, pp. 1241-1251
- Takahashi, F., T. Kondo, Y. Takahashi, and Y. Koyama (1997) *Very Long Baseline Interferometer*. Ohmsha Ltd., Tokyo, ISBN: 4-

274-90378-8, pp. 128-132

- Takiguchi, H., T. Kato, H. Kobayashi, and T. Nakaegawa (2000) *GPS observations in Thailand for hydrological applications*. Earth Planets Space, Vol. 52, pp. 913-919
- Teitelbaum, L.P., S.J. Keihm, R.P. Linfield, M.J. Mahoney, and G.M. Resch (1996) *A demonstration of precise calibration of tropospheric delay fluctuations with water vapor radiometer*. Geophys. Res. Letters, Vol. 23(25), pp. 3719-3722
- Thayer, G.D. (1974) *An improved equation for the radio refractive index of air*. Radio Sci., Vol. 9, pp. 803-807
- Turner, D.D., M.P. Cadetdu, U. Lohnert, S. Crewell, and A.M. Vogelmann (2009) *Modifications to the water vapor continuum in the microwave suggested by ground-based 150-GHz observation*. IEEE Transaction on Geoscience and Remote Sensing, Vol. 47, pp. 3326-3337
- Van Vleck, J.H. and V.F. Weisskopf (1945) *On the Shape of Collisionally Broadened Lines*. Reviews of Modern Physics, Vol. 17, pp. 227-236
- Van Vleck, J.H. (1947a) *The absorption of microwaves by uncondensed water vapor*. Physical Review, Vol. 71, pp. 425-433
- Van Vleck, J.H. (1947b) *The absorption of microwaves by oxygen*, Physical Review, Vol. 71, pp. 413-424
- Van Vleck, J.H. and V.F. Weisskopf (1947) *On the shape of collision broadened lines*. Reviews of modern physics, Vol. 17, pp. 227-236
- Wang, J. and L. Zhang (2008) *Systematic errors in global radiosonde precipitable water data from comparisons with ground-based GPS measurements*. J. Climate, Vol. 21, pp. 2218-2238
- Ware, H. Randolph, C. Rocken, and K.J. Hurst (1986) *A global positioning system baseline determination including bias fixing and water vapor radiometer corrections*. J. Geophys. Res., Vol. 91, pp. 9183-9192
- Ware, R., C. Rocken, F. Solheim, T. Van Hove, C. Alber, and J. Johnson (1993) *Pointed water vapor radiometer corrections for accurate global positioning system surveying*. Geophysical Research Letters, Vol. 20(23), pp. 2635-2638
- Westwater, E. R., Crewell, S. and C. Mätzler (2004) *Frontiers in Surface-based Microwave and Millimeter Wavelength Radiometry*. International Geoscience and Remote Sensing Symposium (IGARSS), Anchorage, Alaska, 20-24 September 2004
- Westwater, E.R., S. Crewell, and C. Maetzler (2005) *Surface-based microwave and millimeter wave radiometric remote sensing of the troposphere: a tutorial*. IEEE Geoscience and Remote Sensing Society Newsletter, March, 134, pp. 16-33
- Wu, S.-C. (1979) *Optimum frequencies of a passive microwave radiometer for tropospheric path-length correction*. IEEE transactions on antennas and propagation, AP-27, 2, March 1979, pp. 233-239
- Zhang, B., X.-W. Zheng, J.-L. Li, and Y. Xu (2008) *An approach of tropospheric correction for VLBI phase-referencing using GPS data*. Chin J. Astron. Astrophys, Vol. 8, No. 1, doi:10.1088/1009-9271/8/1/14

## **Acknowledgements**

I deeply appreciate the thoughtful guidance of Priv.-Doz. Dr.-Ing Axel Nothnagel. He taught me with keen questions and warm advices. His intuitional insight and sagaciousness have been always leading me to reasonable conclusions. I have also learned the attitudes from him such as keeping an open-mind and modesty to other people. It was a great honor to study with such a great teacher. I should also express my appreciations to Prof. Dr.-Ing Heiner Kuhlmann. He supported me a lot during my stay in Bonn. I would like to convey a lively sense of gratitude to Assoc. Prof. Dipl.-Ing. Dr. techn. Johannes Böhm. He pleasingly provided data and helped me to refine the thesis.

I should send my warm thanks to Dr. Alan Roy. He provided the WVR data and gave me a lot of information as the developer of the WVR. A lot of thanks to colleagues in KASI should not be missed. I have spent almost 18 years in KASI. And it was a great pleasure to be with the nice colleagues. And I also would like to thank all colleagues in IGG, University of Bonn. Among them, I would like to express special thanks to Markus Vennebusch. He is one of the most congenial friends to me. More frankly, we are rather tied with brotherhood.

I would like to share my pleasures with my family. My parents in law were always supporting me. To my father, I should appreciate that all of my achievements are originated from you. Boundless thanks should be poured over boundless sacrifices of my mother for me during my lifetime. Finally, I should express my thanks from the inmost of my heart to my wife and daughter. They are the source of my strength to cope with a lot of difficulties.